

University of Kentucky

UKnowledge

Theses and Dissertations--Biomedical
Engineering

Biomedical Engineering


2023

MULTISCALE AND MULTIMODALITY OPTICAL IMAGING OF BRAIN HEMODYNAMICS AND FUNCTION

Mehrana Mohtasebi

University of Kentucky, mehrana.mohtasebi@gmail.com

Author ORCID Identifier:

 <https://orcid.org/0000-0002-4689-990X>

Digital Object Identifier: <https://doi.org/10.13023/etd.2023.411>

[Right click to open a feedback form in a new tab to let us know how this document benefits you.](#)

Recommended Citation

Mohtasebi, Mehrana, "MULTISCALE AND MULTIMODALITY OPTICAL IMAGING OF BRAIN
HEMODYNAMICS AND FUNCTION" (2023). *Theses and Dissertations--Biomedical Engineering*. 80.
https://uknowledge.uky.edu/cbme_etds/80

This Doctoral Dissertation is brought to you for free and open access by the Biomedical Engineering at UKnowledge. It has been accepted for inclusion in Theses and Dissertations--Biomedical Engineering by an authorized administrator of UKnowledge. For more information, please contact UKnowledge@lsv.uky.edu.

STUDENT AGREEMENT:

I represent that my thesis or dissertation and abstract are my original work. Proper attribution has been given to all outside sources. I understand that I am solely responsible for obtaining any needed copyright permissions. I have obtained needed written permission statement(s) from the owner(s) of each third-party copyrighted matter to be included in my work, allowing electronic distribution (if such use is not permitted by the fair use doctrine) which will be submitted to UKnowledge as Additional File.

I hereby grant to The University of Kentucky and its agents the irrevocable, non-exclusive, and royalty-free license to archive and make accessible my work in whole or in part in all forms of media, now or hereafter known. I agree that the document mentioned above may be made available immediately for worldwide access unless an embargo applies.

I retain all other ownership rights to the copyright of my work. I also retain the right to use in future works (such as articles or books) all or part of my work. I understand that I am free to register the copyright to my work.

REVIEW, APPROVAL AND ACCEPTANCE

The document mentioned above has been reviewed and accepted by the student's advisor, on behalf of the advisory committee, and by the Director of Graduate Studies (DGS), on behalf of the program; we verify that this is the final, approved version of the student's thesis including all changes required by the advisory committee. The undersigned agree to abide by the statements above.

Mehrana Mohtasebi, Student

Dr. Guoqiang Yu, Major Professor

Dr. Sridhar Sunderam, Director of Graduate Studies

MULTISCALE AND MULTIMODALITY OPTICAL IMAGING OF BRAIN
HEMODYNAMICS AND FUNCTION

DISSERTATION

A dissertation submitted in partial fulfillment of the
requirements for the degree of Doctor of Philosophy in the
College of Engineering
at the University of Kentucky

By
Mehrana Mohtasebi
Lexington, Kentucky
Director: Dr. Guoqiang Yu, Professor of Biomedical Engineering
Lexington, Kentucky
2023

Copyright © Mehrana Mohtasebi 2023
<https://orcid.org/0000-0002-4689-990X>

ABSTRACT OF DISSERTATION

MULTISCALE AND MULTIMODALITY OPTICAL IMAGING OF BRAIN HEMODYNAMICS AND FUNCTION

Frequent measurement of cerebral hemodynamics is crucial for continuous assessment of brain function and health. Low-frequency oscillations (LFOs; < 0.1 Hz) have shown promise as an indicator of altered neurologic activity in the abnormal brain. Moreover, quantification of temporal correlations in LFOs across distinct brain regions enables mapping of regional neurovascular disorders. Portable diffuse optical techniques such as near-infrared spectroscopy (NIRS) and diffuse correlation spectroscopy (DCS) enable noninvasive and continuous measurements of cerebral oxygenation and cerebral blood flow (CBF), respectively. However, most NIRS/DCS systems use limited numbers of discrete light sources and detectors and thus lack combinations of high temporal/spatial resolution and large field-of-view (FOV) for brain imaging. Recent development of an innovative noncontact speckle contrast diffuse correlation tomography (scDCT) in our lab provides a low-cost and portable tool for high-density imaging of CBF distributions over large FOVs. The scDCT uses a galvo-mirror to remotely deliver coherent point near-infrared light to multiple source positions and a CMOS camera as a high-density 2-D detector array to quantify spatial fluctuations of diffuse laser speckles, resulting from movement of red blood cells. Boundary CBF data were input to a unique finite-element-method (FEM)-based reconstruction algorithm for 3-D imaging of CBF distributions. However, scDCT was hindered for extracting LFOs due to its low sampling rate. In this study, scDCT was optimized to achieve high sampling rates and fast image reconstructions by use of moving window algorithms with parallel computations (Project 1). Power spectral density (PSD) analysis was performed to investigate altered LFOs during transient cerebral ischemia in neonatal piglets. Transient cerebral ischemia caused reductions in both CBF and PSD, supporting inclusion of scDCT in the growing field of LFO analysis. One remaining limitation was the long computational time required for 3-D reconstruction, which prohibited real-time applications. To overcome this limitation, a depth-sensitive diffuse speckle contrast topography (DSCT) method was developed for analyzing scDCT data to achieve fast and high-density 2-D mapping of CBF distribution without the need of complex and time-consuming 3-D reconstructions (Project 2). New head-simulating phantoms with known optical/geometric properties were designed and fabricated to evaluate the spatial resolution and depth sensitivity of DSCT method. In-vivo experiments

verified the capability of DSCT in tracking dynamic changes in CBF at different depths during CO₂ inhalation and transient cerebral ischemia in rats. In addition to preclinical studies, a low-cost, wearable, fluorescence eye loupe (*FLoupe*) device was invented for intraoperative visualization of brain tumor margin in the clinic (Project 3). Consistent results were observed against an expensive, large, standard fluorescence operative microscope for the guidance of tumor resection. Overall, through 3 projects this dissertation demonstrated a variety of noninvasive noncontact optical technologies (scDCT, DSCT, and *FLoupe*) that enabled multiscale (rodents, piglets, and humans) and multimodality (CBF and fluorescence) imaging of brain hemodynamics and function. With further optimization and validation in large populations, these cost-effective portable optical imaging devices are appealing for continuous assessment of brain health at the bedside of clinic.

KEYWORDS: Neuroimaging, Cerebral Blood Flow, Speckle Contrast Diffuse Correlation Tomography/Topography, Low-frequency Oscillations, Parallel Computation, Fluorescence Guided Surgery

Mehrana Mohtasebi

10/03/2023

Date

MULTISCALE AND MULTIMODALITY OPTICAL IMAGING OF BRAIN
HEMODYNAMICS AND FUNCTION

By
Mehrana Mohtasebi

Dr. Guoqiang Yu

Director of Dissertation

Dr. Sridhar Sunderam

Director of Graduate Studies

10/03/2023

Date

DEDICATION

I dedicate this dissertation to the unwavering support and love of my husband, Amirhossein. Your belief in my abilities, your patience during late nights and weekends consumed by research, and your constant reassurance have been invaluable. I am eternally grateful for your understanding and sacrifices. This dissertation would not have been possible without your love. With all my heart, I dedicate this work to you, Amirhossein.

ACKNOWLEDGMENTS

First and foremost, I would like to express my gratitude to my primary advisor, Dr. Guoqiang Yu, for his constant guidance and invaluable mentorship throughout my doctoral education. Dr. Yu provides exceptional assistance on training me as an independent researcher and now I feel confident to find new problems and step forward to solve them on my own. The support, guidance, feedback, and motivation provided by Dr. Yu were crucial factors that enabled the successful completion of this work. I am also thankful for the research assistant scholarship he provided me during my Ph.D. study.

My research was not possible without the support of our excellent preclinical and clinical collaborators. I extend my gratitude to Dr. Lei Chen for his tremendous assistance, guidance, and insightful discussions. His dedicated efforts in leading the animal studies to validate our scDCT device for imaging cerebral hemodynamics in rodents and piglets are highly appreciated. Additionally, I would like to express my thanks to Dr. Thomas A. Pittman for his time, effort and invaluable feedback in testing and developing *FLoupe* device for identification of human brain tumors intraoperatively. Also, it has been an honor to collaborate with experts from various departments including Dr. Li Chen, Dr. Kathryn Saatman, Dr. David Powell, Dr. Jeffrey R. Smiley, and Dr. Piotr Rychahou.

I would like to express my gratitude to my former colleagues, Dr. Chong Huang, Dr. Siavash Mazdeyasna, Dr. Ahmed Bahrani, Dr. Daniel Irwin, and Dr. Dara Singh, who have always been welcoming to my questions and discussions.

Likewise, I would like to express my gratitude to the following colleagues and good friends in the Biomedical Optics Laboratory who have been part of this journey and experience, including Xuhui, Faraneh, Samaneh, Pegah, Fatemeh, Faezeh, and

Chowdhury. Their generous support, stimulating discussions, shared moments of laughter, collaborative journeys, collective celebrations, and even mutual challenges have all played indispensable roles throughout my Ph.D. journey.

I extend my thanks to the esteemed members of my doctoral advisory committee, Dr. Guoqiang Yu, Dr. Abhijit Patwardhan, Dr. Sridhar Sunderam, Dr. Qiang Cheng, and Dr. Lei Chen for their invaluable guidance and insights into my research. Additionally, I am grateful to Dr. Kathryn Saatman for graciously serving as an external examiner for my doctoral dissertation.

I would like to express my sincere gratitude to the Pigman College of Engineering at the University of Kentucky for giving me the invaluable opportunity to participate in the Biomedical Engineering Ph.D. program.

I also acknowledge financial support from the American Heart Association (AHA) Predoctoral Fellowship (no.: 835726) (2021 - 2023), National Institutes of Health (NIH) (Grant no.: R01 EB028792 (2020 - 2023), R01 HD101508 (2020 - 2025), R21 HD091118 (2018 - 2021), R56 NS117587 (2020 - 2021), R01 AG062480 (2019 - 2024), R21 NS114771 (2020 - 2022), and Neuroscience Research Priority Area (NRPA) Pilot Grant (2021 - 2022) from the University of Kentucky. The content of this dissertation is solely the responsibility of myself and my collaborators in each study and does not necessarily represent the official views of the AHA, NIH or University of Kentucky.

My heartfelt appreciation goes to my beloved father, my amazing mother, and my awesome brother for their unconditional love and encouragement. A special thank you goes to my husband for always listening and his never-ending support.

TABLE OF CONTENTS

ACKNOWLEDGMENTS	iii
LIST OF TABLES	viii
LIST OF FIGURES	ix
CHAPTER 1. Introduction.....	1
1.1 <i>Development of scDCT/DSCT for Imaging Cerebral Blood Flow and Detecting Low Frequency Oscillations</i>	1
1.1.1 Study Background and Significance.....	1
1.1.2 Limitations of Current Neuroimaging Technologies	3
1.1.3 Our Solutions	10
1.2 <i>Development of FLoupe for Intraoperative Identification of Human Brain Tumors</i>	12
1.2.1 Study Background and Significance.....	12
1.2.2 Limitations of Current Brain Tumor Imaging Technologies	12
1.2.3 Our Solutions	14
1.3 <i>Dissertation Organization</i>	15
CHAPTER 2. Detection of Low Frequency Oscillations in Neonatal Piglets with Speckle Contrast Diffuse Correlation Tomography (scDCT)	16
2.1 <i>Introduction</i>	17
2.2 <i>Materials and Methods</i>	22
2.2.1 Animal Preparations and Experimental	22
2.2.2 scDCT System for Data Acquisition.....	24
2.2.3 Boundary Data Processing for CBF.....	26
2.2.4 3-D Image Reconstruction of CBF	29
2.2.5 Power Spectral Density (PSD) Analysis for LFO Intensity	31
2.3 <i>Results</i>	32
2.3.1 rCBF and Vital Variations During Transient Global Ischemia	32
2.3.2 LFOs During Transient Global Ischemia.....	35
2.3.3 PSD Changes in LFOs for Identification of Neurological Variations	37
2.4 <i>Discussion and Conclusions</i>	38
CHAPTER 3. Depth-Sensitive Diffuse Speckle Contrast Topography (DSCT) for High-Density Mapping of Cerebral Blood Flow in Rodent.....	45
3.1 <i>Introduction</i>	46

3.2	<i>Materials and Methods</i>	50
3.2.1	Hybrid DSCT and LSCI System.....	50
3.2.2	LSCI Method for 2-D Mapping of Superficial CBF.....	52
3.2.3	DSCT Method for 2-D Mapping of CBF at Different Depths.....	54
3.2.4	Depth Sensitivity Tests Using New Head-simulating Layered Phantoms....	58
3.2.5	In-vivo Experiments in Rats	60
3.2.6	Statistical analysis.....	62
3.3	<i>Results</i>	63
3.3.1	DSCT Performance Depends on Sampling Density	63
3.3.2	DSCT Enables 2-D Mapping of Phantom Flow Contrasts with Depth Sensitivity	64
3.3.3	DSCT Enables 2-D Mapping of rCBF at Different Depths in Rats.....	65
3.3.4	DSCT Captures Dynamic rCBF Responses During CO ₂ Inhalations in Rats 66	66
3.3.5	DSCT Captures Dynamic rCBF Responses to Transient Arterial Ischemia and Ischemia and Hypoxia in Rats.....	69
3.4	<i>Discussion and Conclusions</i>	73
CHAPTER 4. A Wearable Fluorescence Imaging Device for Intraoperative Identification of Human Brain Tumors		77
4.1	<i>Introduction</i>	78
4.2	<i>Materials and Methods</i>	81
4.2.1	<i>FLoupe-1</i> for Imaging of Fluorescein Contrast	82
4.2.2	<i>FLoupe-2</i> for Imaging of 5-ALA Contrasts.....	85
4.3	<i>Results</i>	87
4.4	<i>Discussion and Conclusions</i>	90
CHAPTER 5. Study Summary, Innovation, Limitations, And Future Perspective		94
5.1	<i>Development of scDCT/DSCT for Imaging Cerebral Blood Flow and Detecting Low Frequency Oscillations</i>	94
5.1.1	Study Summary and Innovation.....	94
5.1.2	My Contribution to the Study	95
5.1.3	Study Limitation and Future Perspective.....	98
5.2	<i>Development of FLoupe for Intraoperative Identification of Human Brain Tumors</i>	99
5.2.1	Study Summary and Innovation.....	99
5.2.2	My Contribution to the Study	100
5.2.3	Study Limitation and Future Perspective.....	101
5.3	<i>My Contribution to Other Studies</i>	102

APPENDIX. Glossary.....	103
REFERENCES	107
VITA.....	117

LIST OF TABLES

Table 1.1: Comparison of functional neuroimaging techniques	9
Table 3.1: Impact of sampling density on DSCT performance	63
Table 3.2: Average rCBF variations (mean \pm standard error) from their baselines during CO ₂ inhalation over 6 rats (moving window method)	67
Table 3.3: Pairwise multiple comparisons to assess differences in rCBF variations between different phases of CO ₂ inhalation	67
Table 3.4: Average rCBF variations (mean \pm standard error) from their baselines during unilateral and bilateral CCA ligations over 5 rats	69
Table 3.5: Pairwise multiple comparisons to assess differences in rCBF variations between different phases of ligation in right hemisphere and left hemisphere	70
Table 4.1: Patient demographics and tumor characteristics	83

LIST OF FIGURES

Figure 1.1: Operating principle of fNIRS.....	6
Figure 2.1: Experimental setup for continuous CBF monitoring of neonatal piglets during transient global ischemia.....	25
Figure 2.2: scDCT image processing for determining source locations and reconstruction steps for generating 3-D CBF images.....	28
Figure 2.3: Measurement results from Piglet #1 and Piglet #2 during transient global ischemia.....	34
Figure 2.4: Power spectra of rCBF signals during baseline measurements.....	36
Figure 2.5: Detrended and band-pass filtered time course changes in rCBF over each interval for both piglets.....	37
Figure 2.6: PSD analysis of LFOs in both piglets.....	39
Figure 3.1: A hybrid DSCT and LSCI system for 2-D mapping of CBF in rats.....	52
Figure 3.2: A flowchart for data processing in LSCI and DSCT methods.....	57
Figure 3.3: New head-simulating layered phantoms with known optical/geometry properties.....	60
Figure 3.4: Effect of sampling density on spatial resolution of DSCT.....	64
Figure 3.5: DSCT and LSCI measurement results for UK logo phantoms.....	65
Figure 3.6: 2-D mapping of rCBF distributions with LSCI and DSCT.....	66
Figure 3.7: DSCT measurements of rCBF responses to CO ₂ inhalation in rats.....	68
Figure 3.8: DSCT measurements of rCBF responses to sequential unilateral and bilateral CCA ligations in rats.....	71
Figure 3.9: DSCT measurements of rCBF variations during asphyxia in rats.....	72
Figure 4.1: Development of <i>Floupe-1</i> prototype.....	84
Figure 4.2: Development of <i>Floupe-2</i> prototype.....	85
Figure 4.3: Use of <i>Floupe-2</i> for fluorescence imaging of MGs.....	87
Figure 4.4: Comparison of imaging results in a fluorescence phantom and a patient with MG.....	89
Figure 4.5: Comparison of imaging results from three patients with MGs (P1-P3).....	91

CHAPTER 1. INTRODUCTION

1.1 Development of scDCT/DSCT for Imaging Cerebral Blood Flow and Detecting Low Frequency Oscillations

1.1.1 Study Background and Significance

The human brain is one of the most intricate and metabolically demanding organs in the body. It consumes approximately 20% of the body's oxygen supply [1]. The brain's proper function relies significantly on maintaining adequate cerebral blood flow (CBF), to ensure the delivery of oxygen and glucose to the brain tissue while efficiently removing metabolic waste products [2]. Elevated CBF, known as cerebral hyper-perfusion, can lead to increased intracranial pressure, potentially damaging the fragile brain tissue. Conversely, reduced CBF, referred to as cerebral hypo-perfusion, can directly result in the death of brain cells. Regularly assessing CBF plays a pivotal role in evaluating brain function and overall health, as well as monitoring therapeutic interventions for various cerebral vascular and cellular conditions, such as stroke, head trauma, and shock [3].

The rhythmic oscillations observed in CBF result from various factors, including the cardiac cycle, respiratory motion, myogenic, neurogenic, and metabolic mechanisms [4]. For instance, in humans, oscillations at approximately 1 Hz are linked to the heartbeat, while those at around 0.3 Hz correspond to respiration. Frequencies below 0.1 Hz are generally referred to as low-frequency oscillations (LFOs), which are also known as Mayer waves [4-6].

CBF abnormalities impact rhythmic oscillations, including LFOs. In healthy brains, LFOs typically maintain stability, whereas alterations in localized LFOs are indicative of

compromised brain tissue [7]. Consequently, there is a critical need for continuous monitoring of LFOs to enhance our comprehension of the pathological mechanisms underlying these conditions and to facilitate the development of medical interventions [8].

Heartbeat and respiratory rates scale with the size of the species [9]. However, LFOs have not been shown to be dependent on size. Studies have demonstrated the presence of LFOs in various animals: piglets [10], monkeys [11], cats [12, 13], rabbits [14], and rodents [9, 15, 16]. Most LFOs in these animals exist below 0.1 Hz. Interestingly, these frequencies are the same as those found in humans [4-6, 16]. This feature makes LFOs an attractive target for producing translatable neurological findings.

Taken together, there is an unmet need for continuous neuroimaging tools that offer sufficiently high temporal and spatial resolutions to monitor fast CBF changes, spatially distributed brain function, and accurately detect LFOs [17, 18]. However, currently available neuroimaging technologies, such as functional magnetic resonance imaging (fMRI), positron emission tomography (PET), and magnetoencephalography (MEG) are bulky, expensive and cannot be used in the surgical room or at the bedside for continuous and longitudinal monitoring [19]. Portable techniques such as electroencephalography (EEG) and currently available optical neuroimaging methods like functional near-infrared spectroscopy (fNIRS), diffuse correlation spectroscopy (DCS), and high-density diffuse optical tomography (HD-DOT) lack the combination of high temporal-spatial resolution and a large region of interest (ROI) (see **Chapter 1.1.2**). To overcome these limitations, we have optimized and validated an innovative, noncontact, low-cost, and portable speckle contrast diffuse correlation tomography (scDCT; US Patent #9/861,319, 2018 [20]) for high-density 3-D imaging of blood flow and detection of LFOs within CBF variations (see

Chapter 1.1.3). We also investigated an alternative, depth-sensitive diffuse speckle contrast topography (DSCT) method for analyzing scDCT data to achieve fast and high-density 2-D mapping of CBF distributions at different depths without the need of complex and time-consuming 3-D reconstruction (see **Chapter 1.1.3**).

1.1.2 Limitations of Current Neuroimaging Technologies

Numerous imaging techniques have been developed and applied to evaluate brain hemodynamics. Major neuroimaging modalities are fMRI [21], PET [22, 23], MEG [24], EEG [25], fNIRS [26], DCS [27] and HD-DOT [7, 28, 29]. These functional neuroimaging techniques vary in terms of detection methods, brain coverage, spatial and temporal resolutions, portability, and cost. Below is a brief overview of these functional neuroimaging modalities.

fMRI is a non-invasive imaging modality that measures brain activity [19, 21, 30]. It relies on the magnetic properties of de-oxygenated hemoglobin in the blood to serve as a natural intravascular contrast agent. This method, known as Blood Oxygenation Level Dependent (BOLD) imaging, relies on changes in blood oxygenation resulting from neuronal activity. BOLD-fMRI studies have revealed abnormal LFO amplitudes in patients with schizophrenia [31], mild cognitive impairment [32], Alzheimer's disease [33], major depressive disorder [34], sleep-deprived brain [35], traumatic brain injury (TBI) [36], and stroke [37]. Despite these successes, BOLD-fMRI has limited temporal resolution, typically around 2 to 5 seconds [19]. fMRI offers the best spatial resolution among available functional neuroimaging techniques (2 — 3 mm). Exposure to strong magnetic fields during fMRI is generally considered safe. Motion during scanning can degrade image quality, so precautions are taken to minimize it. Participants with certain ferromagnetic

objects in their bodies, like pacemakers, are excluded from fMRI. The procedure also involves loud acoustic noise, necessitating the use of earplugs for noise reduction [19].

PET is a medical imaging technique that measures regional CBF or regional cerebral metabolic rate of glucose (rCMRG) using radioactively labeled tracer molecules [19, 22, 23]. These tracers are typically administered intravenously or inhaled by the patient. However, PET requires a particle accelerator (cyclotron) to produce these radioisotopes, which contributes to its higher acquisition cost. Additionally, the production of expensive tracers contributes to the comparatively high operating cost of PET imaging [19, 38, 39]. While PET imaging offers valuable quantitative physiological data for the brain, its primary limitation is the use of ionizing radiation from conventional positron-emitting radionuclides, which restricts its use in infants.

MEG is a non-invasive electrophysiological imaging technique used to measure the extremely weak magnetic fields naturally produced by electrical currents in the brain. This makes MEG a direct method for assessing brain activity [40]. MEG provides high temporal resolution imaging of cortical brain activity, allowing the measurement of events with time scales on the order of milliseconds. The primary limitation of MEG is its extremely weak signal, which is several orders of magnitude smaller than background signals. Therefore, special shielding is necessary to eliminate interference in a typical clinical environment [24, 40].

Neuroimaging technologies like fMRI, PET and MEG are characterized by their large size, high cost, and cannot be used in the operating room or at the bedside for continuous and long-term monitoring. On the other hand, EEG and optical imaging techniques like fNIRS, DCS and HD-DOT offer noninvasive, fast, inexpensive, and

portable means for cerebral hemodynamic and LFO assessments. EEG is a neuroimaging technique that directly captures the electrical activity generated by the human brain [25]. Tiny electrical signals serve as the means of communication between neuronal cells in the brain. EEG measures the cumulative activity of these electrical signals detected at the scalp [40]. EEG has a high temporal resolution (<1 ms) but suffers from low spatial resolution due to the limited number of electrodes on the scalp that serve as a detector (2 — 3 cm). EEG is also prone to significant artifacts, including eye blinks, power line noise at 50 or 60 Hz, and muscular activity [40].

fNIRS takes advantage of the absorption properties of living tissue in the NIR range to measure alternations in concentrations of [Hb] and [HbO₂] [26]. Light in the near-infrared (NIR) spectral range (650–950 nm, called the physiological window) can penetrate deep into tissue (a few centimeters) [40, 41]. This is because light within the physiological window minimally absorbs by chromophores such as water, oxy- and deoxy-hemoglobin (Hb and HbO₂), and lipids (Figure 1.1a) [41]. fNIRS is performed by emitting NIR light into the scalp and detecting the transmitted light at detectors placed at a certain distance from the source. As the source-detector (S-D) distance increases, waves originating from the source travel deeper into the tissue before they reach the detector. The photon paths are distributed within a banana-shaped region that extends from the source to the detector, with the central region penetrating the deepest into the tissue, roughly half of the S-D distance [42, 43]. Figure 1.1b [40], shows the banana-shaped photon distribution and schematic diagram of the fNIRS technique.

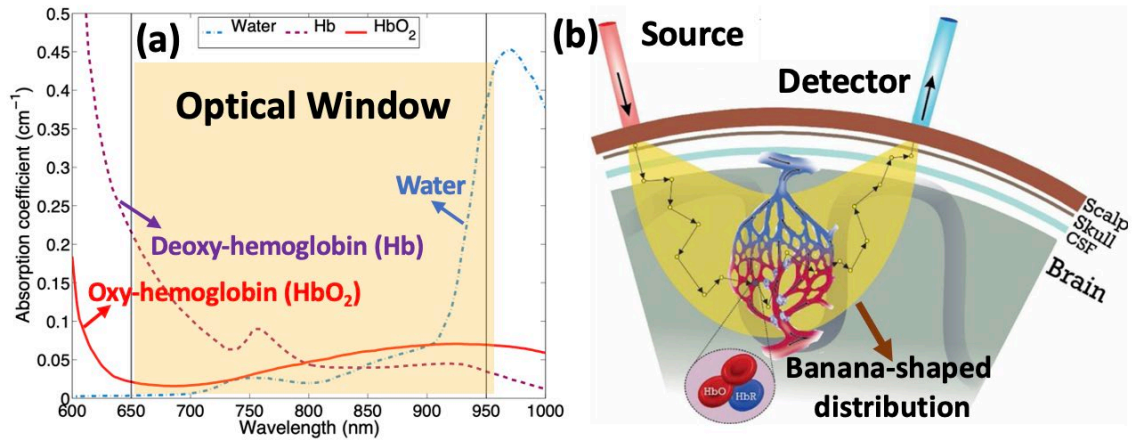


Figure 1.1: Operating principle of fNIRS.

(a) Absorption spectra of the main tissue chromophores are plotted over a large wavelength range. The inset shows the physiological window in the NIR, where water and hemoglobin absorption are relatively low. Within this part of the spectrum, light can penetrate several centimeters into the tissue. (b) In fNIRS system, NIR light is generated and guided to the head through optical fibers. A light detector captures the attenuated light that results from interactions with chromophores (i.e., Hb and HbO₂).

DCS illuminates long coherence length laser in NIR spectral range to measure tissue blood flow [44, 45]. The penetrated NIR light is also scattered, besides absorption in the tissue, and photons undergo diffusive motion as they are reflected back to the surface of the tissue [42]. By quantifying fluctuations in the intensity of diffusely scattered coherent light, information about dynamic properties of the tissue, like the motion of red blood cells in the brain (i.e., CBF), can be obtained [42]. In DCS technique, expensive photon-counting detectors are employed to capture the intensity fluctuations of individual speckles [45]. DCS has also been used to assess LFO amplitudes as a biomarker of neurologic injury during the acute period after cardiac arrest in a piglet model of pediatric cardiac arrest [10]. Hybrid fNIRS/DCS instruments have been developed to simultaneously detect LFOs of CBF, HbO₂, and Hb concentration in cognitively healthy older subjects with high- or low-risk for cerebrovascular disease [46, 47]. fNIRS and DCS are portable,

bedside, and wearable techniques for continuous and long-term recording of brain hemodynamics. These techniques are suitable for individuals of all ages, from premature neonates to adults [40].

While diffuse optical technologies such as fNIRS and DCS hold promise for detecting brain hemodynamics (CBF, HbO₂, Hb concentrations) and their corresponding LFOs, they still face several limitations. fNIRS and DCS systems equipped with limited number of discrete light sources and detectors, resulting in sparse measurements of source-detector pairs across a region of interest (ROI). This limitation causes low spatial resolution (~10–30 mm) and hinders the ability to localize activations from regionally distributed brain functions [48, 49]. Cerebral hemodynamic signals collected using fNIRS and DCS techniques are also inherently influenced by partial volume effects from overlying tissues (scalp and skull) [46, 47], causing the difficulty to discriminate the brain signal of interest.

HD-DOT systems have recently received much attention with regards to improved spatial resolution and brain signal differentiation [7, 29, 50]. Nonetheless, extending the field-of-view (FOV) with fiber-based HD-DOT contact measurement systems to gain a more complete view of the brain is hampered by complications with optical fiber coupling to heads and cap design, especially for the heads of small and fragile newborn infants [7, 29, 50].

Use of a charge-coupled-device (CCD) or complementary metal-oxide-semiconductor (CMOS) camera with thousands of pixels as a 2-D detector array provides high-density and fast parallel sampling [51]. For instance, the laser speckle contrast imaging (LSCI) technique utilizes wide-field coherent illumination in the NIR spectral range, in contrast to the long coherence length lasers used in fNIRS, DCS, and HD-DOT.

LSCI employs a CMOS/CCD camera with thousands of pixels, serving as parallel 2-D detectors for detecting spatial or temporal fluctuations in laser speckle contrast. The use of a camera, as opposed to the limited number of detectors used in NIRS, DCS, and HD-DOT, significantly increases sampling density and enables rapid, noncontact, wide FOV and high-resolution 2-D mapping of CBF distributions. Nevertheless, LSCI suffers from limited penetration depth as it can only map CBF in the superficial cortexes of rodents at a depth of less than 1 mm [52-54].

Recently developed scDCT technology in our laboratory (US Patent #9/861,319, 2018 [20]) provides a fully noncontact, low-cost, and portable tool for high-density 3-D imaging of blood flow distributions in deep tissue volumes (up to ~10 mm) [55-58]. In contrast to LSCI systems that employ widefield illumination, scDCT uses an electronic-controlled galvo-mirror to rapidly (switching time < 1 ms) deliver point NIR light (for deep tissue penetration) to many source positions on a selected ROI. Similar to LSCI, scDCT also utilizes a CMOS/CCD camera with thousands of pixels as parallel 2-D detectors for measuring spatial fluctuations in laser speckle contrast. Boundary data obtained from the selected S-D separations are fed to a unique finite-element-method (FEM)-based reconstruction algorithm to enable 3-D imaging of CBF distributions [55, 57, 59, 60]. Unlike HD-DOT, noncontact scDCT with flexible source-detector arrangement alleviates the need for complicated head helmet design, thus can be easily used on subjects with different head sizes including small animals and preterm infants. scDCT has been successfully used for continuous and longitudinal imaging of CBF distributions in *in-vivo* animal experiments such as rodents undergoing CO₂ inhalation and unilateral/bilateral ligations of common cerebral artery (CCA); neonatal piglets with CCA ligations and

intraventricular hemorrhage (IVH); and sleeping preterm infants without scalp preparation through transparent incubator wall [55, 59-63]. While these applications illustrate scDCT capability in identifying CBF responses across many subject sizes, the cited studies did not incorporate detection of LFOs due to an insufficient temporal sampling rate. To address this weakness, we utilized a moving window 3-D reconstruction method with parallel computations to facilitate LFO detections (see **Chapter 1.1.3**).

Table 1.1: Comparison of functional neuroimaging techniques

Feature	fMRI	PET	MEG	EEG	fNIR	DCS	HD-DOT	scDCT/DSCT
Spatial resolution	2 to 3 mm	4 mm	< 1 cm	2 to 3 cm	~10 to 30 mm	20 to 30 mm	5 to 10 mm	Tens of micrometers (head surface) to 2 millimeters (deep brain)
Temporal resolution	~2 to 5 s	~30 to 40 s	< 1 ms	<1 ms	20 s	1 s	0.1 to 1 s	0.2 to 5 s
Non-Invasive	Yes	No ^a	Yes	Yes	Yes	Yes	Yes	Yes
Expensive	Yes	Yes	Yes	No	No	No	No	No
Portable	No	No	No	Yes	Yes	Yes	Yes	Yes
Long term recording	No	No	No	Yes	Yes	Yes	Yes	Yes
Contact measurement	No	No	Yes	Yes	Yes	Yes	Yes	No
Loudness	Noisy	Silent	Silent	Silent	Silent	Silent	Silent	Silent

^aIt can be considered as a minimally invasive procedure (need of extrinsic contrast injection).

In scDCT, the computational time required for 3-D reconstruction in high-density sampling with large numbers of sources and detectors is very long, which prohibited real-time applications. The FEM-based 3-D reconstruction algorithm comprises two key steps: solving a forward problem for computing light propagation within the tissue and solving an inverse problem for adjusting tissue optical properties [64, 65]. Creating a single CBF

mapping through the FEM-based 3-D reconstruction algorithm is complex and time-consuming, taking from several minutes to hours. Increasing the number of sources and detectors improves spatial resolution but comes at the expense of low temporal resolution and high computational overhead/time for 3-D reconstruction, thereby prohibiting real-time applications [65].

To reduce the computation time, we presented a new DSCT method with parallel computation for analyzing scDCT data to achieve fast and high-density 2-D mapping of flow distributions at different depths without the need for complex and time-consuming 3-D reconstruction (see **Chapter 1.1.3**). Table 1.1 compares different characteristics of the neuroimaging modalities discussed in this section.

1.1.3 Our Solutions

This dissertation presented a modified scDCT system for detection of LFOs within CBF variations in neonatal piglets. Neonatal piglets were selected as model subjects due to their mid-range head size, high anatomical similarity and translational potential to human neonates. scDCT was optimized to achieve high sampling rates and fast image reconstructions. The numbers of scanning sources and detectors in the scDCT were optimized to balance the temporal and spatial resolutions of CBF imaging for examining regional brain responses and deriving LFOs after signal filtering. We adapted a moving window 3-D reconstruction method to achieve a fast sampling rate of 5 Hz, which is much higher than the sampling rate using conventional reconstruction methods (e.g., 0.2 Hz) [18, 55]. With a sampling rate of 5 Hz, which is higher than the typical cardiac and respiratory rates in neonatal piglets (which are less than 2.5 Hz), it becomes possible to eliminate the influences of cardiac and respiratory oscillations on CBF signals through low-pass filtering

[58, 61]. A new 3-D reconstruction algorithm using parallelization functionalities in MATLAB (MathWorks) was developed to achieve a sizable increase in reconstruction speed while maintaining reconstruction quality. With these notable improvements, LFOs in piglet brains were successfully isolated and quantified by the optimized scDCT technique [58].

This dissertation also presented depth-sensitive diffuse speckle contrast topography (DSCT) method for analyzing scDCT data in adult rats. DSCT enables fast and high-density 2-D mapping of CBF distributions at different depths without the need for complex and time-consuming 3-D reconstruction. The DSCT acquires boundary data using the same hardware as the scDCT. Unlike the 3-D reconstruction algorithm that required solving both forward and inverse problems, DSCT only calculates blood flow indices (BFIs) for various S-D pairs with different distances. Therefore, DSCT approach is simpler, faster, and less sensitive to boundary measurement noises than the scDCT with 3-D reconstruction. Through the selection of S-D pairs with different separations based on the desired imaging depth, DSCT distinguishes between short and long photon paths within the measured tissue volume to create depth-sensitive 2-D maps BFIs. Additionally, we have developed a rapid computation method that leverages the functions of the Image Processing Toolbox™ and Parallel Computing Toolbox™ in MATLAB (MathWorks) to quickly calculate high-density blood flow maps.

1.2 Development of *FLoupe* for Intraoperative Identification of Human Brain Tumors

1.2.1 Study Background and Significance

There are nearly 700,000 people in the U.S. living with a brain tumor [66]. Among primary brain tumors, malignant gliomas (MGs) make up to 35-45% and have an incidence of approximately 5 per 100,000 people [67, 68]. MGs are known for their aggressiveness, high invasiveness, and the damage they cause to neurological functions [69]. Surgical resection remains the primary treatment approach for MGs, and the degree of resection is closely linked to patient survival [70-76]. However, conventional surgeries achieve gross-total resection (GTR) rates of only 30-55% due to challenges in identifying diffuse infiltrative tumor cells at the resection margin and tissue shifts during surgery [77-81].

1.2.2 Limitations of Current Brain Tumor Imaging Technologies

Conventional tumor resection methods heavily depend on a surgeon's ability to detect subtle changes caused by invasive tumors within the tissue. In more recent approaches, neurosurgeons have turned to preoperative imaging techniques like MRI, computed tomography (CT), and angiography to identify tumors [82]. Some MRI machines, specifically designed for intraoperative imaging, assist neurosurgeons in safely navigating the intricate structures surrounding the tumor [83]. Nevertheless, the integration of MRI techniques comes with high costs, time consumption, and notable disruptions to the surgical process. Additionally, certain tumor types, like high-grade MGs, present challenges due to their poorly defined tissue boundaries and tendrils extending from the primary tissue volume, making precise localization during resection a daunting task. The

presence of residual cancer cells at the surgical margin often necessitates repeat surgeries, imposing a substantial burden on both patients and healthcare systems [70-76].

Fluorescence imaging has emerged as an advanced adjunctive technique, enabling real-time, cancer-specific detection without the need to worry about brain tissue shifts and with minimal interference with the surgical process [74-81, 84]. Surgeries guided by fluorescence imaging achieve GTR rates of 75-100%, a substantial improvement compared to conventional surgeries with GTR rates of 30-55% [77, 78, 85, 86]. The optimization of imaging technologies to enhance fluorescence contrasts has been a subject of research and development over several decades [77].

Currently, the established standards for intraoperative visualization of MGs involve the use of neurosurgical operative microscopes. Industries have developed supplementary fluorescence modules, approved by the FDA, that can be affixed to standard neurosurgical operative microscopes to facilitate fluorescence imaging during surgery [77, 80, 81, 84, 85]. For example, Carl Zeiss Meditec (Oberkochen, Germany) offers the PENTERO® 900 microscope with a YELLOW 560™ filter kit for Fluorescein visualization and a BLUE 400™ filter kit for 5-aminolevulinic acid (5-ALA) visualization. The PENTERO® 900, equipped with filter kits, includes Xenon arc lamps emitting white light, complemented by special excitation filters operating within specific wavelength ranges. These ranges encompass 460-500 nm (YELLOW 560™) for exciting Fluorescein and 400-410 nm (BLUE 400™) for 5-ALA contrasts. On the other hand, the integration of emission filters into the detection paths customizes emissions within the wavelength ranges of 540-690 nm (YELLOW 560™) and 620-710 nm (BLUE 400™) for both ocular visualization and the display of Fluorescein and 5-ALA fluorescence images on a monitor, respectively [87].

However, most clinical grade neurosurgical operative microscopes are hampered by low adoption rates due to high cost, limited portability, limited operation flexibility, and lack of skilled professionals with technical knowledge. These neurosurgical fluorescence microscopes currently available in the market are not only expensive but also bulky, weighing hundreds of pounds [81, 85]. Resource poor environments may lack access to such advanced equipment. Many neurosurgeons continue to prefer resecting tumors while using affordable surgical eye loupes for their ease of operation. Unfortunately, most commercial surgical eye loupes are unable to visualize fluorescence because they lack excitation and fluorescence filtering systems.

1.2.3 Our Solutions

To overcome limitations of currently available neurosurgical imaging modalities, we innovatively integrated miniaturized light sources, flippable filters, and a recording camera to the eye loupes to generate a unique wearable fluorescence eye loupe device, namely “*FLoupe*” (US Patent Application #62/530,613, 2017), for real-time identification of MGs during surgery. The *FLoupe* is specifically designed for intraoperative visualization of brain tumor margins in clinical settings, with the aim of enhancing surgical procedures through fluorescence-guided surgery and intraoperative visualization of brain tumor margins. Two *FLoupe* prototypes were constructed for imaging of Fluorescein and 5-ALA, respectively. The wearable fluorescence imaging device was tested on tumor-simulating phantoms with varied fluorescence concentrations and tumor diameters, as well as in patients with primary malignant brain tumors. Comparable results were observed against the standard neurosurgical operative microscope (PENTERO® 900) with fluorescence kits.

Affordable and wearable *FLoupe* devices offer the capability to visualize both color and fluorescence images at a quality level equivalent to that of the large and expensive stationary operative microscopes. The wearable *FLoupe* device permits increased mobility, reduced obstruction, and quicker, more user-friendly operation, ultimately reducing surgical time and offering greater adaptability to the surgical environment compared to cumbersome neurosurgical operative microscopes.

1.3 Dissertation Organization

This dissertation consists of five chapters. **Chapter 1** introduces briefly the study background, significance, limitations of the current technologies and our solutions. More details are presented in the following 3 chapters (**Chapters 2-4**), which have been published in or submitted to peer-reviewed scientific journals.

Chapter 2 presents a modified scDCT system for 3-D reconstruction of CBF distributions and detection of LFOs within CBF variations. **Chapter 3** presents an innovative DSCT method with parallel computation for analyzing scDCT data to achieve fast and high-density 2-D mapping of CBF distributions at different depths without the need for 3-D reconstruction. **Chapter 4** presents an innovative wearable fluorescence eye loupe (*FLoupe*) device for intraoperative visualization of brain tumor margins. **Chapter 5** presents a summary of this dissertation, study limitations, my contributions, and future perspectives.

Overall, through three projects this dissertation demonstrated a variety of noncontact optical imaging technologies (scDCT, DSCT, and *FLoupe*) that enabled multiscale (rodents, piglets, and humans) and multimodality (blood flow and fluorescence) imaging of brain hemodynamics and function.

CHAPTER 2. DETECTION OF LOW FREQUENCY OSCILLATIONS IN NEONATAL PIGLETS WITH SPECKLE CONTRAST DIFFUSE CORRELATION TOMOGRAPHY (scDCT)

This chapter is presented based on a published paper: **Mohtasebi M**, Irwin D, Singh D, Mazdeyasna S, Liu X, Haratbar SR, Fathi F, Huang C, Saatman KE, Chen L, Yu G. Detection of low-frequency oscillations in neonatal piglets with speckle contrast diffuse correlation tomography. *Journal of Biomedical Optics*. 2023 Dec 1;28(12):121204-.

Abstract

Significance: Low-frequency oscillations (LFOs; <0.1 Hz) with respect to cerebral blood flow (CBF) have shown promise as an indicator of altered neurologic activity in the abnormal brain. Portable optical instruments have evolved to offer a noninvasive alternative for continuous CBF monitoring at the bedside compared to many large neuroimaging modalities. Their utilization for acquiring LFOs of CBF has though only been studied to a limited extent. The aim of this study is to optimize an innovative speckle contrast diffuse correlation tomography (scDCT) system for detection of LFOs within CBF variations.

Approach: The scDCT was optimized to achieve a higher sampling rate and a faster image reconstruction using a moving window 3-D reconstruction algorithm with parallel computation. Power spectral density (PSD) analysis was performed to investigate altered LFOs during transient global cerebral ischemia in neonatal piglets.

Results: Transient global cerebral ischemia resulted in reductions in both CBF and PSD compared to their baseline values.

Conclusions: Spontaneous LFOs, combined with CBF, provide a more comprehensive assay with the potential to clarify pathological mechanisms involved in brain injury. These results support scDCT's inclusion and application in the growing area of LFO analysis and

demonstrate its inherent advantage for neurological studies in preclinical and clinical settings, such as neonatal intensive care units.

2.1 Introduction

The brain is one of the most complex and metabolically demanding organs in humans. In spite of its relatively small size, the brain consumes approximately 20% of the oxygen in the body [1]. The function of the brain depends on cerebral blood flow (CBF) to deliver oxygen and glucose and to clear metabolic wastes. Blood pressure, neurogenic activity, and cardiac output all contribute to regulating CBF [88]. Rhythmic oscillations present in CBF are driven by cardiac cycle, respiratory motion, myogenic, neurogenic, and metabolic mechanisms [4]. Analysis of these oscillations reveals individual physiological contributions which arise at unique frequencies. In humans, ~ 1 Hz and ~ 0.3 Hz oscillations are associated with heartbeat and respiration, respectively, while those below 0.1 Hz are generally termed low-frequency oscillations (LFOs). LFOs also refer to Mayer waves [4-6]. Heartbeat and respiratory rates scale with the size of the species [9]. On the other hand, LFOs have not been shown to be dependent on size as studies have demonstrated that in piglets [10], monkeys [11], cats [12, 13], rabbits [14], and rodents [9, 15, 16], most LFOs exist below 0.1 Hz, which is the same frequencies as found in humans [4-6, 16]. This feature makes LFOs a potentially attractive target for producing translatable neurological findings.

Central nervous system disease or injury can result in abnormal CBF status and disruption to cerebral autoregulation. The cerebral vasculature network is affected by pathological disturbances, which impair dynamic oxygen and energy supply of neurons [89], thereby interfering with distributed patterns of synchronized neural activity

throughout the brain [90]. An increase in CBF (hyperperfusion of the brain) may result in increased intracranial pressure, headaches, and intraventricular hemorrhage. Insufficient CBF (hypoperfusion of the brain) may lead to depression of cerebral function as well as ischemic stresses on cerebral tissues. Such CBF abnormalities also impact rhythmic oscillations, including LFOs. Specifically, LFOs remain relatively stable in healthy brains, whereas changes in local LFOs are associated with compromised brain tissue [7]. Therefore, it is important to continuously monitor LFOs in order to gain a better understanding of pathological mechanisms underlying these diseases and to develop medical interventions [8]. Moreover, quantification of temporal correlations in LFOs across different regions of the brain (i.e., mapping functional connectivity (FC)) enables detecting regional neurovascular disorders [91]. There is then an unmet need for continuous neuroimaging tools that offer sufficiently high temporal and spatial resolutions to accurately detect LFOs and generate FC maps.

A few noninvasive or minimally invasive neuroimaging tools capable of measuring cerebral hemodynamics are available for LFO applications such as functional magnetic resonance imaging (fMRI) and optical methods. Blood-oxygen-level-dependent (BOLD) fMRI studies have revealed abnormal LFO amplitudes in patients with schizophrenia [31], mild cognitive impairment [32], Alzheimer's disease [33], major depressive disorder [34], sleep-deprived brain [35], traumatic brain injury (TBI) [36], and stroke [37], and has been utilized for cerebral FC analysis in study of cognitive neurosciences and clinical psychiatry/psychology [92, 93]. Despite these successes with fMRI, technical and logistical challenges remain such as low temporal resolution, motion artifact, electromagnetic compatibility, high cost, and lack of portability [94].

Optical imaging techniques offer noninvasive, fast, inexpensive, and portable means for cerebral hemodynamic and LFO assessments. Wide-field optical illumination with laser speckle contrast imaging (LSCI) [52-54, 95] and optical intrinsic signal imaging (OISI) [96, 97] map two-dimensional (2-D) distributions of CBF and cerebral oxygenation, respectively. Their penetration depth is limited to less than 1 mm, restricting their use to the superficial cortex in rodents and precluding their use for noninvasive cerebral imaging in larger animals such as piglets and in humans. Near-infrared (NIR) techniques such as near-infrared spectroscopy (NIRS) and diffuse correlation spectroscopy (DCS) allow continuous, noninvasive measurements of cerebral oxygenation and CBF, respectively, in deep brain tissues (up to centimeters) [27, 47]. For example, DCS was used to assess LFO amplitudes as a biomarker of neurologic injury during the acute period after cardiac arrest in a piglet model of pediatric cardiac arrest [10]. Correlations between the amplitudes of LFOs of CBF and the invasive biomarkers of neurologic injury obtained from microdialysis were found during the first four hours following cardiac arrest. Results from this study demonstrate that LFO is a promising biomarker for evaluating neurometabolic dysfunction in post-resuscitation period. Interests in study of LFOs in human subjects have also been increasing. For example, a hybrid NIRS/DCS instrument have been used to simultaneously detect LFOs of CBF, oxy-hemoglobin concentration ($[HbO_2]$), and deoxy-hemoglobin concentration ($[Hb]$) in cognitively healthy older subjects with high- or low-risk for developing cerebrovascular disease [46, 47]. The LFO amplitudes in the high-risk group were lower than those in the low-risk group [46]. Studies using functional NIRS (fNIRS) [40, 98] have shown impairments in brain FC maps [99, 100] and LFO amplitudes [101] in patients with cerebrovascular diseases compared to healthy controls. Using high-

density diffuse optical tomography (HD-DOT) with numerous sources and detectors [7, 28, 29], abnormal amplitudes of LFOs and FC maps of cerebral oxygenation in occipital cortices were obtained from premature infants [7].

While these diffuse optical systems show promise for detecting brain LFOs, there remain several limitations. NIRS/DCS systems suffer from limited numbers of discrete light sources and detectors, thereby taking sparse source-detector (S-D) pair measurements over a region of interest (ROI). This limits spatial resolution [48] and head coverage, thus inhibiting the localization of activations from regionally distributed brain functions [49]. Cerebral signals collected using NIRS/DCS methods are also inherently influenced by partial volume effects from overlayer tissues (scalp and skull) [46, 47], causing the difficulty to discriminate the brain signal of interest. HD-DOT systems in particular have received much attention with regards to improved spatial resolution and brain signal differentiation [7, 29, 50]. Nonetheless, extending the field-of-view (FOV) with fiber-based HD-DOT contact measurement systems to gain a more complete view of the brain is hampered by complications with optical fiber coupling to heads and cap design, especially for the heads of small and fragile newborn infants [7, 29, 50].

Recently developed speckle contrast diffuse correlation tomography (scDCT; US Patent #9/861,319, 2018 [20]) technology provides a noninvasive, fully noncontact, low-cost, and portable tool for high-density 3-D imaging of blood flow distributions in deep tissue volumes (up to ~10 mm) [55-57]. Importantly, this device remedies many previous limitations while offering direct CBF imaging for potential LFO assessments. In contrast with the NIRS, DCS, and HD-DOT systems using discrete detectors, scDCT uses a complementary metal-oxide semiconductor (CMOS) camera with thousands of pixels to

serve as parallel 2-D detectors, which dramatically increases the sampling density and enables a wide FOV. The light source is directed to an electronic-controlled galvo-mirror which can rapidly scan the FOV with flexible patterns of desired source density. These benefits are combined with a unique finite-element-method (FEM)-based reconstruction technique capable of incorporating complex surface geometries and known tissue properties [64, 102, 103]. Moreover, noncontact scDCT manages large numbers of sources and detectors and alleviates the need for complicated head helmet design, thus resulting in straightforward applications on subjects with different scales/sizes including small animals and preterm infants. In fact, case studies have already successfully demonstrated the scDCT usage for continuous and longitudinal imaging of CBF distributions in tissue phantoms; *in-vivo* cerebral tissues of rodents undergoing CO₂ inhalation and unilateral/bilateral ligations of common cerebral artery (CCA); neonatal piglets with CCA ligations and intraventricular hemorrhage (IVH); and sleeping preterm infants without scalp preparation through transparent incubator wall [55, 59, 60, 62, 104]. While these applications illustrate scDCT capability in identifying localized CBF responses across many subject sizes, the cited studies did not incorporate detection of LFOs.

The goal of the present study was to optimize the scDCT system for the detection of LFOs within CBF variations. Neonatal piglets were selected as model subjects due to their mid-range head size, high anatomical similarity and translational potential to human neonates, and our recent success with original scDCT techniques for comparisons [55]. The numbers of scanning sources and detectors in the scDCT were optimized to balance temporal and spatial resolutions of CBF imaging to examine regional brain responses and derive LFOs after signal filtering. A moving window 3-D reconstruction method was

adapted to achieve a fast sampling rate of 5 Hz, which is much higher than that with conventional reconstruction method (e.g., 0.2 Hz) [18, 55]. This sampling rate (5 Hz) is faster than typical cardiac and respiratory rates in neonatal piglets (<2.5 Hz), thus allowing removal of their contributions to CBF signals using simple lowpass filters. Moreover, reconstruction of a single 3-D image in previous studies took minutes to hours depending on the size of mesh nodes [55, 64, 105, 106]. In response, a new 3-D reconstruction algorithm using parallelization functionalities in MATLAB (MathWorks) was developed to achieve a sizable increase in reconstruction speed while maintaining reconstruction quality. As a result, computation time for 3-D reconstruction in this study was reduced from 15 minutes to 50 seconds. With these notable improvements, LFOs in piglet brains were successfully isolated and quantified by the optimized scDCT technique. This pilot preclinical study served as a vital and straightforward step towards using scDCT to map cerebral FC maps in human newborns.

2.2 Materials and Methods

2.2.1 Animal Preparations and Experimental

All experimental protocols in animals were approved by the Institutional Animal Care and Use Committee (IACUC) at the University of Kentucky. Two male neonatal piglets (Age: 32 days old) were purchased through the Division of Laboratory Animal Resources (DLAR) from the College of Agriculture Swine Center, University of Kentucky. Their genetic background included 62.5% Landrace, 25% Large White, and 12.5% Yorkshire. The two piglets were housed together in one dedicated room in a pigpen, with the support of a heat lamp and towel-covered floor. They were fed ad libitum with milk replacer for the first postnatal week, and gradually transitioned to pellet food at 2-3 weeks.

To study LFO variations, transient global cerebral ischemia was induced in the two neonatal piglets (Figure 2.1). The piglets were fasted for at least 4 hours before surgery to avoid reflux of stomach contents. Piglets were intubated with a pediatric endotracheal tube (internal diameter: 3 mm) and maintained under anesthesia with 1.5% to 2% isoflurane. Following previous studies in neonatal piglets [55], the anesthetized animal was placed prone and its head secured on a customized stereotaxic frame. The animal's body was wrapped with an electric heated blanket under the surveillance of rectal thermometer to avoid hypothermia. A multi-channel respirator-oximeter sensor (8400, Smiths Medical) was used to record heartbeat per minute (BPM), respiration per minute (RPM), end-tidal carbon dioxide (EtCO₂), and peripheral artery blood oxygen saturation (SpO₂).

Both piglets underwent transient unilateral and bilateral CCA ligations to create sequential decreases in CBF within the left and right cerebral hemispheres. After hairs on the head and ventral cervical skin were shaved with a clipper and cleaned with hair cream, the skin was disinfected with betadine and wiped with 70% ethanol. The animal was laid supine, and a 5 cm midline incision was made in the cervical area. The skin was retracted with four customized surgical hooks for better exposure of the surgical area. The underlying tissue was separated with blunt dissection until both CCAs were exposed. A 6-0 braided nylon suture was placed around each CCA, and a loose knot was made on each suture without disrupting blood flow to the brain. The piglet was then laid prone. A 50 × 50 mm² C-shape incision was made on the scalp to expose the skull. After a baseline measurement of scDCT for 5 minutes, the right knot was tightened to occlude the right CCA for ~5 minutes, followed by tightening the left knot for ~2 minutes to induce a transient global cerebral ischemia (i.e., both right and left CCA occlusions). The left and

right knots were then released sequentially, allowing restoration of blood flow to the brain (i.e., recovery phase). After the restoration of CBF from transient global cerebral ischemia, the piglet was euthanized with 100% CO₂ for ~4 minutes.

2.2.2 scDCT System for Data Acquisition

Details about scDCT techniques for blood flow measurements are available in our previous publications [55, 59, 60, 62, 103, 106-108]. Briefly, a high-speed scanning galvanometer mirror positioning system (maximum scan angle: $\pm 12.5^\circ$, switching time < 1 ms, GVS002, Thorlabs) remotely and sequentially delivered coherent focused-point NIR light (780nm, CrystaLaser) to multiple source positions on the tissue surface for boundary data acquisition (Figure 2.1a). An adjustable iris diaphragm (SM05D5, Thorlab) was placed into the source path to optimize the intensity and spot size of incident light. A scientific CMOS (sCMOS) camera (Pixels: 2048×2048 ; Frame rate: 30/sec; Quantum-efficiency: 50% @800 nm, ORCA-Flash4.0, Hamamatsu Photonics) was used as a high-density 2-D detector array to collect re-emitted light from the tissue for measures of spatial diffuse speckle contrasts in a selected ROI. The movement of red blood cells in the measured tissue volume produced spatial fluctuations of laser speckles captured by the sCMOS camera with a typical exposure time of 2 ms. A zoom lens (Zoom 7000, Navitar) was connected to the camera for adjusting the size of ROI (Figure 2.1b). A long-pass filter (> 750 nm, #84-761, EdmundOptics) was installed in front of the zoom lens to reduce the impact of ambient light. A pair of polarizers were added across the source and detection paths to reduce specular reflection directly from the scanning light sources on tissue surface.

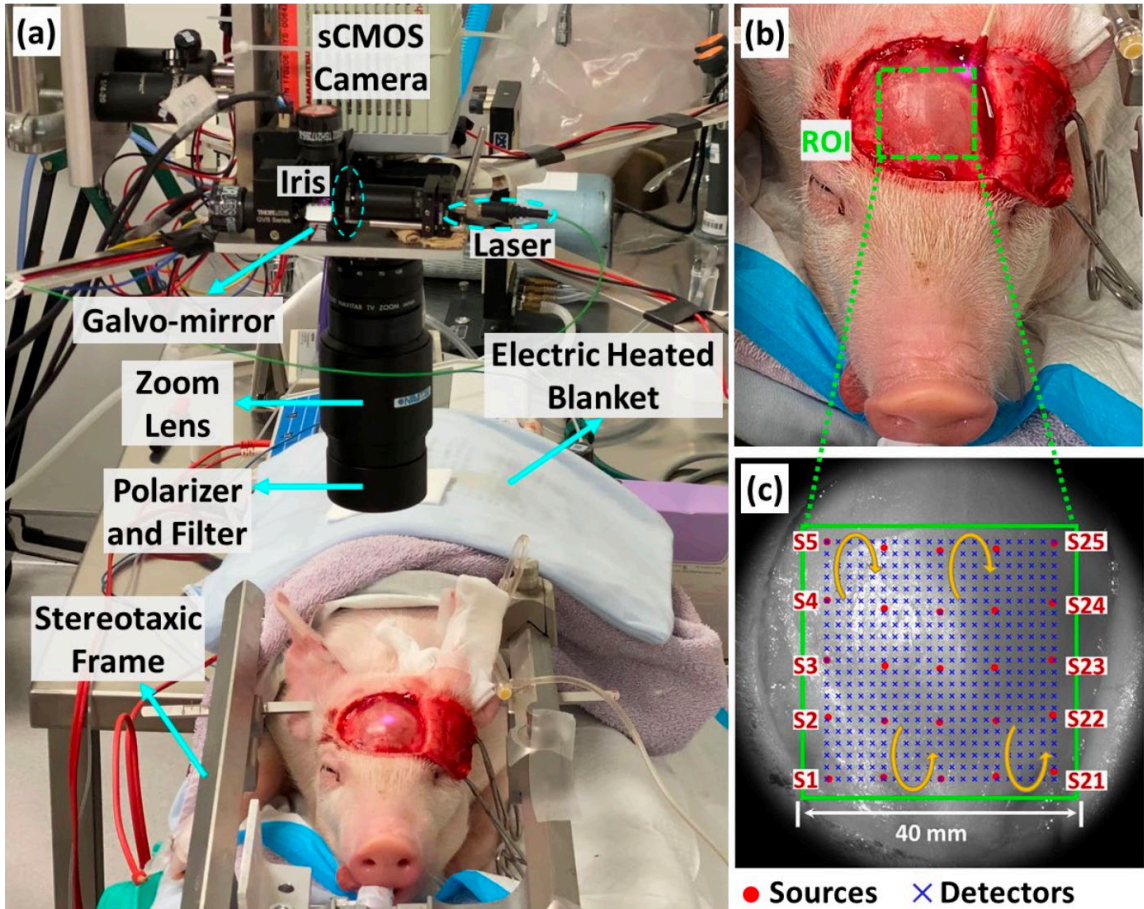


Figure 2.1: Experimental setup for continuous CBF monitoring of neonatal piglets during transient global ischemia.

(a) The anesthetized piglets were secured on a stereotaxic frame. A respirator-oximeter probe was clipped on the ear to acquire BPM, RPM, EtCO₂, and SpO₂. The noncontact scDCT was set up overhead and used for 3-D imaging of rCBF distributions. (b) For scDCT, an ROI of 40 × 40 mm² was projected on the intact skull of piglet head without the need of an invasive transcranial window. (c) The ROI was covered by evenly distributed 5 × 5 sources (scanned) and 21 × 21 detectors (grouped pixels).

The noncontact scDCT system was adjusted above the piglet to cover a ROI of 40 × 40 mm² on the head after skull exposure and before CCA occlusion commencement. The continuous data acquisition procedure consisted of sequentially scanning a set of 5 × 5 source locations on the ROI in a cycling fashion (Figure 2.1c). The total sampling time for scanning over 25 source positions was 5 seconds (0.2 seconds per source position). For

each source position, the sCMOS camera, as a 2-D detector array, output a raw intensity image.

The power of incident point light that reached tissue surface from the scDCT was less than 0.5 mW, according to the measurement by a power meter. This low level of power is considered safe according to the American National Standards Institute standard under the Accessible Emission Limit Class 3R classification [60]. Moreover, eyes of anesthetized piglet were always closed during scDCT measurements. Thus, the point light scanned over the selected ROI on the head and never shined on the eyes. Nonetheless, further eye protection will be made in the future by placing a protective eyewear on their eyes.

2.2.3 Boundary Data Processing for CBF

For 3-D reconstruction of CBF, source and detector positions on the mesh surface must be supplied. To precisely find actual source location, the intensity image (Figure 2.2a) was first converted to a binary image (Figure 2.2b). This was done by replacing all intensity values above a globally determined threshold with “1” and setting all other values to “0”. The threshold value was determined by Otsu’s method to minimize the intraclass variance of the thresholded black and white pixels [109]. After thresholding, those thresholded pixels with a value of “1” that connected to 8 pixels in local neighborhoods (so called 8-connected) were found and grouped together. In this automatic process, the *bwlabel* built-in function in MATLAB was employed to label the connected components in the binary image. By setting the ‘conn’ parameter in the *bwlabel* function to 8, eight neighboring pixels were determined. Then the *regionprops* built-in function with the 'Area' property was applied to compute the connected area, labelled as pixel numbers. The area with the maximum number of pixels was identified using the max function in MATLAB and other

areas were then removed from the 2-D binary image. Morphological operators such as opening, closing, and filling were then applied to the binary image for removing thin protrusions and isolated areas to reduce noises (Figure 2.2c). Finally, the centroid and radius of the point source were determined by estimating the center of the remaining largest area using the *regionprops* function with the 'Centroid' property (Figure 2.2d). This automatic process was repeated for all source locations (Figure 2.2e).

After finding these source locations on the X-Y plane, 441 detectors (21×21) were then evenly distributed between the 25 sources in the selected ROI of $40 \times 40 \text{ mm}^2$ to cover both hemispheres (Figure 2.1c). With this S-D configuration, the distance between two adjacent detectors was 2 mm. This configuration allowed to arrange 441 detectors on the ROI without any overlap and balanced between the spatial resolution and computation time. Moreover, S-D pairs with signal-to-noise ratios (SNRs) below 3 (linear scale) or above 90% of saturated intensity were excluded from the data analysis. The SNR was calculated by the ratio of I/I_{noise} , where I and I_{noise} denote the detected light intensity and dark noise of the camera, respectively.

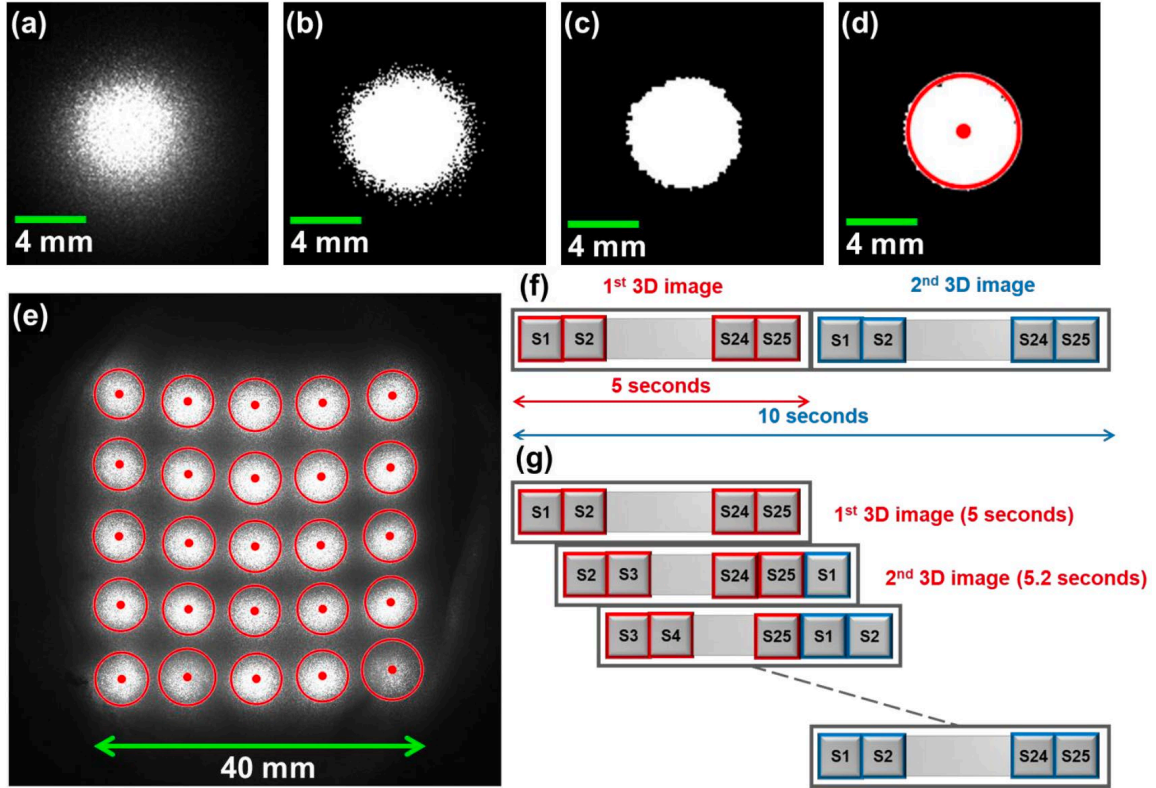


Figure 2.2: scDCT image processing for determining source locations and reconstruction steps for generating 3-D CBF images.

(a) A raw image captured by the camera. (b) The raw image from (a) converted to a binary image, derived by replacing all values above a globally determined threshold with “1” and setting all other values to “0”. (c) The object from (b) with the maximum number of connected pixels where morphological operators were applied to remove the noise from the image. (d) The centroid and radius of the point source was determined by estimating the center of mass for the remaining object in (c). This process was performed on all raw images to determine each source location. (e) 25 raw images with their centroid location were added for presenting purpose. (f) Conventional reconstruction paradigm: each 3-D CBF reconstruction was performed after fully updated boundary data was available (every 5 seconds). (g) Moving window reconstruction method: the first 3-D image reconstruction took 5 seconds. However, a new 3-D CBF image was then produced as soon as the raw image from one new source position was available, which occurred approximately every 0.2 seconds.

Another processing step was to extract boundary blood flow indices (*BFI*s) from measured speckle contrasts in the raw intensity images. The speckle contrast relies on the statistical property of spatial signal intensity distribution and was quantified by calculating the intensity ratio of standard deviation (σ) to mean ($\langle I \rangle$), i.e., $K = \sigma / \langle I \rangle$ in a pixel

window of 7×7 pixels on the sCMOS camera. We then averaged K values over 3×3 adjacent pixel windows with an area of $0.2 \times 0.2 \text{ mm}^2$ (as a single detector out of total 441 detectors) to improve SNRs. These speckle contrasts calculations were carried out at the effective source-detector distances of 6 to 16 mm, which corresponded to penetration depths up to ~ 8 mm (i.e., one half of the maximal S-D separation). Boundary BFI data were then obtained through a nonlinear relation with K . Derivation of this nonlinear relation can be found in our previous publication [103]. Boundary BFI at one S-D pair was extracted by iteratively minimizing the difference between the measured and theoretical speckle contrast, with total computation time of ~ 100 milliseconds.

2.2.4 3-D Image Reconstruction of CBF

The S-D pair coordinates, their boundary BFI s, and a solid volume tetrahedral mesh with 30 mm height, $60 \times 60 \text{ mm}^2$ bottom area, and 20K nodes were input into our FEM-based reconstruction program, i.e., modified near-infrared fluorescence and spectral tomography (M-NIRFAST), to generate a complete 3-D image of CBF distributions in the measured tissue volume [64, 102, 103]. The relative change in CBF (rCBF) was calculated by normalizing the reconstructed BFI to its corresponding baseline before physiological manipulations.

In the conventional reconstruction method, blood flow distribution in the measured tissue volume is reconstructed once a full source scanning cycle is completed. In other words, the intensity images for all source locations (i.e., 5×5 sources) should be available to generate a complete tomographic flow image (Figure 2.2f). Then the process is repeated for subsequent scanning cycles (i.e., another 5×5 sources). As a result, the total scanning time in previous studies using 5×5 sources was 5 seconds (0.2 Hz). Decreasing the number

of source positions would improve the temporal resolution. However, this would undesirably reduce the sampling density and SNRs. Alternatively, we implemented a new reconstruction method based on a moving window, where a tomographic reconstruction was obtained each time when one new source position data became available (Figure 2.2g) [18]. The moving window method updated data at each new source position every 0.2 seconds. As a result, the sampling rate of moving window method (5 Hz) was 25 times higher than the conventional reconstruction method (0.2 Hz). Using this higher sampling rate (5 Hz), carrier frequencies from cardiac and respiratory variations are unlikely to be aliased into LFO bands and can be removed with simple low-pass filters. Typical heartbeat and respiratory rates for piglets depend on their age and the anesthetic used. In our study, the heartbeat and respiratory rates for piglets were around 2.5 Hz and 0.5 Hz, respectively.

The reconstruction procedure itself is often an expensive task with high computational overhead. The higher sampling rate achieved in this study carried more burden of reconstructing for all time points. With original reconstruction procedures, processing such a magnified dataset size could prohibit practical use and longitudinal applications. To improve the speed of reconstructing multiple images, we parallelized the for-loop iterations using MATLAB's *parfor* control flow statement available in the Parallel Computing Toolbox™. This was possible because 3-D reconstructions of multiple rCBF images were independent, thus allowing to execute iterative calculations simultaneously. Our approach utilized powerful computers at the University of Kentucky High-Performance Computing (HPC) Center to achieve fast parallel computations of Jacobian matrices across multiple S-D pairs and iterative solvers [64, 102, 103]. The computer configuration was Intel® Xeon® Gold 6252 high performance server microprocessor, 16

CPU cores @ 3.70 GHz (Max Turbo Frequency). For a single 3-D image reconstruction of CBF distribution in the slab mesh with total mesh nodes of 20K as used in this study, the sublimated speed and memory efficiency led to 18 times reduction of computation time (from 15 minutes to 50 seconds).

2.2.5 Power Spectral Density (PSD) Analysis for LFO Intensity

The PSD analysis for LFO intensity quantification has been established in diffuse optical technologies including NIRS [7, 110] and DCS [10, 46, 47]. Following these methods, LFO intensities of CBF under different physiological conditions (i.e., resting baseline, right CCA occlusion, transient global ischemia, releasing left CCA occlusion, and sequentially releasing right CCA occlusion for recovery) were extracted from PSDs calculated by Welch's method in a non-parametric approach [47]. Specifically, the PSD was calculated as follows: $PSD = 1/(F_s \times N_{seg}) \sum \left| \text{FFT}_{X_{seg}}(f) \right|^2$, where F_s is the sampling frequency, N_{seg} is the number of segments, and $\text{FFT}_{X_{seg}}$ is the fast Fourier transform of the segmented signals [111]. Briefly, time-course rCBF dataset under each physiological condition at the sampling rate of ~5 Hz (frame per second) were first detrended using a built-in *detrend* function in MATLAB to obtain the best straight-line fit linear trend. The detrended rCBF data were then transferred into a Butterworth filter with a passband at the LFO range from 0.01 Hz to 0.1 Hz. Finally, the built-in *pwelch* function in MATLAB was used to generate the PSD over the LFO bandwidth.

To compare PSD levels across different phases of transient global cerebral ischemia, PSD at each phase was normalized to the area under-the-curve (AUC) of baseline PSD. The trapezoidal integration method in MATLAB built-in *trapz* function was used to

calculate the AUC of PSD. Half-width-at-half-maximum (HWHM) value was then determined from the normalized PSD by quantifying the half width of the frequency band in which the PSD was above half of its maximum value.

2.3 Results

2.3.1 rCBF and Vital Variations During Transient Global Ischemia

Figure 2.3 shows physiological changes measured by the scDCT and multi-channel respirator-oximeter during transient global ischemia in two neonatal piglet brains following the CCA occlusion protocol. Figure 2.3a shows rCBF data averaged over the ROI at the depth of 5 mm beneath the skull of Piglet #1, quantified by the moving window (blue curve) and conventional (red curve) reconstruction methods, respectively. Based on neonatal piglet head anatomy, the depth of 5 mm reaches the brain cortex [55]. During right CCA occlusion, rCBF declined, reaching $75\% \pm 11\%$ and $79\% \pm 4\%$ (mean \pm standard deviation in timeseries of rCBF values) of the baseline from the moving window and conventional reconstruction methods, respectively. Bilateral ligation further decreased rCBF to $63\% \pm 11\%$ (moving window) and $63\% \pm 6\%$ (conventional reconstruction), respectively. After sequentially releasing left and right ligations, rCBF values were $68\% \pm 11\%$ (moving window)/ $70\% \pm 5\%$ (conventional reconstruction) and $70\% \pm 12\%$ (moving window)/ $74\% \pm 5\%$ (conventional reconstruction), respectively. At the end of the experiment, euthanasia was induced by 100%CO₂ inhalation until heartbeat stopped. rCBF had an immediate but brief reactive hyperemic response, then dropped to a minimum of 7% (moving window)/ 9% (conventional reconstruction) by the conclusion. As expected, both the

moving window and conventional reconstruction methods portrayed similar trends over all protocol phases.

Figure 2.3d shows time-course changes in rCBF detected by scDCT during transient global ischemia in Piglet #2. Compared to Piglet #1, more pronounced decreases occurred during bilateral ligation as compared to unilateral ligation. Specifically, rCBF declined to $90\% \pm 12\%$ (moving window)/ $88\% \pm 2\%$ (conventional reconstruction) of the baseline during right CCA ligation and to $45\% \pm 7\%$ (moving window)/ $53\% \pm 8\%$ (conventional reconstruction) during bilateral ligation. Then rCBF increased to $68\% \pm 11\%$ (moving window)/ $72\% \pm 9\%$ (conventional reconstruction) during release of left ligation and $91\% \pm 11\%$ (moving window)/ $90\% \pm 3\%$ (conventional reconstruction) during release of right ligation, respectively. Transient reactive hyperemic responses were detected during the induction of euthanasia by 100%CO₂. rCBF dropped to 30% (moving window)/ 42% (conventional reconstruction) during the euthanasia, which were less dramatic than those observed in Piglet #1.

To summarize rCBF results from the two piglets, the model of sequential CCA ligations enabled prompt manipulation of rCBF. Right CCA ligation induced an instant reduction in rCBF and sequential bilateral occlusions of CCA resulted in a transient global cerebral ischemia. Sequential release of left and right CCAs allowed restoration of rCBF. These changes in rCBF are expected and consistent with previous findings in rodents and neonatal piglets during transient global cerebral ischemia [55, 59, 62]. While both methods showed similar trends, the moving window method with a higher sampling rate demonstrated larger variations in rCBF, which are likely associated with other physiological changes such as heartbeat and respiration rates. Importantly, the high

sampling rate of moving window method enabled the detection of LFOs without any interference from heartbeat and respiration.

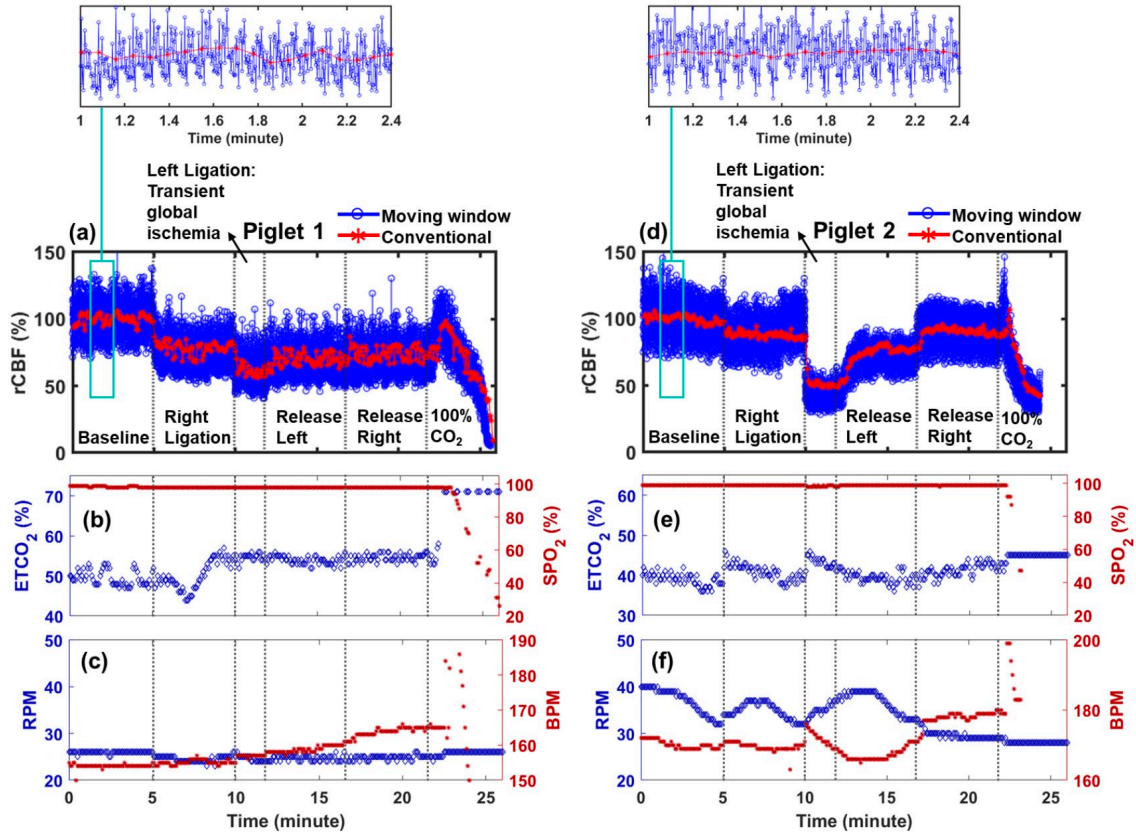


Figure 2.3: Measurement results from Piglet #1 and Piglet #2 during transient global ischemia.

(a) and (d) Time-course changes in rCBF measured by scDCT at 5 mm depth during sequential unilateral and bilateral CCA ligations. The experimental protocol included baseline, right CCA ligation, bilateral ligation (transient global ischemia), releasing of left ligation, releasing of both left and right ligations (recovery), and euthanasia (100% CO₂). Red curves indicate the time points where a 3-D CBF reconstruction was available with the conventional reconstruction method while blue curves indicate the time points with the moving window method. Two zoom-in magnified areas are shown to highlight the increased temporal resolution of the rCBF by the moving window method (blue). (b) and (e) Time-course changes in EtCO₂ and SpO₂. (c) and (f) Time-course changes in RPM and BPM.

Fluctuations of EtCO₂, SpO₂, RPM, and BPM during transient global ischemia are shown in Figure 2.3b, 2.3c for Piglet #1 and Figure 2.3e, 2.3f for Piglet #2. The increased CO₂ concentration (EtCO₂, blue dots in Figure 2.3b, 2.3e) along with the reduced O₂

concentration during euthanasia inhibited respiratory and cardiac functions, thus leading to large drops in rCBF (Figure 2.3a, 2.3d), SpO₂ (red dots in Figure 2.3b, 2.3e), and BPM (red dots in Figure 2.3c, 2.3f). Piglet #2 was found to have a marginal change in EtCO₂, which is consistent with the higher observed rCBF minimum upon euthanasia compared to Piglet #1. Unfortunately, data were not collected from the respirator-oximeter device during euthanasia of Piglet # 2 due to a technical problem with the device, but a BPM decline was confirmed by measuring the heartbeat with stethoscope. The RPM (blue dots in Figure 2.3c, 2.3f) response in Piglet #1 was negligible while that in Piglet #2 displayed a slow decrease throughout. These physiological variations resulting from the hypoxic challenge agreed with pathophysiological processes.

2.3.2 LFOs During Transient Global Ischemia

LFOs were isolated from moving window rCBF curves (Figure 2.3a, 2.3d blue curves) for each session of physiological conditions. The LFO range (<0.1 Hz) was identified through the power spectra of rCBF as shown in Figure 2.4. rCBF signals were taken from the baseline measurement interval before physiological manipulations. With the new moving window method, scDCT achieved a sampling rate of 5 Hz, which was sufficient to capture the heartbeat (2.5 Hz) and respiration rate (0.5 Hz). Apparently, high-frequency signals arising from respiration and cardiac cycles were aliased into the desired LFOs. Using low-pass filter, rCBF signals were re-analyzed for LFO isolation while filtering the artifactual signals unrelated to neural activity.

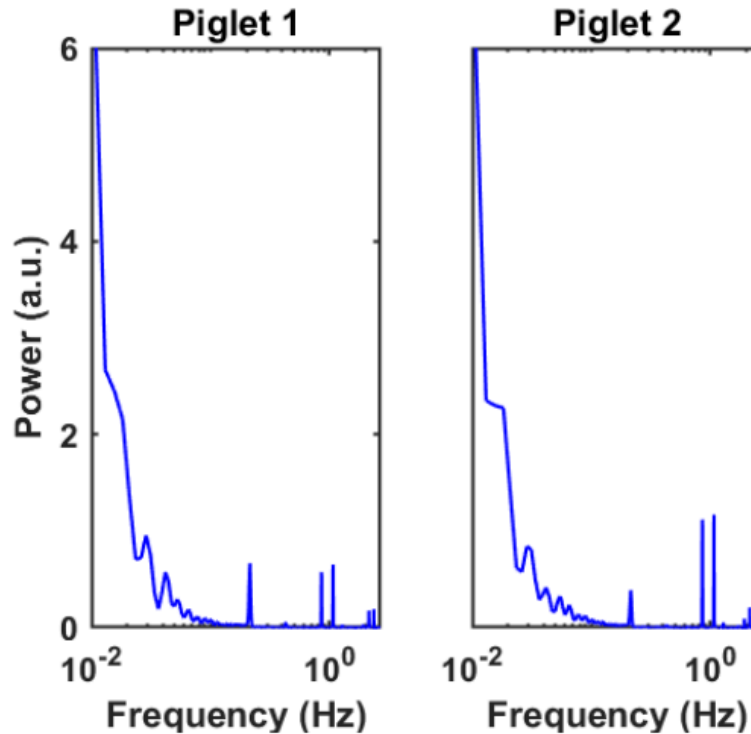


Figure 2.4: Power spectra of rCBF signals during baseline measurements.

Power spectra were determined from reconstructed rCBF at 5 mm beneath the skull as acquired using scDCT with the moving window reconstruction method. Baseline measurement preceded physiological manipulations (i.e., CCA ligations). LFOs (<0.1 Hz), heartbeat (2.5 Hz) and respiratory rate (0.5 Hz) were captured.

Figure 2.5 shows the time course for rCBF during baseline, right CCA occlusion, transient global ischemia, releasing the left CCA occlusion, releasing both left and right CCA occlusion, and euthanasia periods after detrending and LFO band-pass filtering (0.01 Hz to 0.1 Hz). Hemodynamic fluctuations during transient global ischemia and euthanasia periods exhibited marked differences. This positive finding verified LFOs as measured by the optimized scDCT have the potential for indicating abnormal cerebrovascular conditions.

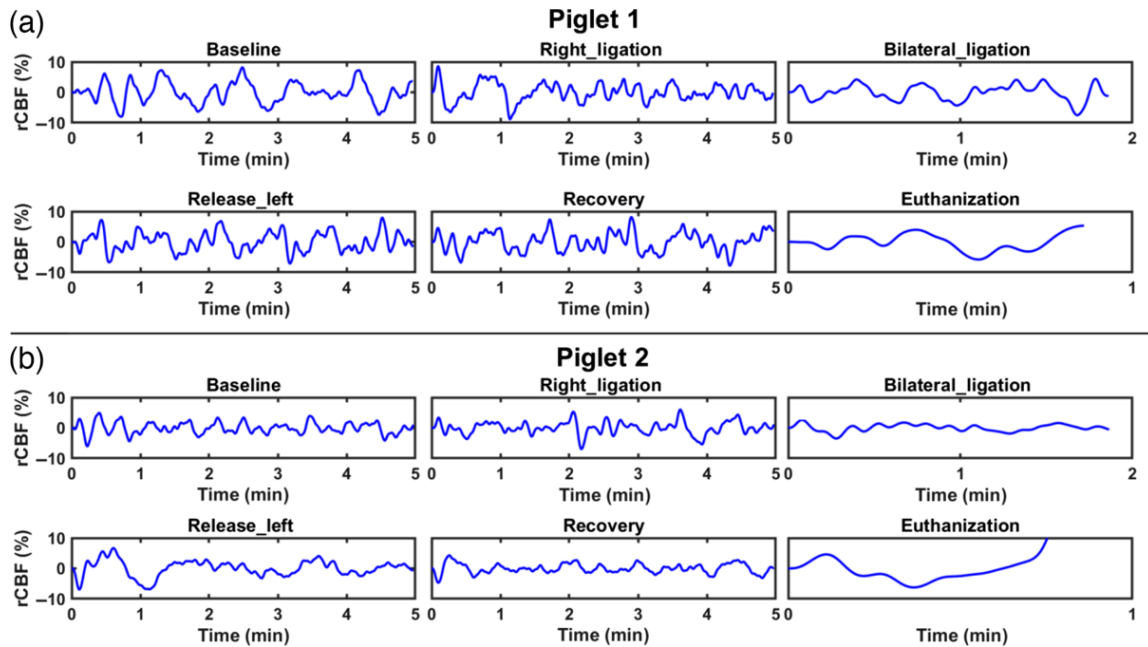


Figure 2.5: Detrended and band-pass filtered time course changes in rCBF over each interval for both piglets.

(a) Piglet #1 and (b) Piglet #2: Time course changes in re-analyzed rCBF, from 5 mm beneath the skull, during the periods of: baseline, right CCA ligation, bilateral ligation (transient global ischemia), releasing of left ligation, releasing of both left and right ligations (recovery), and euthanasia (100% CO₂). The detrended and band-pass filtered (0.01 Hz to 0.1 Hz) rCBF represents spontaneous activity that occurred within the piglet's brain.

2.3.3 PSD Changes in LFOs for Identification of Neurological Variations

To better characterize the potential of LFOs as a measure of abnormal neurological status, we calculated changes in PSD within the LFO range. Figure 2.6a and Figure 2.6b show normalized PSD distributions for both piglets. During the period of bilateral ligation, PSD decreased to ~35% of the baseline for both Piglet #1 and Piglet #2 (Figure 2.6c). Correspondingly, HWHM values increased from 0.026 Hz at the baseline to 0.042 Hz (1.6 times increase) and 0.031 Hz (1.2 times increase) in Piglet #1 and Piglet #2, respectively (Figure 2.6d). Alterations in PSD and HWHM are likely associated with impairments of autonomic nervous activities during transient global cerebral ischemia. After release of bilateral ligation, both PSD and HWHM recovered towards their baseline levels.

2.4 Discussion and Conclusions

Near-infrared diffuse optical instrumentation capable of noninvasively penetrating the deep brain offers a unique opportunity for CBF and LFO analyses [7, 40, 112]. Among various NIR instruments, noncontact scDCT enables 3-D imaging of CBF with flexible FOV and S-D arrangements for use across a wide range of subjects with varied head sizes within a low-cost package [55, 56, 59, 60, 62, 103, 108]. This system was, however, hindered for extracting LFOs due to an insufficient temporal sampling rate. The current study utilized a moving window 3-D reconstruction method with parallel computations to facilitate LFO studies. With this modified scDCT technique, a powerful tool has been made available for neurologic studies and neonatal applications. The results from the unique design and testing efforts in neonatal piglets are discussed below.

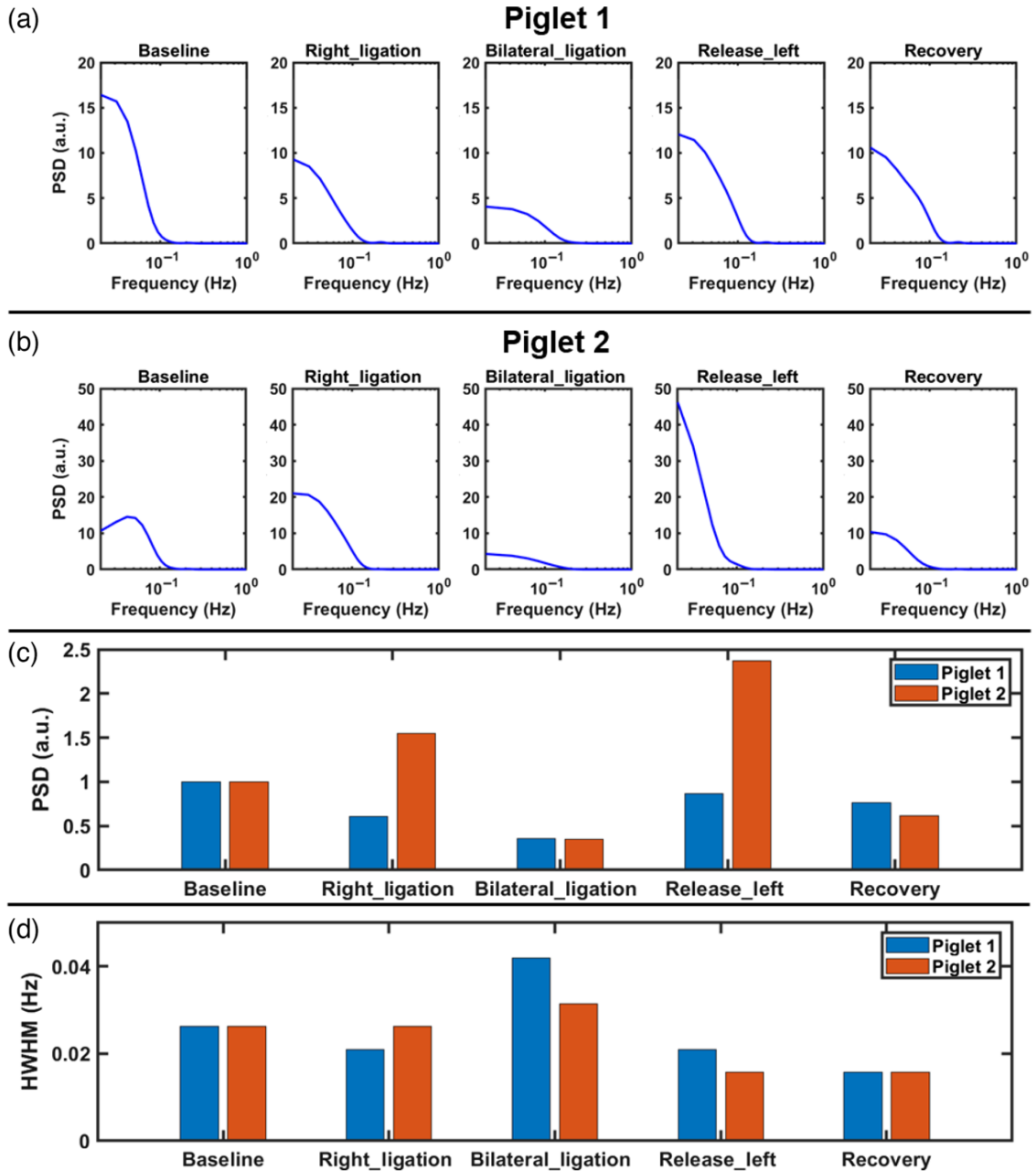


Figure 2.6: PSD analysis of LFOs in both piglets.

(a) and (b) Normalized PSD distributions from Piglet #1 and Piglet #2, respectively. PSDs were normalized to the area under-the-curve (ACU) of baseline PSD. (c) and (d) PSD and HWHM changes during different phases of transient global cerebral ischemia from Piglet #1 and Piglet #2, respectively.

A moving window 3-D reconstruction method was employed to increase the temporal resolution of scDCT (Figure 2.2g). As evidenced by the zoom-in results in Figure 2.3a (Piglet #1) and Figure 2.3d (Piglet #2), the moving window method introduced a

higher temporal resolution (5 Hz) as compared with the conventional method (0.2 Hz). More frequency components were observed suggesting increased sensitivity to underlying physiological variations, such as LFOs, as opposed to random noises and to the generally aperiodic pattern from the conventional method. It should be noted that the moving window method increased the temporal resolution 25 times compared to the conventional method at the expense of only utilizing data from one updated source location to generate a new image. Nevertheless, we were able to successfully measure and identify the higher frequency changes occurring in the blood flow responses during the ligation tests. This is expected as ligations have a far-reaching influence on the brain tissues and underlying physiological signals.

Moreover, a new 3-D reconstruction algorithm using parallelization functionality in MATLAB was developed for rapid image reconstruction while maintaining reconstruction quality. The completion time leveraged advance resources such as graphics processing units (GPUs) at the HPC. Technological advancements and their availability improve the accessibility and potency of these resources in the lab and clinic. Improvements in computation speed vary depending on factors such as mesh density, hardware specifics, and competing processes.

We created a perinatal disease model of transient global cerebral ischemia in neonatal piglets to test the ability of scDCT technique in detecting alterations in rCBF and LFOs. The transient global cerebral ischemia impacted entire brain hemodynamics. Despite the limited number of subjects, the observed large variations in rCBF during transient global cerebral ischemia (Figure 2.3) align with pathophysiological expectations and agree with previous study results [55, 59, 62]. The individual discrepancies in rCBF

amplitudes during transient global cerebral ischemia are likely due to individual heterogenous responses in rCBF and differences in pathological stresses.

Performing spectral analysis on rCBF data at baseline, common physiological frequency peaks (i.e., 2.5 Hz heartbeat and 0.5 Hz respiratory rate) and LFOs (< 0.1 Hz) were identified (Figure 2.4). The high temporal resolution of optimized scDCT (i.e., 5 Hz) is faster than typical cardiac and respiratory rates in neonatal piglets, allowing removal of their contributions to LFOs using simple lowpass filters. Thus, LFOs in the range of 0.01 Hz to 0.1 Hz were isolated from the high sampling rCBF curves for resting baseline, right CCA occlusion, transient global cerebral ischemia, releasing the left CCA, and recovery phase. There were apparent reductions in rCBF fluctuations in correspondence with the ligations and euthanasia (Figure 2.5). The bilateral ligation still retained an oscillatory nature whereas euthanasia took on a monotonic trend. Correspondingly, attenuations in LFOs during ligations and euthanasia were also observed (Figure 2.6). These observations are consistent with other studies reporting alterations in temporal and/or spectral characteristics of spontaneous LFOs following an ischemic stroke. For example, functional connectivity OISI has been applied to mice with transient middle cerebral artery occlusions [90]. LFOs of cerebral hemodynamic signals in the region of the brain affected by an ischemic stroke exhibit reduced fluctuations and significant reductions in their power spectra [90]. According to a study conducted using the HD-DOT [7], power spectra of LFOs are markedly lower in an infant who suffered a left occipital stroke than healthy term-born infants [7].

Although rCBF and LFOs responses to transient global cerebral ischemia were coupled in this study, power spectral analysis of the detrended and filtered rCBF (i.e.,

LFOs) provided new insights into neurologic status of the brain [113]. During transient global cerebral ischemia, PSD values reduced dramatically compared to their baselines (Figure 2.6c), indicating possible impairments in autonomic nervous activities. Meanwhile, HWHM values increased (Figure 2.6d), suggesting LFO shifts to higher frequencies. These frequency shifts may be related to cerebral autoregulation mechanisms in response to dramatic variations in rCBF during transient global cerebral ischemia. Previous studies have found that different frequency bands within the LFO range are associated with different regulatory mechanisms including metabolic, neurogenic, and myogenic regulations [114-116]. Further investigations on more subjects are needed to draw solid conclusions based on these new findings in PSD and HWHM alterations.

We note that our innovative scDCT system can be further improved in the future to map the brain's resting-state functional connectivity (rs-FC). The rs-FC can be assessed by quantifying temporal correlations in LFOs across different regions of the brain, which enables depicting the brain's functional organization [40]. As the moving window method only uses a local update of information, the ability to capture highly distributed changes over the brain requires greater customization and consideration. To address this, the sampling rate of the scDCT should be further increased to remove entirely artifactual signals unrelated to neural activity. They may manifest as structured noise that introduces spurious correlations in the data and thus influencing results. Use of a high-quality CCD or scientific CMOS (sCMOS) camera with faster sampling rate and higher sensitivity would improve data acquisition, detection sensitivity, and probing depth. It is possible to further reduce the sampling time by modifying the number of sources, distribution pattern of the sources, and simultaneously illuminating multiple sources at the same time in

different brain regions. In the future, it is planned to combine rCBF measurement with rs-FC mapping as well as the power of LFOs to perform novel functional neuroimaging with scDCT devices.

Some limitations exist that were not otherwise mentioned. One such limitation is that the optical properties (e.g., absorption and scattering coefficients) are known to have an influence on rCBF calculations [117]. Optical properties are often assumed from the literature. Recently, a two-step fitting algorithm successfully extracted tissue absorption and blood flow simultaneously using the scDCT arrangement [118]. This solution can assist in improving flow reconstruction accuracy. The utilization of multiple wavelengths of source light makes it possible to measure CBF as well as cerebral oxygenation and derivatives (e.g., tissue oxidative metabolism) [117, 119, 120]. By providing a more comprehensive assay, which includes fluctuations in hemoglobin concentrations ($[HbO_2]$ and $[Hb]$) in addition to rCBF, it may be possible to clarify the disease-related hemodynamic and metabolic mechanisms involved in the disruption of brain networks as a result of disease. Also, we note that the PSD interpretation of LFOs used here is only one approach and other options exist and will be studied for appropriateness. For example, normalization of LFOs to the full frequency range has been used in fMRI to increase sensitivity and specificity [121].

In this paper, the design of a high-speed scDCT imaging and reconstruction technique successfully increased effective temporal sampling, reconstructed full 3-D data sets quickly, filtered non-LFO and undesired signal contributions, extracted LFOs from deep brain CBF, and characterized the LFOs through PSD throughout CCA ligation phases on neonatal piglets. The results provide a basis for scDCT instrument inclusion and

applicability in the growing area of LFO analysis while bringing with it many inherent advantages for neurologic studies and potential clinical applications. Further studies with a greater number of subjects and better localization of neurological events and responses (e.g., mapping rs-FC) are needed to ensure these findings and conclusions in this pilot study.

CHAPTER 3. DEPTH-SENSITIVE DIFFUSE SPECKLE CONTRAST TOPOGRAPHY (DSCT) FOR HIGH-DENSITY MAPPING OF CEREBRAL BLOOD FLOW IN RODENT

This chapter is presented based on a submitted manuscript: **Mohtasebi M**, Singh D, Liu X, Fathi F, Haratbar SR, Saatman KE, Chen L, Yu G. Depth-Sensitive Diffuse Speckle Contrast Topography (DSCT) for High-Density Mapping of Cerebral Blood Flow in Rodents. Neurophotonics. 2023 May 01.

Abstract

Significance: Frequent assessment of cerebral blood flow (CBF) is crucial for diagnosis and management of cerebral vascular diseases. In contrast to large and expensive imaging modalities such as nuclear medicine and MRI, optical imaging techniques are portable and inexpensive tools for continuous measurements of cerebral hemodynamics. Recent development of an innovative noncontact speckle contrast diffuse correlation tomography (scDCT) enables 3-D imaging of CBF distributions. However, scDCT requires complex and time-consuming 3-D reconstruction, which limits its ability to achieve high spatial resolution without sacrificing temporal resolution and computational efficiency. The aim of this study is to investigate a new diffuse speckle contrast topography (DSCT) method with parallel computation for analyzing scDCT data to achieve fast and high-density 2-D mapping of CBF distributions at different depths without the need for 3-D reconstruction.

Approach: A new moving window method was adapted to improve the sampling rate of DSCT. A fast computation method utilizing MATLAB functions in the Image Processing Toolbox™ and Parallel Computing Toolbox™ was developed to rapidly generate high-density CBF maps. The new DSCT method was tested for the spatial resolution and depth sensitivity in head-simulating layered phantoms and *in-vivo* rodent models.

Results: DSCT enables 2-D mapping of particle flow in the phantom at different depths through the top layer with varied thicknesses. Both DSCT and scDCT enable the detection

of global and regional CBF changes in deep brains of adult rats. However, DSCT achieves fast and high-density 2-D mapping of CBF distributions at different depths without the need of complex and time-consuming 3-D reconstruction.

Conclusions: The novel depth sensitive DSCT method has the potential to be used as a noninvasive, noncontact, fast, high resolution, portable, and inexpensive brain imager for basic neuroscience research in small animal models and for translational studies in human neonates.

3.1 Introduction

Cerebral blood flow (CBF) is vital to maintain proper cerebral perfusion and supply the brain with necessary oxygen and metabolic substrates [2]. Cerebral hyperemia (a higher CBF than normal) raises intracranial pressure, which may compress and damage delicate brain tissue. On the other hand, cerebral ischemia (a lower CBF than normal) may directly result in the death of brain cells. Measurement of CBF is critical for both the diagnosis and therapeutic monitoring of many cerebral vascular/cellular diseases including stroke, head trauma, and shock [3]. Imaging of CBF with a high temporal-spatial resolution enables monitoring of fast cerebral hemodynamic changes and spatially distributed brain function [17, 18]. Moreover, acquiring data with high resolution allows temporal-spatial averaging to improve the signal-to-noise ratio (SNR).

A variety of neuroimaging tools are used for CBF assessments including nuclear medicine, magnetic resonance imaging (MRI), ultrasonic techniques, and optical methods. Transcranial Doppler ultrasonography measures blood flow velocities in large vessels, which may not reflect CBF in the microvasculature. In contrast to large and expensive imaging modalities such as nuclear medicine and MRI, optical imaging techniques based

on dynamic light scattering are portable and inexpensive tools for continuous and fast measurements of cerebral hemodynamics in brain microvasculature. Near-infrared (NIR) diffuse optical technologies such as near-infrared spectroscopy (NIRS) and diffuse correlation spectroscopy (DCS) with continuous point source illumination and photodetector detection enable noninvasive measurements of cerebral blood oxygen saturation (StO₂) and CBF respectively in relatively deep tissues (up to centimeters) [44, 64, 105, 122-126]. However, most NIRS/DCS systems use limited numbers of discrete light sources and detectors, leading to sparse source-detector (S-D) pair measurements and lack of combinations of high temporal-spatial resolution and large field-of-view (FOV) needed for assessing spatially distributed cerebral hemodynamics and function.

Use of a charge-coupled-device (CCD) or complementary metal-oxide-semiconductor (CMOS) camera with thousands of pixels as a 2-D detector array provides high-density and fast parallel sampling [51]. For example, laser speckle contrast imaging (LSCI) with the widefield illumination and CMOS/CCD camera detection enables high-resolution 2-D mapping of CBF distributions on superficial cortexes of rodents (mice and rats), although rodents' scalps must be retracted and an invasive cranial window is needed on rats due to the limited imaging penetration depth (<1 mm) [52-54].

There have been recent advancements toward using point illumination for deep tissue penetration and CCD/CMOS camera for high-density 2D detection of diffuse laser speckle contrasts to facilitate 3D tomographic reconstruction of blood flow distributions. For example, speckle contrast optical tomography employed focused point illuminations and CCD detection of spatial diffuse speckle contrasts for 3D image of CBF distributions in tissue-simulating phantoms and rodents [18, 127, 128]. We have developed an innovative

speckle contrast diffuse correlation tomography (scDCT; US Patent #9/861,319, 2018 [20]) method, which provides a noncontact, inexpensive, and portable tool for 3D imaging of blood flow distributions over a large FOV in relatively deep tissue volumes (up to ~10 mm depth) [55, 57, 59, 60, 62, 103, 104, 108, 129, 130]. These advanced CCD/CMOS-based techniques are inherently founded upon the same concept despite differences in nomenclature and technological evolution.

In the scDCT, a galvo mirror rapidly (switching time < 1 ms) delivers continuous, coherent, point NIR light (for deep tissue penetration) to many source positions on a selected FOV with a flexible scanning pattern/density. In contrast with the NIRS and DCS systems using discrete photodetectors, scDCT uses a high-resolution scientific CMOS (sCMOS) camera with more than one million pixels as a parallel 2-D detector array, which dramatically increases the sampling density and area of FOV. Boundary data from the selected S-D pairs are input to a unique finite-element-method (FEM)-based reconstruction algorithm for 3-D imaging of CBF distributions [55, 57, 59, 60]. However, the FEM-based 3-D reconstruction algorithm involves solving a forward problem to calculate light propagation through the tissue and an inverse problem to fit tissue optical properties [64, 65]. The FEM-based 3-D reconstruction is complex and time consuming, taking from several minutes to hours to generate one single CBF image. Increasing numbers of sources and detectors improves spatial resolution with the expenses of low temporal resolution and high computational overhead/time for 3-D reconstruction, thereby prohibiting real-time applications [65]. Moreover, 3-D image reconstruction is an ill-posed inverse problem due to the nonlinear light propagation in biological tissues and limited number of S-D pairs for

boundary data measurements [131]. As such, even small errors in boundary measurements or reconstruction modelling may result in large errors in reconstructed images [131].

To overcome these limitations, we investigated an alternative, depth-sensitive diffuse speckle contrast topography (DSCT) method for analyzing scDCT data to achieve fast and high-density 2-D mapping of CBF distributions at different depths without the need of complex and time-consuming 3-D reconstruction. In contrast to solving the forward and inverse problems in 3-D reconstruction, DSCT simply computes blood flow indices (BFIs) for the selected S-D pairs with different distances. According to the photon diffusion theory [132], the penetration depth of diffusive light in biological tissues is approximately half of the S-D separation. By selecting S-D pairs with shorter or larger separations according to the imaging depth of interest, DSCT differentiates short and long photon paths through the measured tissue volume, thus generating depth-sensitive 2-D maps of BFIs. Apparently, the DSCT method involves only solving forward problems with boundary data for 2-D mapping, which is simpler, faster, and less sensitive to boundary measurement noises than the scDCT with 3-D reconstruction. As such, a fast computation method that takes advantage of the Image Processing Toolbox™ and Parallel Computing Toolbox™ functions in MATLAB (MathWorks) has been developed for rapidly calculating high-density blood flow maps.

To test the new DSCT method and compare it with other established methods such as LSCI, a hybrid system combining scDCT and LSCI was assembled. To assess the depth sensitivity of DSCT method, new head-simulating layered phantoms with known optical/geometric properties were designed and fabricated using 3-D printing technique. Results from the DSCT and LSCI methods were compared to assess their performances.

Furthermore, 2-D mapping of CBF variations was performed by the DSCT in rats during CO₂ inhalations (resulting in global CBF increases) and during unilateral and bilateral transient ligations of carotid arteries (resulting in regional CBF decreases).

3.2 Materials and Methods

This Method section starts with the introduction of a hybrid system combining scDCT and LSCI for comparison measurements (Section 3.2.1). Since the hardware for data acquisition in scDCT and DSCT are essentially same, terminologies of “scDCT” and “DSCT” are used interchangeably in this paper for hardware introduction. Data analyses for the LSCI (Section 3.2.2) and new DSCT (Section 3.2.3) are then described separately. Phantom tests (Section 3.2.4) and *in-vivo* experiments in adult rats (Section 3.2.5) are followed to assess the performance of DSCT.

3.2.1 Hybrid DSCT and LSCI System

The DSCT acquires boundary data using the same hardware as the scDCT (Figure 3.1a), which has been reported extensively in our previous publications [55, 57, 59, 60, 62, 103, 106-108]. Briefly, a high-speed scanning galvanometer mirror positioning system (maximum scanning angle: $\pm 12.5^\circ$; switching time: < 1 ms; GVS002, Thorlabs) remotely and sequentially delivered coherent focused-point NIR light (780 nm, CrystaLaser) to multiple source positions on the region of interest (ROI) (Figure 3.1b and Figure 3.1c). The point light was focused on the tissue surface via an achromatic lens (AC127-019-B, Thorlabs) and light spot size was adjusted and minimized using a lever-actuated iris (SM05D5, Thorlabs). A sCMOS camera (pixels: 2048×2048 ; frame rate: 30/sec; quantum-efficiency: 50% @800 nm; ORCA-Flash4.0, Hamamatsu Photonics) was used as

a high-density 2-D detector array to collect re-emitted diffuse light from the tissue for boundary measurement of spatial diffuse speckle contrasts in the selected ROI. A zoom lens (Zoom 7000, Navitar) connected to the camera for adjusting camera's focus on the ROI. A high-performance long-pass filter (>750 nm; #84-761, EdmundOptics) was used to minimize the influence of ambient light on DSCT measurements [129]. No obvious influence of ambient light was observed on the obtained raw intensity images and reconstructed BFI maps from the experiments. A pair of polarizers (LPNIRE050-B and LPNIRE200-B, Thorlabs) were added crossing the source and detection paths to reduce specular reflection directly from the scanning light sources on tissue surface.

For comparisons with LSCI, a hybrid DSCT and LSCI system was assembled (Figure 3.1a). LSCI and DSCT measurements were performed sequentially in one rat at the baseline. For LSCI measurement, an engineering diffuser (ED1-S20-MD, 20° Square Engineered Diffuser, Thorlabs) was manually placed in the source path of DSCT to generate a widefield illumination without the need of point source scanning (Figure 1d). After LSCI measurement, the diffuser was manually removed to facilitate DSCT measurement. Both DSCT and LSCI measurements utilized the same sCMOS camera with an exposure time of 2 ms. The F-number of the detection zoom lens was set as 8 to meet Nyquist sampling rule [52].

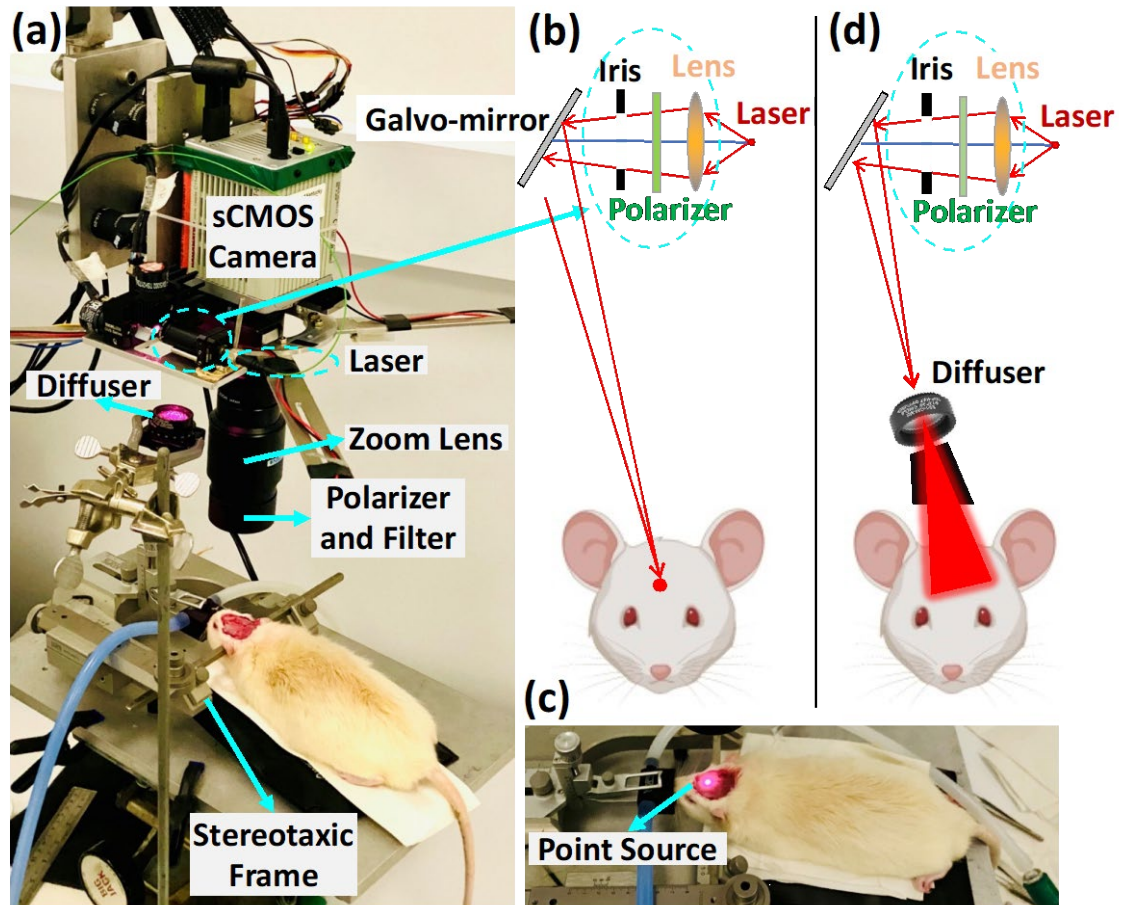


Figure 3.1: A hybrid DSCT and LSCI system for 2-D mapping of CBF in rats.

(a) The rat was anesthetized with 1–2% isoflurane and placed on a heating blanket with its head fixed on a stereotaxic frame. The hybrid instrument was set up overhead for 2-D mapping of CBF distributions. (b) Optical design of DSCT. (c) NIR point source was focused on the exposed skull for DSCT measurements. (d) Optical design of LSCI. Widefield illumination was generated by manually placing a diffuser in the source path for LSCI measurements.

3.2.2 LSCI Method for 2-D Mapping of Superficial CBF

Movement of light scattering particles (i.e., red blood cells) in the measured tissue volume results in spatial fluctuations of laser speckles on the tissue surface, which appear as blurred speckle patterns when recorded by the camera [133]. Using LSCI technique with widefield illumination (Figure 3.1d), the raw intensity image taken from the selected ROI is converted to a spatial speckle contrast image. The spatial speckle contrast is quantified

by calculating the ratio of the standard deviation (σ) of the intensity (I) to its mean intensity ($\langle I \rangle$) in a pixel window of $N_{pixels} \times N_{pixels}$ [52, 53, 134]: $K_s = \sigma / \langle I \rangle = \sqrt{(\langle I^2 \rangle - \langle I \rangle^2)} / \langle I \rangle$. The pixel window size of 3×3 , 5×5 , or 7×7 is usually selected to balance the detection sensitivity and spatial resolution [134]. Larger values of N_{pixels} assess spatial speckle contrasts better in terms of sensitivity at the expense of lower spatial resolutions [52].

Although the exact relationship between K_s and BFI is nonlinear, BFI at each pixel window can be approximated as inverse square of the speckle contrast: $BFI \sim 1/K_s^2$ [133, 135]. Due to its numerical simplicity, this relationship enables fast data processing of K_s values over all pixel windows. Traditionally, two nested *for-loops* are utilized to calculate K_s on each pixel window of $N_{pixels} \times N_{pixels}$. Then, a third *for-loop* iterates the pixel window through all pixels on the ROI to generate a 2-D map of BFI.

We have implemented a fast computation method for analyzing the LSCI and DSCT data, which takes advantage of functions from Image Processing Toolbox™ and Parallel Computing Toolbox™ in MATLAB to dynamically calculate 2-D map of BFI. Instead of using the inefficient *for-loops* to calculate K_s values within the raw image, we applied a MATLAB's built-in 2-D convolution function (*conv2*) from the Image Processing Toolbox™ to implement an implicit multi-threading approach for the fast computation [136, 137]. Figure 3.2a shows the steps of new fast parallel computation method to obtain a speckle contrast image from the raw intensity image, where the kernel matrix was defined as a square matrix of $N_{pixels} \times N_{pixels}$ with all elements equal to $1/N_{pixels}^2$.

Since calculations of multiple speckle contrast images are independent, MATLAB's *parfor* control flow statement in the Parallel Computing Toolbox™ was used to execute

loop iterations in parallel to compute speckle contrast images simultaneously. Specifically in this study, MATLAB's codes were executed on a desktop with Intel(R) Core (TM) i9-10980XE CPU @ 3.00 GHz (18-Core), NVIDIA Quadro RTX 5000 GPU. MATLAB (version: R2021a) automatically utilized all available CPU cores by default, which in this case was 18 workers, when executing parallel commands. As a result, total computation time with the new parallel computation method were reduced dramatically compared to the use of inefficient *for-loops* to calculate K_s values from the raw intensity images sequentially, e.g., reducing from 6.5 hours to 30 seconds to generate 400 flow maps with the total pixels of 2048×2048 in each map.

3.2.3 DSCT Method for 2-D Mapping of CBF at Different Depths

Following our established method [59, 129], raw intensity images were prescreened to ensure that the detected light intensities (counts) were within the linear range of our camera and above the minimal SNR requirement (i.e., $\text{SNR} > 3$). The DSCT method first converted each of raw intensity images taken at different source locations within the ROI into a speckle contrast image based on the fast LSCI analysis utilizing the Image Processing Toolbox™ and Parallel Computing Toolbox™ (Section 3.2.2). Since the penetration depth of DSCT with point source illumination is approximately one half of the S-D distance, the Euclidean distances between each source and detectors (i.e., pixel windows of $N_{pixels} \times N_{pixels}$) were calculated. To extract a K_s map at the depth of d , the pixels/detectors within the S-D distances of $[d1:d2]$ from the source were averaged to improve the SNR (Figure 2b). Here, $d1 = 2d - \Delta d$, $d2 = 2d + \Delta d$, and Δd was selected empirically as 1 mm to balance the SNR and spatial resolution. More generally for each source (S_i), a binary belt shape mask denoted as $M_{S-D}(i)$ was defined such that the pixels

corresponding to the detectors located within S-D distances of [d1:d2] were assigned a value of “1”, while all other pixels are assigned a value of zero. This mask served for identifying the paired detectors for each source to extract corresponding speckle contrast values of $K_s(i)$. These calculations were implemented through all sources and the resulting speckle contrast images were summed to generate one K_s map in the selected ROI (Figure 3.2c). To mitigate the artifacts from the summation of $K_s(i)$ in the overlap regions of masks, the inverse of mask summation was multiplied by $K_s(i)$ summation. Note that DSCT data analyses are based on our fast parallel LSCI analysis (Section 3.2.2), thus also decreasing total computation time dramatically compared to use of inefficient *for-loops* methods.

The DSCT data analysis requires the input of source locations. Following our established method [129], the intensity image captured at each source location was analyzed to precisely determine its location. This method enabled accounting for the potential shift of each source location caused by tissue geometric factor. Briefly, the intensity image taken at each source location was first converted to a binary image. This was done by replacing all intensity values above a globally determined threshold with “1” and setting all other values to “0”. The threshold value was determined by Otsu’s method to minimize the intraclass variance of the thresholded black and white pixels [109]. After thresholding, those pixels with a value of “1” that connected to 8 pixels in the local neighborhoods (so called 8-connected) were found and grouped together. The group with the maximum number of pixels was identified and the rest of the groups were removed from the 2-D binary image. Morphological operators such as opening, closing, and filling were then applied to the binary image for removing thin protrusions and isolated areas to

reduce noise. Finally, the centroid and radius of the point source were determined by estimating the center of the remaining group. This automatic process was repeated for determining all source locations [129].

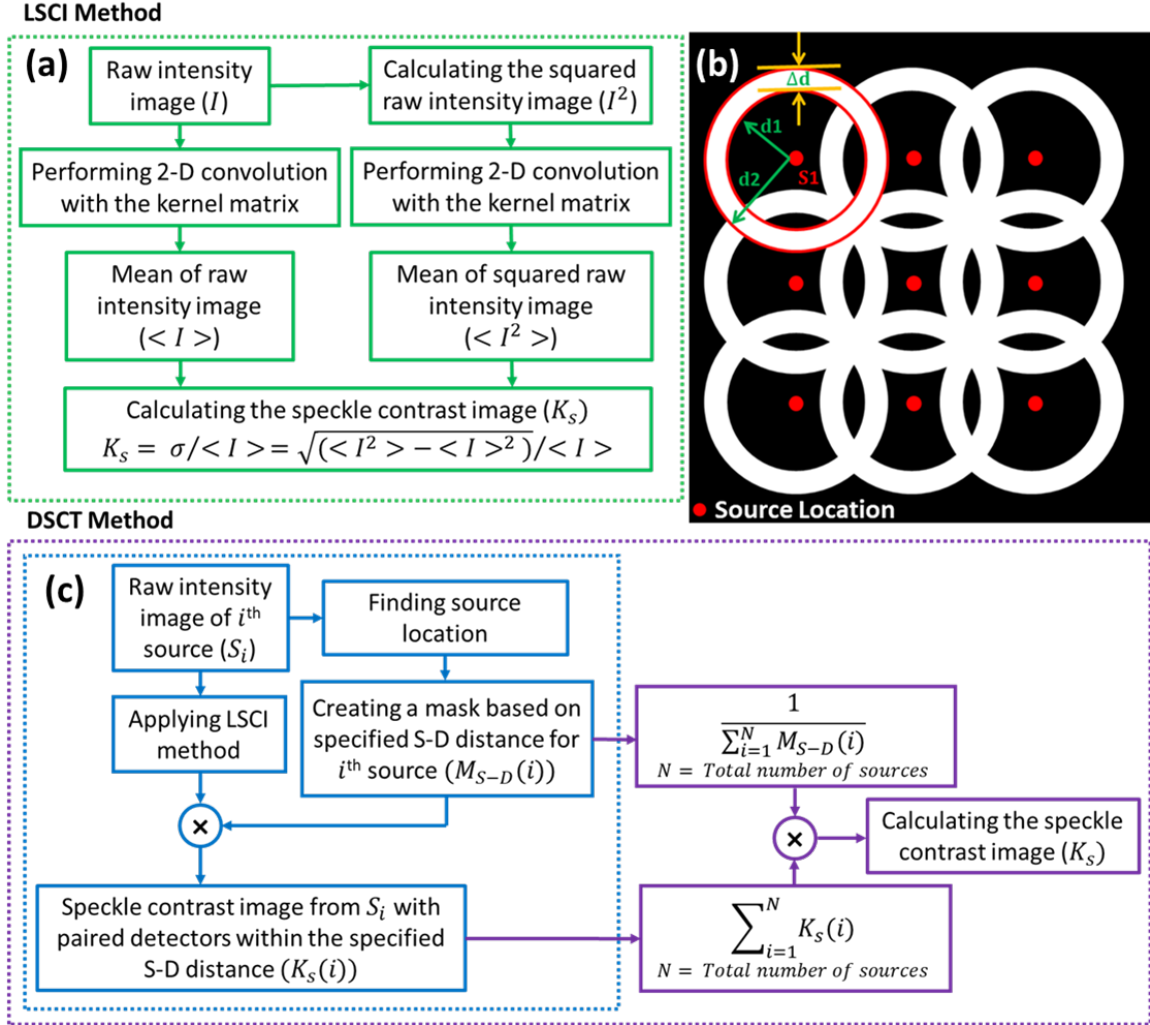


Figure 3.2: A flowchart for data processing in LSCI and DSCT methods.

(a) New fast parallel computation method for LSCI data analysis. The procedures within the green dashed box were executed on each of raw intensity images to calculate K_s values. Parallel Computing Toolbox™ in MATLAB was then used to process multiple raw intensity images simultaneously and generate multiple flow maps. (b) Determination of the S-D mask in DSCT for extracting a K_s map at the depth of d . The detectors within the specified S-D distances of $[d1: d2]$ are selected for each source to calculate K_s values at the depth of d . (c) New fast parallel computation method for DSCT data analysis. The procedures within the blue dashed box were executed on raw intensity image of each source (S_i) to calculate corresponding $K_s(i)$ values. Parallel Computing Toolbox™ in MATLAB was then used to process raw intensity images of all sources simultaneously. The steps depicted in purple boxes were implemented to reduce the artifacts arising from the summation of $K_s(i)$ in the overlap regions of the masks, and ultimately generate one K_s map.

3.2.4 Depth Sensitivity Tests Using New Head-simulating Layered Phantoms

Use of tissue-simulating phantoms with known optical properties is a commonly accepted approach for the validation of new methods and technologies [102, 132, 138]. In this study, head-simulating layered phantoms with known optical/geometry properties were fabricated using 3-D printing techniques for testing the sensitivity of DSCT method in mapping flow distributions at different depths. Two layers of head tissues (skull and brain) were simulated using the solid phantom with zero flow and Intralipid liquid phantom with particle flow, respectively. Figure 3.3a and Figure 3.3b show the 3-D solid phantom (no flow) with empty channels bearing the University of Kentucky (“UK”) logo, fabricated by a 3-D printer (SL1, Prusa). Three solid phantoms with UK logo channels were printed with the top layer thicknesses of 1 mm, 2 mm, and 3 mm, respectively, to mimic skulls with varied thicknesses. The solid phantoms were made of Titanium dioxide (TiO_2), India ink (Black India, MA), and clear resin (eSUN Hard-Tough) [139]. The empty UK logo channels were then filled with liquid phantom solutions composed of Intralipid solution (Fresenius Kabi, Sweden), India ink, and water (Figure 3.3c and Figure 3.3d) [59]. India ink concentration regulates tissue absorption coefficient (μ_a) while TiO_2 and Intralipid concentrations regulate reduced scattering coefficient (μ'_s). Optical properties of both solid and liquid phantoms were set as $\mu_a = 0.03 \text{ cm}^{-1}$ and $\mu'_s = 9 \text{ cm}^{-1}$ to match biological tissue properties [102, 103]. Brownian motion of Intralipid particles inside the UK logo channels provides the particle flow to mimic the motion of red blood cells inside vessels (i.e., blood flow) [59, 140].

To evaluate the impact of sampling density on spatial resolution when using DSCT, 10×10 , 15×15 , 20×20 , and 30×30 source locations were scanned sequentially inside

the ROI of $40 \times 40 \text{ mm}^2$ on the UK logo phantom with the top layer thickness of 1 mm. Then, the UK logo phantoms with the top layer thicknesses of 1 mm, 2 mm, and 3 mm were imaged by the DSCT (with 30×30 source locations) and LSCI sequentially (Figure 3.3b). For both DSCT and LSCI, K_s was computed over a pixel window of 49 pixels (i.e., $N_{pixels} = 7$) to balance the imaging sensitivity and spatial resolution. Five sequential flow maps over time were averaged to improve SNRs. Relative flow values were calculated by normalizing flow indices to their mean within the ROI. Finally, results from the DSCT and LSCI were compared to demonstrate the depth sensitivity of DSCT in contrast to LSCI.

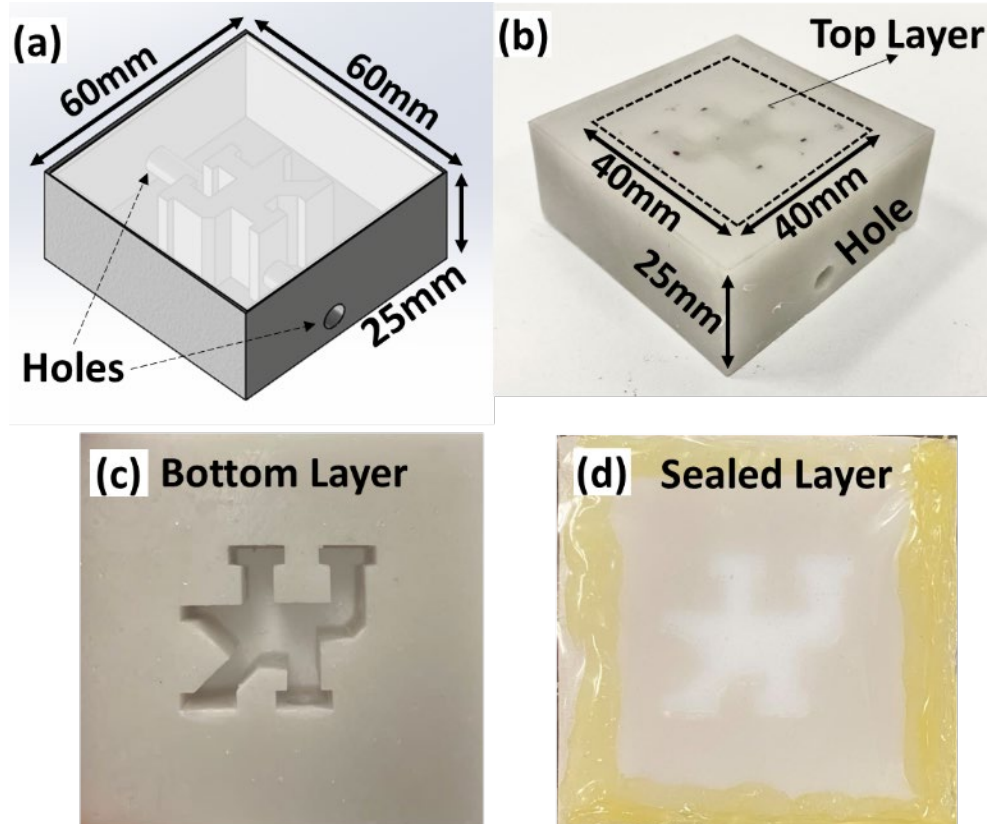


Figure 3.3: New head-simulating layered phantoms with known optical/geometry properties.

(a) 3-D design of solid phantom (no flow) with empty channels bearing the University of Kentucky (“UK”) logo. The holes connected to the UK logo channels were used to fill in liquid phantoms. (b) 3-D printed solid phantom with empty UK logo channels, fabricated by a 3-D printer with the top layer thicknesses of 1 mm. The dashed square indicates the scanning ROI of $40 \times 40 \text{ mm}^2$ on the phantom surface. (c) Bottom view of solid phantom with the empty UK logo channels. (d) The empty UK logo channels were filled with liquid phantom solutions and then sealed with plastic film and hot glue gun.

3.2.5 In-vivo Experiments in Rats

To evaluate the ability of DSCT for continuous monitoring of CBF variations, adult rats with intact skull (scalp was retracted) underwent CO_2 inhalation and transient carotid arterial ligations were imaged. It is well known that CO_2 inhalation leads to global CBF increases while transient arterial ligations lead to regional CBF decreases. All experimental procedures involving animals were approved by the University of Kentucky Institutional Animal Care and Use Committee (IACUC).

Six male adult Sprague-Dawley rats (age: 10-11 months) were imaged by the DSCT. In addition, one animal was imaged by the LSCI for comparisons. For both DSCT and LSCI, K_s was computed over a pixel window of 9 pixels (i.e., $N_{pixels} = 3$) to balance the imaging sensitivity and spatial resolution. The DSCT scanned over 441 source positions (21×21) in the ROI of $20 \times 20 \text{ mm}^2$ on the rat head to balance temporal and spatial resolutions. 2-D maps of CBF at the depths of 1 mm to 3 mm were generated based on the 1 mm skull thickness of adult rats [59]. The relative time-course changes in CBF (rCBF) were calculated by normalizing BFI data to the baseline value before physiological changes.

Unlike the phantom studies where temporal resolution is not critical for imaging constant particle flow contrasts (Section 3.2.4), fast sampling rate is essential in capturing dynamic CBF variations caused by pathophysiological changes. Using conventional 2-D mapping method with 441 sources (21×21), the total sampling time to generate one 2-D map of CBF was 60 seconds. In this study a new method based on a moving window was adapted to improve the sampling rate, where the topographic reconstruction of each CBF map was obtained when one new source position data became available [18, 129]. As a result, the total sampling time was reduced ~ 440 times (i.e., from 60 seconds to 0.136 seconds).

Continuous Imaging of CBF Variations in Rats During CO_2 Inhalation. The rat anesthetized with 1–2% Isoflurane was placed on a heating blanket and its head fixed in a stereotaxic frame. After sterilizing rat's scalp with Betadine and 70% Ethanol, a $20 \times 40 \text{ mm}^2$ piece of scalp was surgically removed. Following the removal, a thin layer of mineral oil was applied to the exposed skull to maintain its moisture and optical properties (Figure

3.1). The noncontact DSCT probe was set above the rat head for continuous mapping of relative changes in CBF (rCBF) before (5 minutes), during (5 minutes), and after (5 minutes) inhalation of 92%O₂/8%CO₂. For CO₂ inhalation, the mixed gas of 92%O₂ and 8%CO₂ was administered through a rat nose cone.

Continuous Imaging of CBF Variations in Rats During Transient Arterial Ligations. Following the CO₂ inhalation measurement, the rat underwent transient unilateral and bilateral ligations of common carotid artery (CCA) to create sequential decreases in rCBF at both hemispheres. For CCA ligations, hairs at cervical surgical site were shaved and removed with hair cream and cervical skin was disinfected with Betadine followed by 70% Ethanol. A midline incision was performed to expose and isolate both the left and right CCAs. A 6-0 braided nylon suture was placed around each CCA with a loose knot. After a baseline measurement for 5 minutes, the right suture was tightened to ligate right CCA for 5 minutes. The left CCA was then also ligated to induce bilateral occlusion of CCAs for another ~2 minutes. Following the release of the left CCA ligation, another 5 minutes of DSCT measurements were performed to record rCBF recovery by releasing right CCA ligation as well. After restoration of rCBF from the transient global ischemia, the rat was euthanized after ~5 minutes inhalation of 100%CO₂. One rat (Rat #1) was excluded from data analysis because of the surgical complication.

3.2.6 Statistical analysis

SPSS software (version 29) was used for statistical analysis in animal studies. The Kolmogorov–Smirnov test was performed to assess the normality of rCBF distributions. Also, repeated measures analysis of variance (ANOVA) following with Post hoc test (pairwise multiple comparisons) were used to evaluate differences in rCBF variations

between the different phases of stimuli (CO₂ inhalations and transient arterial occlusions). A p-value < 0.05 is considered significant for all statistical analysis.

3.3 Results

3.3.1 DSCT Performance Depends on Sampling Density

Figure 3.4 demonstrates the impact of sampling density on spatial resolution when using DSCT to image the UK logo phantom with the top layer thickness of 1 mm. Increasing scanning source numbers improved spatial resolution at the costs of prolonged data acquisition time, increased number of images for processing, and increased computation and storage demands (Table 3.1).

Table 3.1: Impact of sampling density on DSCT performance

Number of sources	Total number of raw intensity images to generate one flow map	Data acquisition time	Data size	Computation time for one depth
10 × 10	100	15 sec	800 MB	12 sec
15 × 15	225	34 sec	1.75 GB	20 sec
20 × 20	400	60 sec	3.12 GB	30 sec
30 × 30	900	132 sec	7.04 GB	85 sec

More specifically, the maximum data acquisition time for obtaining one raw intensity image at one source position was ~150 ms, including 2 ms for exposure, 33 ms for capturing one image by the camera, and 115 ms for saving data to the hard drive.

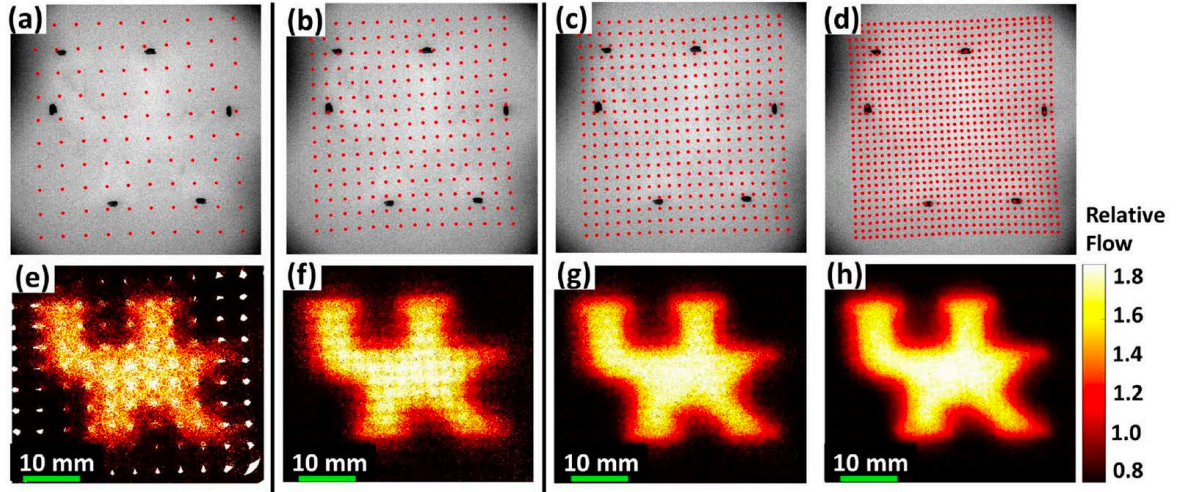


Figure 3.4: Effect of sampling density on spatial resolution of DSCT.

(a)-(d): Numbers of source locations on the UK logo phantom with a top layer thickness of 1 mm: 100 (10×10), 225 (15×15), 400 (20×20), and 900 (30×30). (e)-(h): Resulting 2-D flow maps at the depth of 2 mm with the source numbers of 100, 225, 400, and 900, respectively. Five sequential flow maps were averaged to improve the SNR.

3.3.2 DSCT Enables 2-D Mapping of Phantom Flow Contrasts with Depth Sensitivity

Figure 3.5 shows results using the DSCT and LSCI to image UK logo phantoms with top layer thicknesses of 1 mm, 2 mm, and 3 mm, respectively. For DSCT measurements, 30×30 source locations were scanned over the selected ROI of 40×40 mm² on the phantoms. Higher flow contrasts were observed at deeper depths with larger S-D separations, indicating the depth sensitivity of DSCT method. SNRs decreased with the increases of imaging depth and top layer thickness (i.e., from 1 to 3 mm). These results are expected as the deeper penetration and thicker top layer resulted in fewer diffused photons being detected, thus leading to lower SNRs. By contrast, SNRs and spatial resolutions of superficial LSCI measurements were much worse than those of DSCT measurements, especially on the phantoms with thicker top layers.

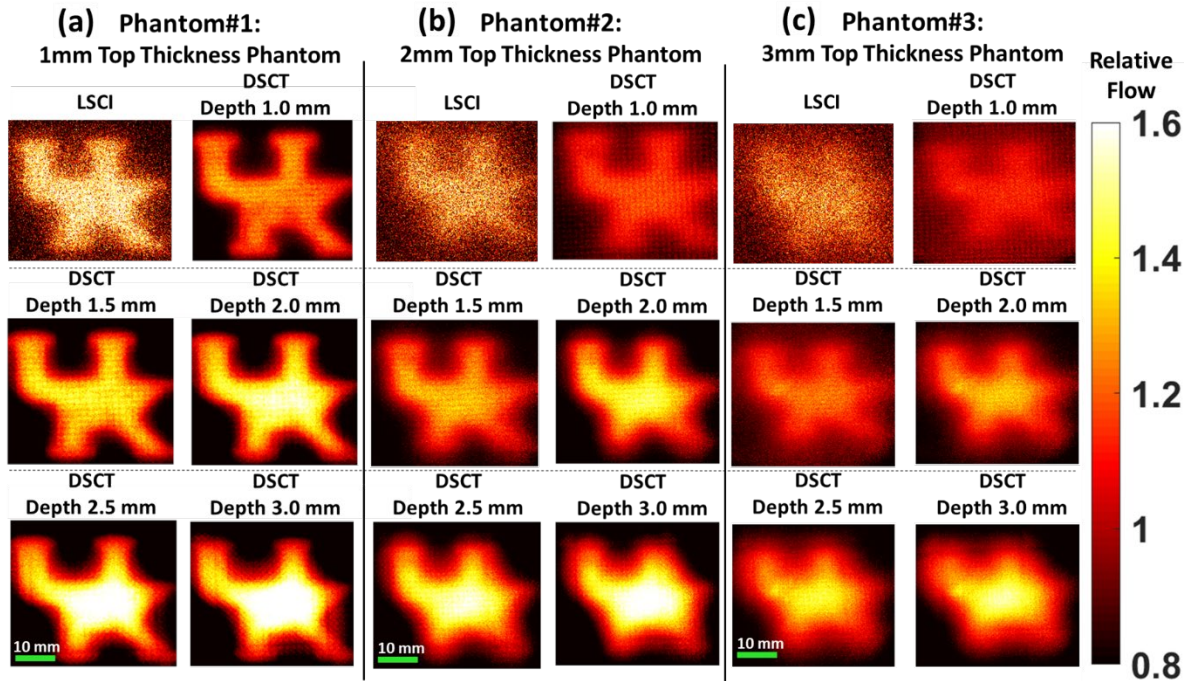


Figure 3.5: DSCT and LSCI measurement results for UK logo phantoms.

(a)-(c): Resulting 2-D maps of Intralipid particle flow contrasts on three phantoms with the top layer thicknesses of 1 mm, 2 mm, and 3 mm, respectively. Flow indices were normalized to their mean values to generate relative flow maps for comparisons.

3.3.3 DSCT Enables 2-D Mapping of rCBF at Different Depths in Rats

Figure 3.6a and Figure 3.6b show white light images of a rat head (scalp was removed) and 441 source positions (21×21) on the rat skull for DSCT measurements. Figure 3.6c shows rCBF map of a representative rat (Rat #4), imaged by the LSCI. Figure 3.6d-3.6h displays rCBF maps of Rat #4 at depths varying from 1 mm to 3 mm, imaged by the DSCT. As observed in phantom measurements (Section 3.3.2), DSCT enables 2-D mapping of rCBF distributions at various depths, with higher spatial resolutions and SNRs than LSCI.

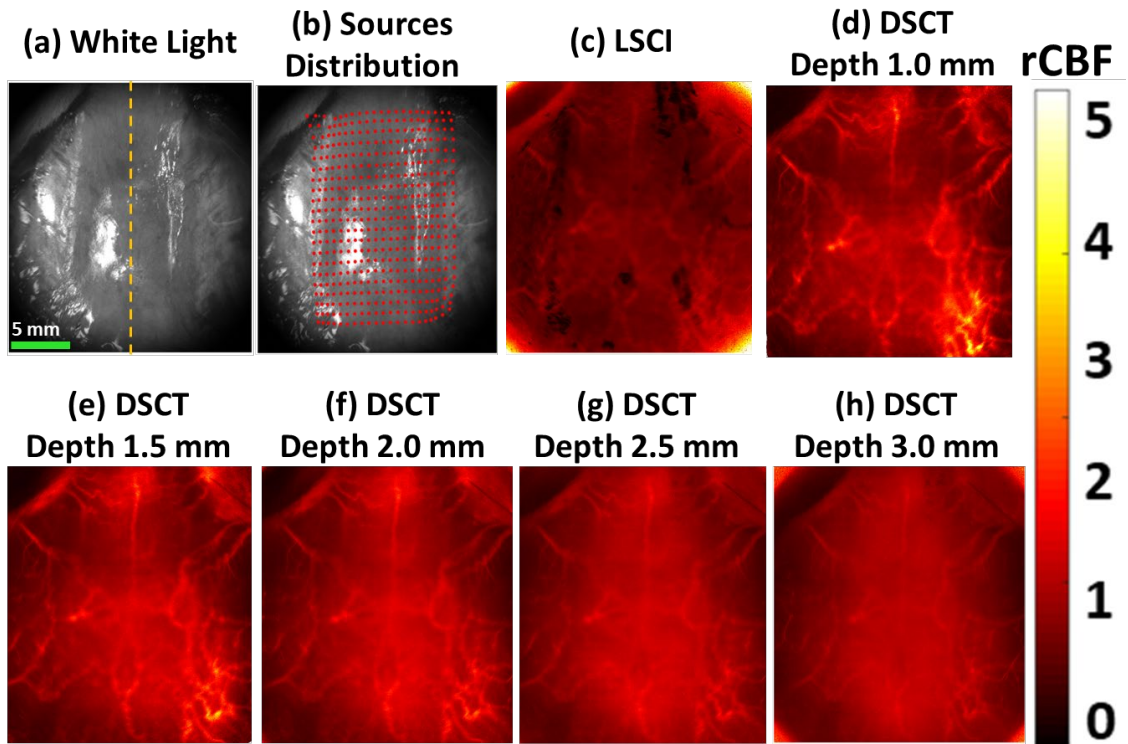


Figure 3.6: 2-D mapping of rCBF distributions with LSCI and DSCT.

(a) A white light image of a rat head with nose up (Rat #4, scalp was retracted). The yellow dotted line indicates the central line that separates the left and right hemispheres. (b) Sources distribution (red dots) on the ROI of 20×20 mm². (c) 2-D map of rCBF, imaged by LSCI. (d) to (h) 2-D maps of rCBF at different depths from 1.5 mm to 3.0 mm, imaged by DSCT.

3.3.4 DSCT Captures Dynamic rCBF Responses During CO₂ Inhalations in Rats

Figure 3.7a shows typical blood flow maps in a representative rat (Rat #2) at the depth of 3.0 mm before, during, and after 8%CO₂ inhalation, measured by the DSCT with 441 source positions (21×21). Figure 3.7b shows time-course changes in rCBF in one rat (Rat #2), calculated by the moving window method and normalizing BFI data to their baseline values (assigning as “100%”) before CO₂ inhalation. Figure 3.7c compares the results of time-course rCBF changes between the conventional reconstruction (red curve) and moving window (blue curve) methods. As expected, both methods generated similar trends in rCBF, although the sampling rate of moving window method was much higher

than the standard reconstruction method. Figure 3.7d compares time-course changes in rCBF at different depths ranging from 1.0 mm to 3.0 mm. As expected, rCBF changes in deeper brain tissues (depth ≥ 2.0 mm) were higher than those in the skull (depth ≤ 1.5 mm). Figure 3.7e shows average time-course changes in rCBF (moving window method) over 6 rats. Table 3.2 summarizes average changes in rCBF during different phases of CO₂ inhalation. The 8%CO₂ led to a significant increase in rCBF at the endpoint of inhalation compared to the baseline (mean \pm standard error: 117% \pm 5%), which agrees with previously reported changes in rCBF [59].

P-values from the Kolmogorov-Smirnov tests were less than 0.05, indicating that the assumption of normality for rCBF distributions was met. Repeated measures ANOVA found an overall significance difference (F = 6.984, p-values = 0.013) in comparing changes in rCBF between different phases of 8%CO₂ inhalation. Table 3.3 shows significance levels (p-values) for comparing changes in rCBF between different phases of 8%CO₂ inhalation using pairwise multiple comparisons. The 8%CO₂ led to a significant increase in rCBF at the endpoint of inhalation compared to the baseline (pairwise multiple comparisons: p-value = 0.024). There was also a significant difference (pairwise multiple comparisons: p-value = 0.046) between the 8%CO₂ inhalation and the endpoint of recovery phase.

Table 3.2: Average rCBF variations (mean \pm standard error) from their baselines during CO₂ inhalation over 6 rats (moving window method)

	Baseline	8% CO ₂ inhalation	Recovery
Brain Region	100% \pm 0.2%	117% \pm 5%	107% \pm 8.5%

Table 3.3: Pairwise multiple comparisons to assess differences in rCBF variations between different phases of CO₂ inhalation

	p-value
--	---------

Baseline	8%CO ₂ Inhalation	0.024*
	Recovery	0.733
8% CO ₂ Inhalation	Baseline	0.024*
	Recovery	0.046*
Recovery	Baseline	0.733
	8% CO ₂ Inhalation	0.046*

*The mean difference is significant at the 0.05 level.

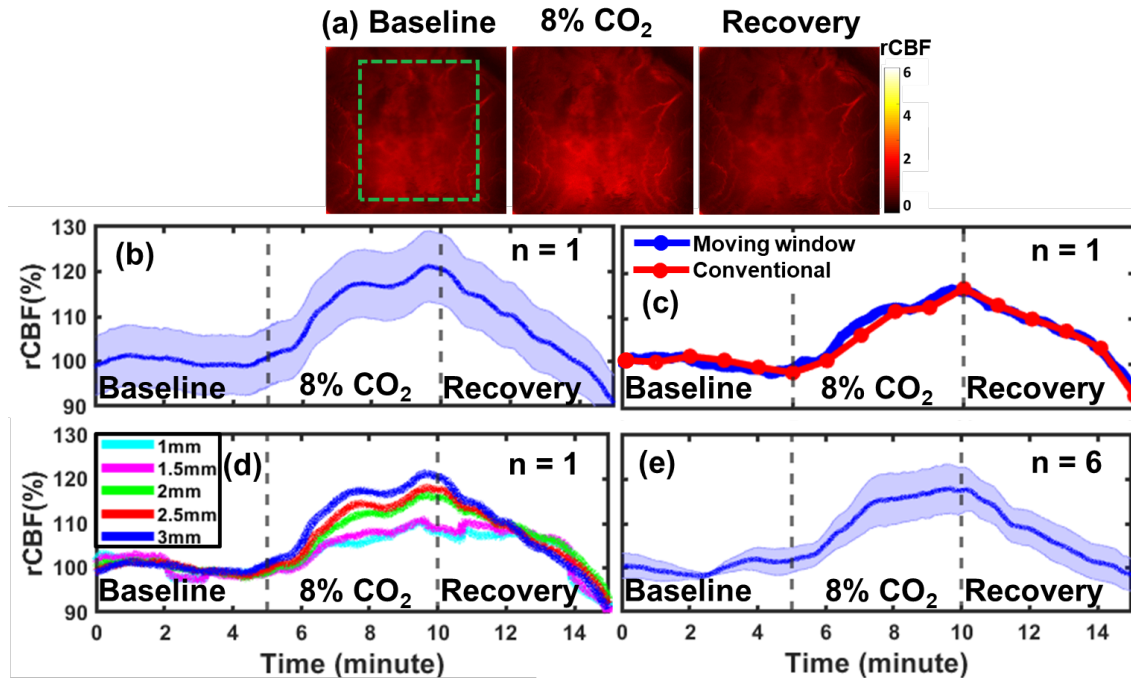


Figure 3.7: DSCT measurements of rCBF responses to CO₂ inhalation in rats.

(a) 2-D maps of rCBF at the depth of 3 mm before, during, and after 8%CO₂ inhalation in an illustrative rat (Rat #2). The dashed green box indicates the selected brain region for data analysis. (b) Time-course changes in rCBF, averaged over the brain region (dashed green box) and reported as mean value \pm standard deviation (Rat #2). The shaded area represents standard deviations. (c) Comparison of time-course changes in rCBF (mean values) between the conventional reconstruction (red curve) and moving window (blue curve) methods (Rat #2). (d) Comparison of time-course changes in rCBF (mean values) at different depths ranging from 1.0 mm to 3.0 mm (Rat #2, moving window method). (e) Average time-course rCBF changes (moving window method) over 6 rats (mean value \pm standard error). The shaded area represents standard errors.

3.3.5 DSCT Captures Dynamic rCBF Responses to Transient Arterial Ischemia and Ischemia and Hypoxia in Rats

Figure 3.8a shows typical blood flow maps in a representative rat (Rat #3) at the depth of 3.0 mm before, during, and after sequential CCA ligations, measured by the DSCT with 441 source positions (21×21). Figure 3.8b shows time-course changes in rCBF at the right and left hemispheres of one rat (Rat #3), which were calculated by the moving window method and normalizing BFI data to the baseline values prior to CCA ligations. Figure 3.8c shows average time-course changes in rCBF over 5 rats. Table 3.4 summarizes average changes in rCBF during different phases of CCA ligations. These results agree with our previous study in adult rats utilizing scDCT with 3-D reconstruction [59].

Table 3.4: Average rCBF variations (mean \pm standard error) from their baselines during unilateral and bilateral CCA ligations over 5 rats

	Right Ligation	Bilateral Ligation	Release Left Ligation	Release Right Ligation (Recovery)
Right Hemisphere (RH)	67% \pm 9%	41% \pm 10%	63% \pm 6%	68% \pm 6%
Left Hemisphere (LH)	78% \pm 9%	37% \pm 9%	72% \pm 4%	80% \pm 4%

Repeated measures ANOVA found a significance differences ($F = 14.619$ (RH)/14.561 (LH), p -values = 0.006) in comparing changes in rCBF between different phases of CCA ligations. Table 3.5 shows significance levels (p -values) for comparing changes in rCBF between different phases of CCA ligations using pairwise multiple comparisons. As expected, the sequential right and left CCA ligations as well as subsequent releasing resulted in significant alterations in rCBF in both hemispheres compared to their baselines (pairwise multiple comparisons: p -value < 0.05). Particularly, the bilateral ligation led to

significant reductions in rCBF in both hemispheres, compared to all other phases of transient CCA ligations (pair-wise multiple comparisons: p-value < 0.05).

Table 3.5: Pairwise multiple comparisons to assess differences in rCBF variations between different phases of ligation in right hemisphere and left hemisphere

		Right Hemisphere (RH) p-value	Left Hemisphere (LH) p-value
Baseline	Right Ligation	0.003*	0.029*
	Bilateral Ligation	<0.001*	<0.001*
	Release Left Ligation	<0.001*	<0.001*
	Release Right Ligation (Recovery)	<0.001*	0.005*
Right Ligation	Baseline	0.003*	0.029*
	Bilateral Ligation	0.005*	<0.001*
	Release Left Ligation	0.482	0.291
	Release Right Ligation (Recovery)	0.925	0.780
Bilateral Ligation	Baseline	<0.001*	<0.001*
	Right Ligation	0.005*	<0.001*
	Release Left Ligation	0.035*	0.003*
	Release Right Ligation (Recovery)	0.028*	0.002*
Release Left Ligation	Baseline	<0.001*	<0.001*
	Right Ligation	0.482	0.291
	Bilateral Ligation	0.035*	0.003*
	Release Right Ligation (Recovery)	0.060	0.005*
Release Right Ligation (Recovery)	Baseline	<0.001*	0.005*
	Right Ligation	0.925	0.780
	Bilateral Ligation	0.028*	0.002*
	Release Left Ligation	0.060	0.005*

*The mean difference is significant at the 0.05 level.

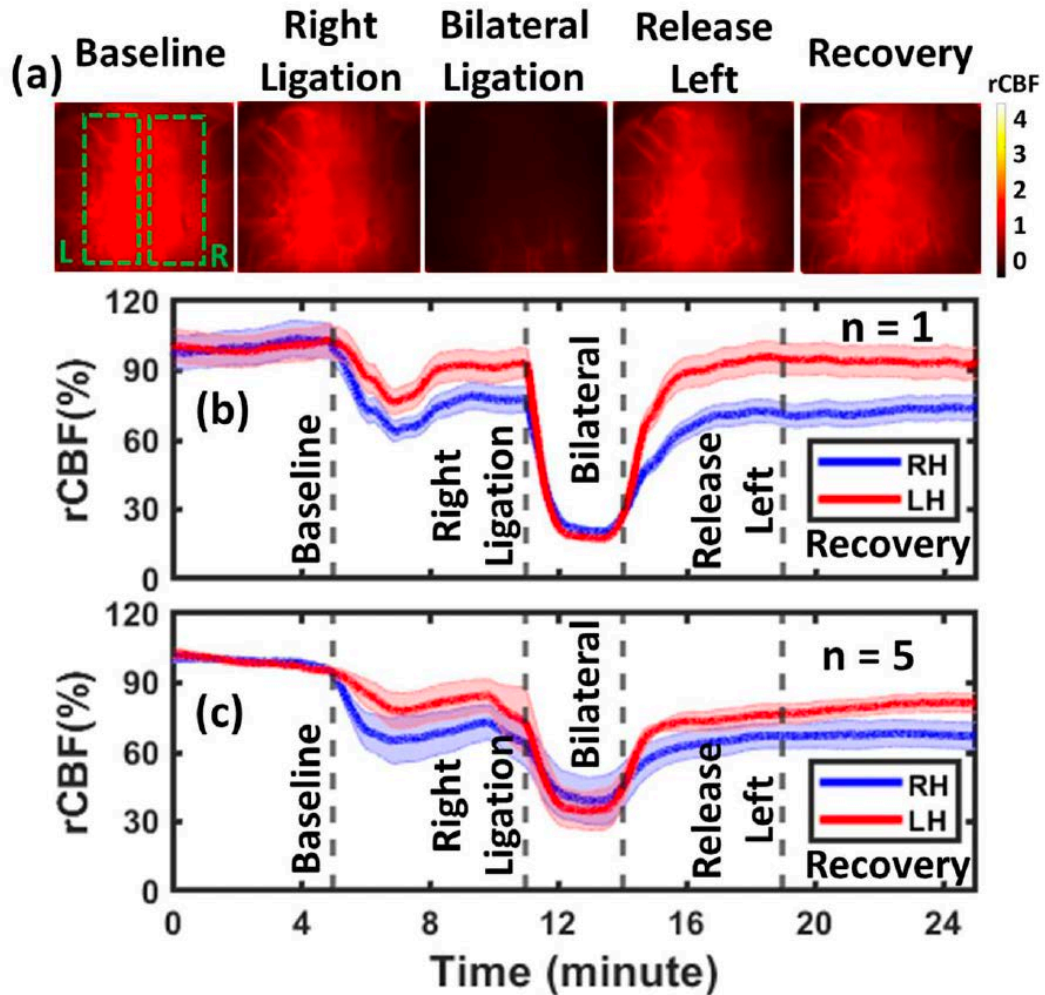


Figure 3.8: DSCT measurements of rCBF responses to sequential unilateral and bilateral CCA ligations in rats.

(a) 2-D maps of rCBF at the depth of 3 mm before, during, and after unilateral and bilateral CCA ligations in an illustrative rat (Rat #3). The dashed green boxes indicate selected brain regions at right hemisphere (RH) and left hemisphere (LH) for data analyses. (b) Time-course changes in rCBF (moving window method), averaged over the brain regions (dashed green boxes) and reported as mean value \pm standard deviation (Rat #3). The shaded area represents standard deviations. (c) Average time-course rCBF changes over 5 rats (mean value \pm standard error). The shaded area represents standard errors.

Figure 3.9a shows typical blood flow maps in a representative rat (Rat #4) at the depth of 3.0 mm before and during 100%CO₂ euthanasia, measured by the DSCT with 441 source positions (21 \times 21). Figure 9b shows time-course changes in rCBF, which were calculated by the moving window method and normalizing BFI data to the baseline values

prior to asphyxia. Figure 3.9c shows average time-course changes in rCBF over 5 rats. At the end, rCBF values were close to “zero”, meeting the physiological expectation.

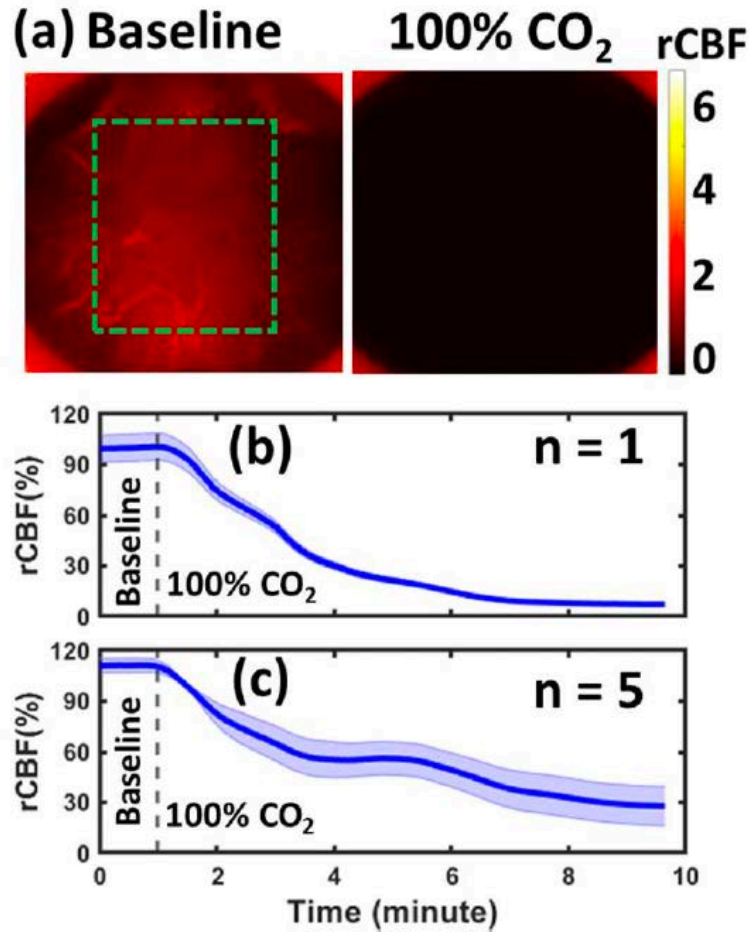


Figure 3.9: DSCT measurements of rCBF variations during asphyxia in rats.

(a) 2-D maps of rCBF at the depth of 3 mm before and at the end of asphyxia challenge in an illustrative rat (Rat #4). The dashed green box indicates the selected brain region for data analysis. (b) Time-course changes in rCBF, averaged over the brain region (dashed green box) and reported as mean value \pm standard deviation. The shaded area represents standard deviations. (c) Average time-course rCBF changes over 5 rats (mean value \pm standard error). The shaded area represents standard errors.

(b)

3.4 Discussion and Conclusions

Assessment of cerebral hemodynamics is crucial for diagnosis and management of cerebral vascular diseases. Recent development of an innovative noncontact scDCT in our laboratory provides a low-cost and portable tool for 3-D imaging of CBF distributions with adjustable FOV and S-D configuration [55, 57, 59, 60]. The spatial resolution of scDCT depends on the numbers of scanning coherence sources and detectors/pixels on the sCMOS camera. However, higher numbers of sources and detectors result in longer computational time required for 3-D reconstruction and lower temporal resolution. To reduce the computation time, we present a new DSCT method with parallel computation for analyzing scDCT data to achieve fast and high-density 2-D mapping of flow distributions at different depths without the need for complex and time-consuming 3-D reconstruction (Figure 3.1).

Specifically, DSCT takes advantages of Image Processing Toolbox™ and Parallel Computing Toolbox™ functions in MATLAB to rapidly generate a 2-D map of CBF (Figure 3.2). To achieve fast calculation of K_s values from raw intensity images, MATLAB's built-in 2-D convolution function was used from the Image Processing Toolbox™. Since raw intensity images obtained at different source positions are independent, multiple 2-D speckle contrast images at different depths (by selecting different S-D separations) are computed and generated simultaneously by executing parallel loop iterations using MATLAB's Parallel Computing Toolbox™. The use of parallel computing with high performance CPUs reduced the processing time significantly in contrast to the inefficient *for-loops* method. For instance, the time required to generate 400 flow maps (each with total pixels of 2048×2048) decreased dramatically from 6.5 hours to 30 seconds.

To tackle low temporal resolution during high density scanning for capturing dynamic rCBF variations, a moving window method was employed to increase the temporal resolution of DSCT [18, 129], where a new 2-D CBF map was produced as soon as the raw image from one new source position data became available. For example, the moving window method with 441 sources (21×21) updated the data at a new source position every 0.136 seconds. As a result, the sampling rate of the moving window method (7.35 Hz) was ~ 440 times higher than the conventional reconstruction method (0.017 Hz). It should be noted that the moving window method increased the temporal resolution significantly at the expense of only utilizing data from one updated source location to generate a new image. Nevertheless, we were able to measure rapid changes in rCBF during CO₂ and CCA ligation tests. It is possible to further increase the sampling rate by optimizing the number of sources and selecting high-quality cameras with faster frame rates. Also, our DSCT with a fast and high-density sampling holds the potential for use to map brain functional connectivity [90], which is a subject of our future study.

In order to evaluate the effect of sampling density on spatial resolution and depth sensitivity of DSCT method for 2-D flow mapping, new head-simulating layered phantoms with UK logo were fabricated by a 3-D printing technique (Figure 3.3). The phantoms were printed with a top solid layer to mimic the skull (no flow) and the UK logo filled by a liquid phantom solution (with Intralipid particle flow). Higher sampling density improves spatial resolution at the expense of longer data acquisition time (Figure 3.4 and Table 3.1). Therefore, it is necessary to balance the spatial and temporal resolutions for specific applications. Results from sequential DSCT and LSCI measurements demonstrate that DSCT enables 2-D mapping of particle flow at different depths through the top layer

(“skull”) with varied thicknesses of 1-3 mm (Figure 3.5). We note that relative flow maps were generated by normalizing the measured flow indices to their mean values within the ROI, obtained from both solid and liquid phantoms. This normalization somewhat reduces the flow contrast between the solid and liquid phantoms, leading to an underestimation of flow contrasts. By contrast, LSCI can barely map the UK logo phantoms with top layer thickness of ≥ 1 mm.

Based on phantom test results, we optimized DSCT’s setup for *in-vivo* animal experiments. We tested the ability of DSCT for continuous monitoring of temporal and spatial variations in rCBF by imaging global rCBF increases during CO₂ inhalations and regional rCBF decreases during CCA ligations in adult rats. Approximately three minutes after 8%CO₂ inhalation, rCBF increased globally and significantly: $117\% \pm 5\%$ of its baseline (Figure 3.7, Table 3.2, and Table S1). These results are consistent with our previous study in adult rats utilizing the scDCT with 3-D reconstruction ($119\% \pm 8\%$ during 10% CO₂ inhalation) [59]. Bilateral CCA ligations resulted in significant reductions in rCBF: $41\% \pm 10\%$ and $37\% \pm 9\%$ of their baselines in the right and left hemispheres, respectively (Figure 3.8c, Table 3.3, and Table S2). rCBF variations during bilateral CCA ligations agree with our previous study in adult rats utilizing scDCT with 3-D reconstruction ($32\% \pm 11\%$ and $34\% \pm 10\%$) [59]. These results suggest that both DSCT and scDCT enable the detection of global and regional rCBF changes in deep brains. However, DSCT achieves fast and high-density 2-D mapping of CBF distributions at different depths without the need of complex and time-consuming 3-D reconstruction in scDCT.

Real-time or near real-time mapping and reporting of CBF by the DSCT offer a range of benefits. Researchers can conduct experiments with faster turnaround times, thus enabling iterative testing and optimization, which is crucial for refining the experimental setup and methodology. Real-time is particularly beneficial when immediate feedback is needed for making the decision, such as during surgical procedure or medical intervention. Efficient data analysis capability is essential for reporting rapid physiological responses or transient events with a high sampling rate and large data size. While the current study focuses on testing DSCT in animals, the ultimate goal is to translate this technology to clinical settings where real-time monitoring/feedback is essential.

In conclusion, we present a novel depth-sensitive DSCT method for rapid 2-D mapping of blood flow distributions in deep brains. The performance of DSCT was evaluated in head-simulating tissue phantoms and *in-vivo* experiments in adult rats. The results from DSCT agreed with those reported previously using scDCT in adult rats with similar experimental protocols. Since the hardware for data acquisition in the scDCT and DSCT are essentially the same, they share the same advanced features including noncontact hardware, flexible S-D configuration, adjustable ROI/FOV, and a cost-effective instrument. Compared to the scDCT technique with 3-D reconstruction, however, DSCT method with fast sampling rate and parallel computation enables fast and high-density 2-D mapping of blood flow distributions at different depths. With more optimizations, we expect to ultimately offer a noninvasive, noncontact, fast, high resolution, portable, and inexpensive brain imager for basic neuroscience research in small animal models and for translational studies in human neonates.

CHAPTER 4. A WEARABLE FLUORESCENCE IMAGING DEVICE FOR INTRAOPERATIVE IDENTIFICATION OF HUMAN BRAIN TUMORS

This chapter is presented based on a submitted manuscript: **Mohtasebi M**, Huang C, Zhao M, Mazdeyasna S, Liu X, Haratbar SR, Fathi F, Sun J, Pittman T.A., Yu G. A Wearable Fluorescence Imaging Device for Intraoperative Identification of Human Brain Tumors. IEEE Journal of Translational Engineering in Health and Medicine. 2023 July 25.

Abstract

Significance: Malignant glioma (MG) is the most common type of primary malignant brain tumors. Surgical resection of MG remains the cornerstone of therapy and the extent of resection correlates with patient survival. A limiting factor for resection, however, is the difficulty in differentiating the tumor from normal tissue during surgery. Fluorescence imaging is an emerging technique for real-time intraoperative visualization of MGs and their boundaries. However, most clinical grade neurosurgical operative microscopes with fluorescence imaging ability are hampered by low adoption rates due to high cost, limited portability, limited operation flexibility, and lack of skilled professionals with technical knowledge. To overcome the limitations, we innovatively integrated miniaturized light sources, flippable filters, and a recording camera to the surgical eye loupes to generate a wearable fluorescence eye loupe (*FLoupe*) device for intraoperative imaging of fluorescent MGs.

Approach: Two *FLoupe* prototypes were constructed for imaging of Fluorescein and 5-aminolevulinic acid (5-ALA), respectively. The wearable *FLoupe* devices were tested on tumor-simulating phantoms and patients with MGs.

Results: Comparable results were observed against the standard neurosurgical operative microscope (PENTERO® 900) with fluorescence kits.

Conclusions: The affordable and wearable *FLoupe* devices enable visualization of both color and fluorescence images with the same quality as the large and expensive stationary operative microscopes. The wearable *FLoupe* device allows for a greater range of movement, less obstruction, and faster/easier operation. Thus, it reduces surgery time and is more easily adapted to the surgical environment than unwieldy neurosurgical operative microscopes.

4.1 Introduction

There are nearly 700,000 people in the U.S. living with a brain tumor [66]. Malignant gliomas (MGs) constitute 35-45% of primary brain tumors with an incidence of approximately 5 out of 100,000 [67, 68]. MGs are aggressive, highly invasive, and neurologically destructive [69]. Surgical resection remains the cornerstone of therapy to treat MGs and the extent of resection correlates with survival [70-76]. However, gross-total-resection (GTR) rates in conventional surgeries are only 30-55% due to difficulty in recognizing diffuse infiltrative tumor cells at the margin of resection and tissue shift during surgery [77-81].

Conventional tumor resection techniques are largely relying on surgeon's observation of subtle changes associated with tissue distortion by invasive tumors. More recently, neurosurgeons utilize imaging techniques such as magnetic resonance imaging (MRI), computed tomography (CT), and angiogram to identify tumor preoperatively [82]. Some MRI machines specially designed for intraoperative imaging help neurosurgeons navigate delicate structures surrounding the tumor [83]. However, incorporating MRI techniques is expensive and time consuming and significantly interferes with surgical workflow. Moreover, specific types of tumors such as high-grade MGs have ill-defined

tissue boundaries with tendrils extending from the main tissue volume, which are difficult to locate during resection. Prevalence of residual cancerous cells on the surgical margin leads to repeat surgeries and is a significant burden on patients and healthcare systems [70-76].

Fluorescence imaging has emerged as an advanced adjunctive technique, allowing for real-time cancer-specific detection without the concern for brain tissue shift and with limited disruption to surgical workflow [74-81, 84]. Surgeries guided by fluorescence imaging achieve GTR rates of 75-100%, which are significantly higher than the conventional surgeries with GTR rates of 30-55% [77, 78, 85, 86]. Fluorescence light is generated when a fluorophore absorbs the excitation light at the wavelength of its absorption peak, which excites fluorophore electrons to a higher energy level. The fluorophore then releases the extra energy as light (photons) while its energy level returns to the ground state. Therefore, the emitted fluorescence light has a longer wavelength compared to the excitation radiation [141].

Various fluorescent agents are increasingly being tested to distinguish tumors from normal parenchyma, thus improving surgical resection while sparing healthy tissue. Fluorescein and 5-aminolevulinic acid (5-ALA) are the two most frequently used fluorescent tracers for guiding MG surgeries [84, 142]. Fluorescein accumulates primarily in the extracellular space of MGs for hours while minimizing its leakage into the normal brain tissue. The efficient clearance of Fluorescein from the body ensures its safe use in medical applications [81]. Fluorescein dye has a peak excitation from 465 to 490 nm and emission band between 500 and 550 nm [81]. 5-ALA is a precursor molecule that leads to the synthesis of phototoxic protoporphyrin IX (PpIX) in the heme biosynthesis pathway.

When 5-ALA is systemically delivered to the body, it is selectively accumulated within MG cells, which often exhibit higher metabolic activity compared to healthy cells. As a result, the concentration of PpIX increases in cancerous cells. PpIX absorbs blue light from 375 to 440 nm and emits a violet-red fluorescence from 620 to 710 nm [143, 144].

Although 5-ALA is more expensive than Fluorescein, it is the only fluorescent agent so far tested in randomized controlled trials in Europe and results in significant GTR improvement and especially progression-free survival in high-grade MGs [84]. More recently in 2017, 5-ALA was granted approval by the Federal Drug Administration (FDA) as an optical agent for adjunct visualization of malignant tissue in patients with suspected World Health Organization (WHO) III or IV gliomas [145, 146].

Optimization of imaging technologies to enhance fluorescence contrasts have been explored over decades [77]. Current standards for intraoperative visualization of MGs are neurosurgical operative microscopes. Industries have also developed FDA-cleared supplementary fluorescence modules that attach to the standard neurosurgical operative microscopes for fluorescence imaging during surgery [77, 80, 81, 84, 85]. For example, Carl Zeiss Meditec (Oberkochen, Germany) has marketed the PENTERO® 900 microscope with a YELLOW 560™ filter kit for Fluorescein visualization and a BLUE 400™ filter kit for 5-ALA visualization. The PENTERO® 900 with filter kits encompasses Xenon arc lamps (white light) with special excitation filters in the wavelength ranges of 460-500 nm (YELLOW 560™) and 400-410 nm (BLUE 400™) for exciting Fluorescein and 5-ALA contrasts, respectively. On the other hand, integration of emission filters into detection paths customize the emissions in the wavelength ranges of 540-690 nm (YELLOW 560™) and 620-710 nm (BLUE 400™) for both ocular visualization and

monitor display of Fluorescein and 5-ALA fluorescence images, respectively [87]. However, most clinical grade neurosurgical operative microscopes are hampered by low adoption rates due to high cost, limited portability, limited operation flexibility, and lack of skilled professionals with technical knowledge. Currently available neurosurgical fluorescence microscopes are expensive and weigh hundred pounds [81, 85]. Resource poor environments may not have access to neurosurgical fluorescence microscopes. Many neurosurgeons prefer and continue to resect tumors while wearing low-cost surgical eye loupes that allow for easy operation. However, most commercial surgical eye loupes cannot visualize fluorescence due to the lack of excitation and fluorescence filtering systems.

To overcome limitations of currently available imaging modalities, we innovatively integrated miniaturized light sources, flippable filters, and a recording camera to the eye loupes to generate a unique wearable fluorescence eye loupe device, namely “*FLoupe*” (US Patent Application #62/530,613, 2017), for real-time identification of MGs during surgery. Two *FLoupe* prototypes have been constructed for intraoperative imaging of Fluorescein and 5-ALA, respectively. We have experimentally verified the dual-imaging ability of *FLoupe* prototypes against the standard PENTERO® 900 with fluorescence kits in the tumor-simulating fluorescence phantom and patients with MGs. Overall, our low-cost wearable *FLoupe* devices enable visualization of both color and fluorescence images with the same quality as the large and expensive stationary neurosurgical operative microscopes.

4.2 Materials and Methods

Two *FLoupe* prototypes (*FLoupe-1* and *FLoupe-2*) were developed to image Fluorescein and 5-ALA contrasts, respectively. The devices were tested in 11 patients with MGs (one with Fluorescein and 10 with 5-ALA) during surgery at the University of

Kentucky (UK) Hospital. The study has been approved by the UK Institutional Review Board (IRB). Informed consents were obtained from all subjects. Patient demographics, tumor type, and WHO grade were listed in Table 4.1. The WHO grade classifies tumors based primarily on their malignancy, with particular emphasis on most aggressive regions of tumors. Low-grade tumors include WHO grade I (pilocytic astrocytoma) and WHO grade II (diffuse astrocytoma). High-grade tumors include WHO grade III (anaplastic astrocytoma) and grade IV (glioblastoma multiforme - GBM) [147]. Isocitrate dehydrogenase (IDH) wildtype GBM comprise over 90% of glioblastomas [148]. MG resection was performed following the standard protocols under the guidance of PENTERO® 900 with YELLOW 560™ for Fluorescein and PENTERO® 900 with BLUE 400™ for 5-ALA, respectively. The identified MGs were then imaged by the *Floupe* devices for comparisons.

4.2.1 *FLoupe-1* for Imaging of Fluorescein Contrast

We first developed a *FLoupe-1* prototype for imaging Fluorescein contrasts, which piggybacks on a commercial eye-loupe device (EyeZoom™ 5.0X, Orascoptic, Figure 4.1a) and a headlight bracket (Halogen III, BFW). An excitation filter (MF475-35, Thorlabs) was installed in front of the fiber-optic headlight (coupled with a 300W Xenon arc lamp) to generate the narrow-band light (center wavelength = 475 nm; full width at half-maximum (FWHM) = 35) for Fluorescein excitation (Figure 4.1b). A pair emission filters (MF530-43, Thorlabs) was attached to the eye loupes for Fluorescein visualization (center wavelength = 530 nm; bandwidth = 43 nm). A video camera (FL3-FW-20S4C-C, FLIR) equipped with another filter (MF530-43, Thorlabs) was attached to the headlight bracket for fluorescence image recording.

Table 4.1: Patient demographics and tumor characteristics

Contrast Agent	Age	Gender	Histology	Location
Fluorescein	76	Female	GBM, IDH Wildtype, WHO Grade IV	Left parietal lobe
5-ALA	47	Male	GBM, IDH Wildtype, WHO Grade IV	Left parietal
5-ALA	72	Male	GBM, IDH Wildtype, WHO Grade IV	Right temporal
5-ALA	60	Female	GBM, IDH Wildtype, WHO Grade IV	Right frontal
5-ALA	62	Male	GBM, IDH Wildtype, WHO Grade IV	Right posterior temporal with extension into the occipital and parietal
5-ALA	30	Male	Oligodendroglioma, WHO Grade III	Left mid anterior frontal lobe
5-ALA	66	Male	GBM, IDH Wildtype, WHO Grade IV	Right frontal lobe
5-ALA	35	Male	Minute residual GBM, IDH Wildtype, WHO Grade IV	Right frontal lobe
5-ALA	76	Male	GBM, IDH Wildtype, WHO Grade IV	Right temporal lobe
5-ALA	61	Female	GBM, IDH Wildtype, WHO Grade IV	Lateral temporal lobe
5-ALA	56	Male	Gliosarcoma, IDH Wildtype, WHO Grade IV	Right temporal/occipital/parietal lobes

GBM: Glioblastoma Multiforme, IDH: Isocitrate Dehydrogenase, WHO: World Health Organization.

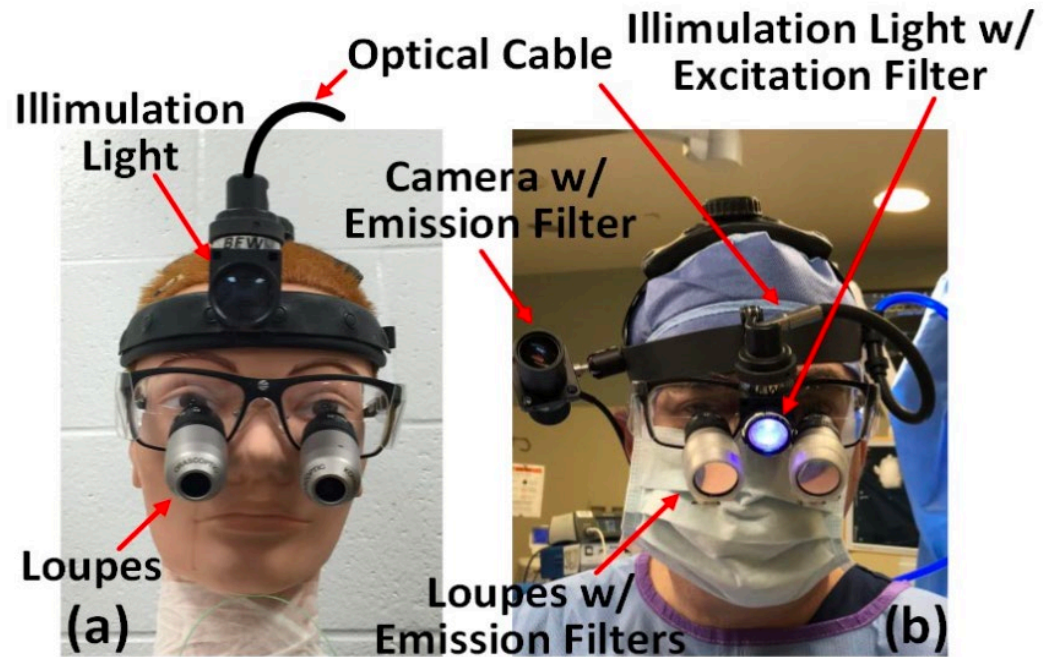


Figure 4.1: Development of *FLoupe-1* prototype.

(a) Conventional wearable eye loupes and fiber-optic headlight bracket for white light imaging. (b) *FLoupe-1* prototype for fluorescence imaging.

We tested this *FLoupe-1* prototype on a tumor-simulating fluorescence phantom. The bulk material used for making the phantom was acetal plastic, which acts as a diffusive tissue. The phantom was fabricated using a 3-D printer (Gigabot® 3.0) and consisted of holes/spaces to test imaging sensitivity and spatial resolution. Experiments were performed by filling the holes with solutions of varying concentrations of Fluorescein (1 to 8 mg/kg) to delineate real tumor tissues with different fluorescence contrasts. The smallest and largest holes were 2 and 10 mm in diameter, respectively, to mimic the different sizes of diffusive tumors.

We also tested this *FLoupe-1* prototype in one patient with MGs. At the induction of anesthesia, patient received intravenous Fluorescein at a dosage of 5 mg/kg body weight [77, 85]. During MG resection, the PENTERO® 900 microscope equipped with a YELLOW 560™ filter were utilized as the standard for intraoperative identification of

MGs to guide resection. The identified MGs (before resection) were then imaged by *Floupe-1* device for comparisons.

4.2.2 *Floupe-2* for Imaging of 5-ALA Contrasts

More recently, the UK Hospital started routinely using the PENTERO® 900 with BLUE 400™ module to image 5-ALA contrasts in GMs for the guidance of tumor resection. To meet this need, we developed the *Floupe-2* prototype for imaging 5-ALA contrasts. *Floupe-2* was developed in collaboration with SurgiTel, a world leading manufactory and supplier for eye loupes, headlights, video cameras, and other medical devices. The standard SurgiTel products include white LED headlights driven by a lithium portable battery pack (~8 hours) and surgical eye loupes with up to 10× magnification Eye Loupes (Figure 4.2a).

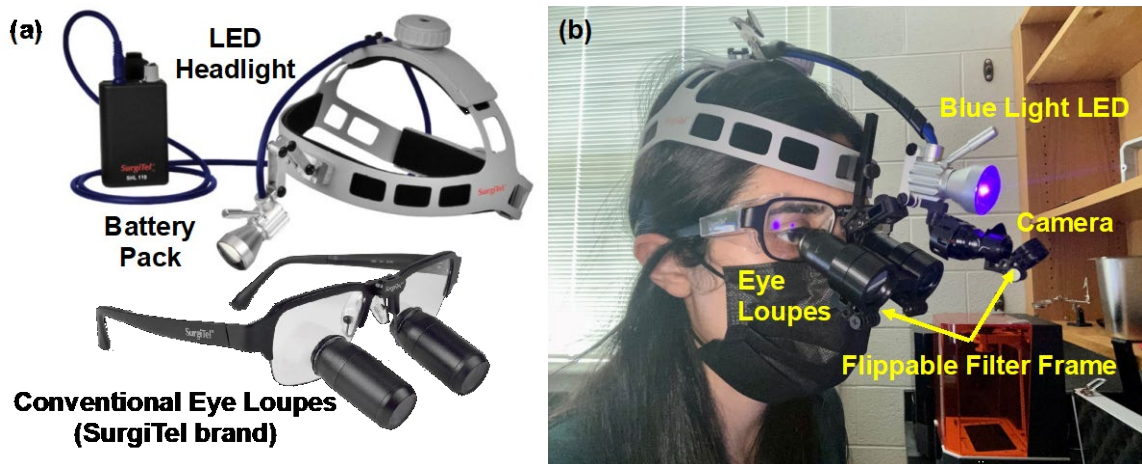


Figure 4.2: Development of *Floupe-2* prototype.

(a) Commercial wearable eye loupes and headlight bracket (SurgiTel brand) for white light imaging. (b) FLoupe-2 prototype for both white light and fluorescence imaging.

To achieve our goal of imaging 5-ALA, the white LED in SurgiTel headlight was replaced with a narrow-band, high-intensity, blue LED (405 ± 5 nm, SST-10-UV, Luminus Devices) for 5-ALA excitation (Figure 4.2b). We adjusted/calibrated the blue

light intensity against the PENTERO® 900 with BLUE 400™ module to ensure the patient safety. A video camera was attached to the headband for real-time recording of the surgical site. We also designed and fabricated a small flippable filter frame by a 3-D printer (SL1, Prusa) and integrated a long-pass optical filter (>550 nm, Diameter 12.5 mm, #15-213, Edmund Optics) in front of the video camera for fluorescence image recording. Another flippable frames were designed and fabricated to hold long-pass filters (>550 nm, Diameter 25 mm, #62-984, Edmund Optics) in front of eye loupes. These unique flippable filter frames attached to the video camera and eye loupes allow for easily changing from fluorescence to color vision/recording and vice versa. The video camera and eye loupes are aligned to the same field-of-view (FOV) at the surgical site. The integrated small video camera in *FLoupe-2* with a dedicated emission filter frame is used for continuous displaying on the Operating Room (OR) monitor. and video recording of fluorescence images at the surgical site (Figure 4.3). This video recording is critical for comparing *FLoupe-2* with the fluorescence surgical microscope (e.g., PENTERO® 900 with fluorescence kits) in real time.

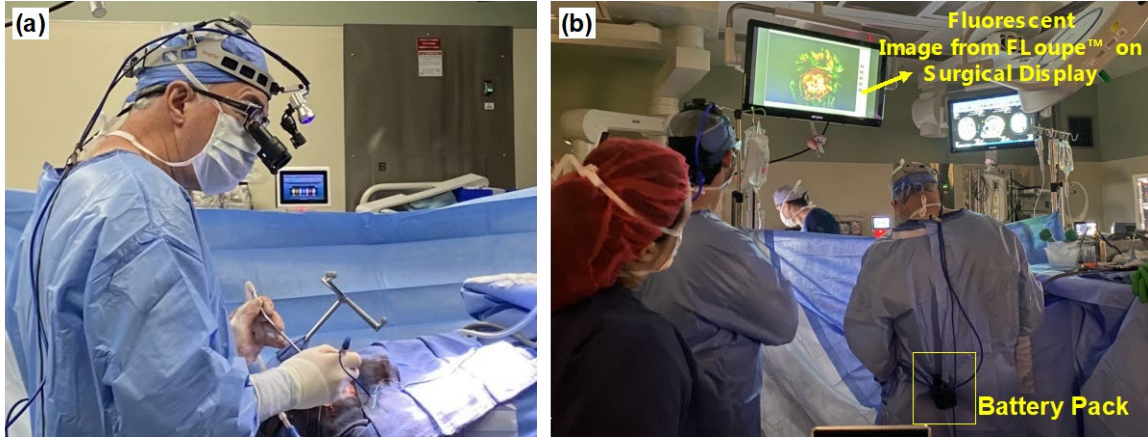


Figure 4.3: Use of *FLoupe-2* for fluorescence imaging of MGs.

(a) The neurosurgeon wears *FLoupe-2* during surgery. (b) Real-time display of MGs on the OR monitor allows the surgical team with immediate feedback and other trainees (e.g., residents) to observe and discuss the surgical operation.

We tested this *FLoupe-2* prototype in 10 patients with MGs and compared results against PENTERO® 900 with BLUE 400™ module. Patients were administered 5-ALA (Gliolan, Medac) at a dosage of 20 mg/kg body weight four hours prior to induction of anesthesia. The PENTERO® 900 microscope equipped with a BLUE 400™ filter were utilized as the standard for the guidance of MG resection.

4.3 Results

Figure 4.4a-4c show the results from tumor-simulating fluorescence phantom measurements using *FLoupe-1*. Fluorescence images of phantom “tumors” were clearly observed by the PENTERO® 900 with YELLOW 560™ (Figure 4.4a) and our *FLoupe-1* (Figure 4.4b). Holes with Fluorescein concentrations as low as 1 mg/kg, and diameters as small as 2 mm were detected by both imaging devices. These lower limits are generally sufficient to identify MGs for resection, given that patients receive 5mg/kg body weight of intravenous Fluorescein [77, 85]. As expected, when using our *FLoupe-1* device without

an emission filter, fluorescent contrasts were hidden by the high-intensity excitation light (Figure 4.4c).

Figure 4.4d-4f show fluorescence images taken from a patient with MG by the commercial PENTERO® 900 with YELLOW 560™ (Figure 4.4d) and our *FLoupe-1* device (Figure 4.4e). Although filter variances across the two devices lead to slight color differences between images, similar fluorescent signals/dots are observed on diffusive tumors.

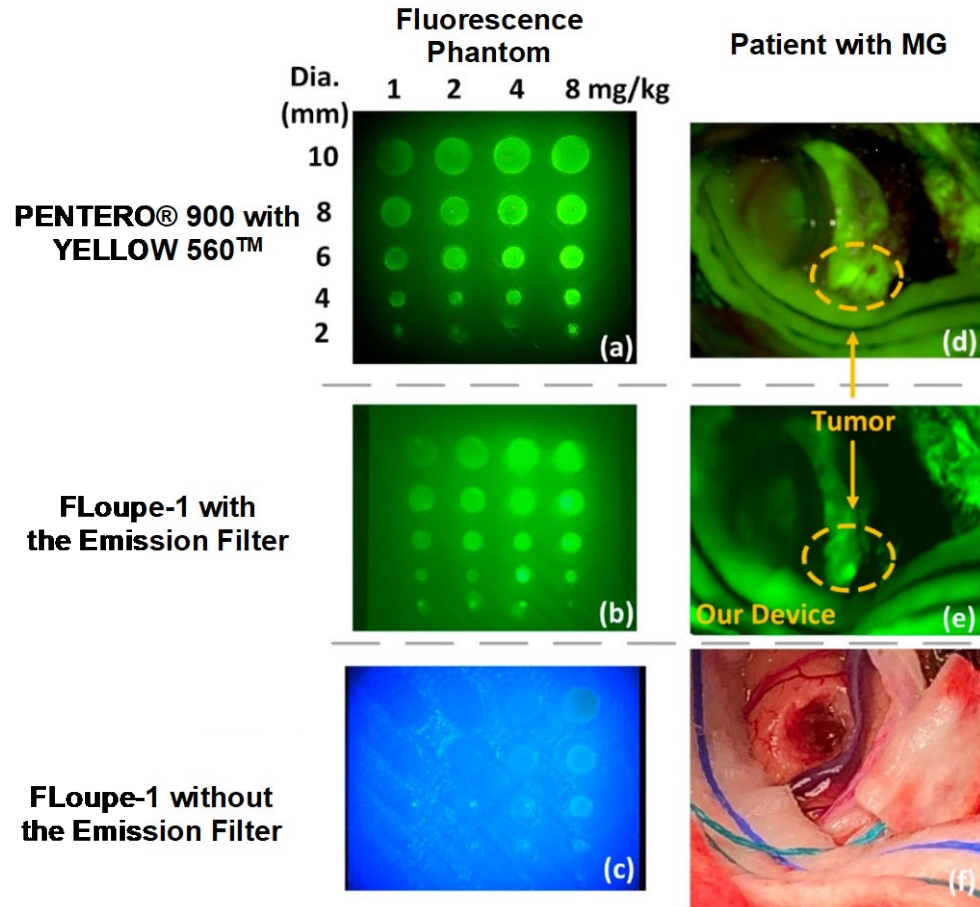


Figure 4.4: Comparison of imaging results in a fluorescence phantom and a patient with MG.

Images were obtained using PENTERO® 900 with YELLOW 560™ (a, d) and FLoupe-1 with the emission filter (b, e) and without the emission filter (c, f), respectively. Note that the color image (f) was obtained using the white light illumination and FLoupe-1 camera without the emission filter.

Figure 4.5 shows the color and fluorescence images from three patients (P1-P3) obtained by the PENTERO® 900 with BLUE 400™ and FLoupe-2, respectively. The two imaging modalities generated consistent results in visualization of fluorescent MGs (see the tumor contours drawn manually based on fluorescence visualization in Figure 4.5b and Figure 4.5c). The fluorescent tumorous tissues appeared more vivid with our FLoupe-2 (Figure 4.5c) as compared to the PENTERO® 900 with BLUE 400™ (Figure 4.5b), which is likely due to the differences in excitation lights and emission filters used in the two

modalities. The PENTERO® 900 with BLUE 400™ uses the Xenon arc lamp with an excitation filter to generate the blue light whereas *FLoupe-2* uses a narrow-band blue LED for 5-ALA fluorescence excitation (see Figure 4.2b). Moreover, the color difference on the fluorescence images (Figure 4.5b and Figure 4.5c) is mainly due to the spectral difference of the emission filters used in the two imaging systems. Similarly, *FLoupe-2* was able to visualize fluorescent tumors in other patients with low or high grade of MG (see Table 4.1).

4.4 Discussion and Conclusions

Fluorescence imaging of cancers during surgery allows real-time cancer-specific detection for guiding tumor removal, usually resulting in significant improvements in patient survival. However, most clinical-grade fluorescence imaging systems are hampered by high costs, limited portability, and lack of operation flexibility. Many surgeons prefer and continue to use wearable surgical eye loupes, which allow for convenient and fast operation, but are not capable of fluorescence visualization. We developed low-cost wearable *FLoupe* devices (US Patent Application #62/530,613, 2017), which are attached to wearable surgical eye loupes to help neurosurgeons easily and accurately identify fluorescent MGs for safe and maximal tumor removal. We have tested two *FLoupe* prototypes for real-time imaging of Fluorescein and 5-ALA contrasts respectively in a small group of patients with MGs. Comparable results were observed against the standard neurosurgical operative microscope (PENTERO® 900) with fluorescence kits.

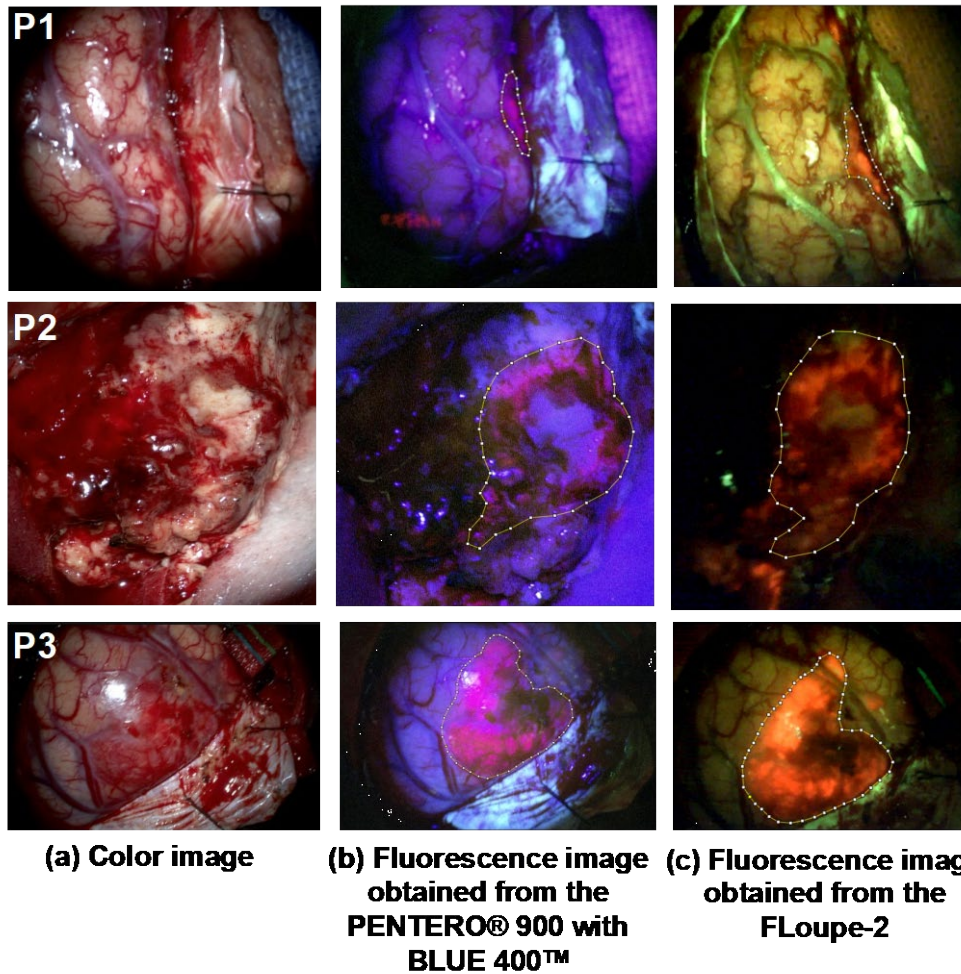


Figure 4.5: Comparison of imaging results from three patients with MGs (P1-P3).

(a) Color images obtained using the white light illumination and PENTERO® 900 camera without the emission filter. (b) Fluorescence images obtained from the PENTERO® 900 with BLUE 400™. (c) Fluorescence images obtained from the FLoupe-2. Note that the tumor contours were drawn manually based on fluorescence visualization.

Our *FLoupe* technology provides unique advancements over other competitors' fluorescence imaging technologies, specifically for the guidance of brain cancer resection. Compared to expensive, large, stationary, neurosurgical operative microscopes (e.g., PENTERO® 900) [81, 85], *FLoupe* devices are affordable and wearable and allow for a greater range of movement, less obstruction, and faster/easier operation. This affordable and wearable device significantly increases the ability of more surgeons to conduct fast and thorough operations, and thus improving patient safety and outcomes. Moreover, this

low-cost allows for procurement of multiple devices, thus alleviating costs for maintenance and downtime for device repair/replacement.

Very recently, Design for Vision reported a fluorescence eye loupe prototype (*ReVeal*) for imaging of 5-ALA contrasts in MGs [149]. Pilot observation studies were performed in a small group of patients to test its usability for fluorescence imaging of high-grade MGs. As mentioned in their study limitations, several key studies are lacking before *ReVeal* is recommended for widespread clinical practice. Also, a comparison sensitivity/specificity histological study needs to be performed to fully assess the potential of *ReVeal* as a replacement for the neurosurgical microscopes. In comparison, *FLoupe* has the following unique features. First, *FLoupe* has designed and fabricated unique flippable filter frames that are attached to the eye loupes and video camera for easily switching from fluorescence to color vision and vice versa. Moreover, the flippable and modular design makes it easy to switch the LEDs and filters on the *FLoupe* for imaging different dyes. Second, *FLoupe* has designed and tested two prototypes (*FLoupe-1* and *FLoupe-2*) for real-time imaging of Fluorescein and 5-ALA, respectively. In other words, *FLoupe* has demonstrated the potential to incorporate into other surgical settings beyond brain tumor surgeries using different visible dyes. Third, *FLoupe* has integrated a small video camera with a dedicated emission filter frame for continuous video recording of fluorescence images at the surgical site and real-time displaying on the OR monitor. Real-time video recording is critical for comparison of *FLoupe* and PENTERO® 900 measurements, which supports a substantial equivalence determination between the two imaging systems. The comparison results can be used to apply for FDA clearance. Moreover, the real-time display

on the OR monitor allows the surgical team with immediate feedback and other trainees (e.g., residents) to observe and discuss the surgical operation.

Based on neurosurgeons' feedback in this pilot study, we are currently further optimizing the headlights (LEDs), video camera, emission filters, electrical control system, and mechanical design of *FLoupe* devices in terms of weight, size, imaging quality, and ease to wear/operate. The optimized *FLoupe* devices will be calibrated and validated against the PENTERO® 900 system for equivalence to image fluorescent MGs in a large group of patients. We expect that fluorescence images taken at the surgical site and from biopsied samples by both devices will be equivalent and agree with the blinded histopathological analyses (the gold standard). Resulting data will be used for FDA clearance via the pre-market notification 510(k) submission with the PENTERO® 900 system as the primary predicate.

CHAPTER 5. STUDY SUMMARY, INNOVATION, LIMITATIONS, AND FUTURE PERSPECTIVE

5.1 Development of scDCT/DSCT for Imaging Cerebral Blood Flow and Detecting Low Frequency Oscillations

5.1.1 Study Summary and Innovation

Among various NIR instruments, our noncontact scDCT enables continuous 3-D imaging of CBF distributions for use across a wide range of subjects with varied head scales/sizes including rodent, neonatal piglet, and human preterm infant [55, 59, 60]. In contrast with the NIRS, DCS, and HD-DOT systems that use discrete detectors, our scDCT uses a CMOS camera with thousands of pixels to serve as parallel 2-D detectors, which dramatically increases the sampling density and enables a wide FOV. The light source is directed to an electronic-controlled galvo-mirror which can rapidly scan the FOV with flexible patterns of desired source density. These benefits are combined with a unique FEM-based reconstruction technique capable of incorporating complex surface geometries and known tissue properties [64, 102, 103]. The scDCT system was, however, hindered for extracting LFOs due to its insufficient temporal sampling rate.

I presented an innovative fast scDCT method for 3-D imaging of CBF distributions, which enables the extraction of LFOs from deep brains of neonatal piglets. Results from this pilot study show the feasibility of scDCT in the growing area of LFO analysis, which has many advantages over other methods for neurologic studies and potential clinical applications.

I also presented a novel depth-sensitive DSCT method with parallel computation for analyzing scDCT data to achieve fast and high-density 2-D mapping of CBF

distributions at different depths without the need for complex and time-consuming 3-D reconstruction. The performance of DSCT was evaluated in head-simulating tissue phantoms and *in-vivo* experiments in adult rats.

Since the hardware for data acquisition in the scDCT and DSCT are essentially the same, they share the same advanced features including noncontact hardware, flexible S-D configuration, adjustable ROI/FOV, and a cost-effective instrument. Compared to the scDCT technique with 3-D reconstruction, however, DSCT method with fast sampling rate and parallel computation enables fast and high-density 2-D mapping of blood flow distributions at different depths.

5.1.2 My Contribution to the Study

In the studies reported in **Chapter 2**, I optimized the scDCT system for the detection of LFOs within CBF variations in neonatal piglets. Neonatal piglets were selected as model subjects due to their mid-range head size, high anatomical similarity and translational potential to human neonates, and our recent success with original scDCT techniques for comparisons [55, 104]. I optimized the numbers of scanning sources and detectors in the scDCT to balance temporal and spatial resolutions of CBF imaging to examine regional brain responses and derive LFOs after signal filtering. I adapted a moving window 3-D reconstruction method to achieve a fast sampling rate of 5 Hz, which is much higher than that with conventional reconstruction method (e.g., 0.2 Hz) [18, 55]. This sampling rate (5 Hz) is faster than typical cardiac and respiratory rates in neonatal piglets (<2.5 Hz), thus allowing removal of their contributions to CBF signals using simple lowpass filters. Moreover, reconstruction of a single 3-D image in previous studies took minutes to hours depending on the size of mesh nodes [55, 64, 105, 106]. In response, I

developed a new 3-D reconstruction algorithm using parallelization functionalities in MATLAB (MathWorks) to achieve a sizable increase in reconstruction speed while maintaining reconstruction quality. As a result, computation time for 3-D reconstruction in this study was reduced from 15 minutes to 50 seconds. With these notable improvements, LFOs in piglet brains were successfully isolated and quantified by the optimized scDCT technique.

For the animal studies, I worked closely with colleagues from the Division of Laboratory Animal Resources (DLAR) facility and got their assistance for safe handling and proper feeding of the piglets. One aspect of the project involved developing a precise planning system for overnight feeding of the animals. Working closely with my colleagues, I devised a well-coordinated schedule that ensured the piglets received proper nutrition while adhering to experimental requirements. Additionally, I collaborated with Dr. Lei Chen, who played a crucial role in performing the animal surgeries and monitoring throughout the *in-vivo* animal experiments.

This pilot preclinical study served as a vital and straightforward step towards using the optimized scDCT to map cerebral FC maps in human newborns. I incorporated initial findings from these studies in my proposal to the American Heart Association (AHA) and was honored to receive the AHA Predoctoral Fellowship in 2021 for a two-year period (2021-2023) to support my PhD dissertation research. The outcomes of these studies have been published in the Journal of Biomedical Optics (2023) [129].

In the studies reported in **Chapter 3**, I adapted and optimized a novel depth-sensitive DSCT method for rapid 2-D mapping of blood flow distributions in deep brains. Specifically, DSCT takes advantages of Image Processing Toolbox™ and Parallel

Computing Toolbox™ functions in MATLAB to rapidly generate a 2-D map of CBF. To achieve fast calculation of speckle contrast values from raw intensity images, I used MATLAB's built-in 2-D convolution function from the Image Processing Toolbox™. Since raw intensity images obtained at different source positions are independent, multiple 2-D speckle contrast images at different depths (by selecting different S-D separations) are computed and generated simultaneously by executing parallel loop iterations using MATLAB's Parallel Computing Toolbox™. The use of parallel computing with high performance CPUs reduced the processing time significantly in contrast to the inefficient *for-loops* method. To tackle low temporal resolution during high density scanning for capturing dynamic rCBF variations, I employed a moving window method to increase the temporal resolution of DSCT [18, 129], where a new 2-D CBF map was produced as soon as the raw image from one new source position data became available.

To evaluate the effect of sampling density on spatial resolution and depth sensitivity of DSCT method for 2-D flow mapping, new head-simulating layered phantoms with UK logo were fabricated by a 3-D printing technique. The phantoms were printed with a top solid layer to mimic the skull (no flow) and the UK logo filled by a liquid phantom solution (with Intralipid particle flow). I demonstrated how increasing the sampling density can enhance spatial resolution, albeit at the cost of longer data acquisition time. As a result, achieving an optimal balance between spatial and temporal resolutions becomes essential for specific applications. Results from sequential DSCT and LSCI measurements demonstrate that DSCT enables 2-D mapping of particle flow at different depths through the top layer (“skull”) with varied thicknesses of 1-3 mm. By contrast, LSCI can barely map the UK logo phantoms with top layer thickness of ≥ 1 mm.

Based on phantom test results, I optimized DSCT's setup for *in-vivo* animal experiments. I tested the ability of DSCT for continuous monitoring of temporal and spatial variations in rCBF by imaging global rCBF increases during CO₂ inhalations and regional rCBF decreases during CCA ligations in adult rats. The results of these studies suggest that both DSCT and scDCT enable the detection of global and regional rCBF changes in deep brains. However, DSCT achieves fast and high-density 2-D mapping of CBF distributions at different depths without the need of complex and time-consuming 3-D reconstruction in scDCT. Results from these studies have been submitted to the Neurophotonics (under revision, 2023) [150].

5.1.3 Study Limitation and Future Perspective

The relatively small sample sizes of subjects enrolled (2 piglets and 6 rats) present a constraint on our statistical analyses and study power. The significance of these pilot studies lies in paving the way towards larger-scale investigations, where more subjects will be enrolled. The optical properties (e.g., absorption and scattering coefficients) are known to have an influence on CBF calculations, which are assumed from the literature [117]. Recently, a two-step fitting algorithm successfully extracted tissue absorption and blood flow simultaneously using the scDCT [118]. This solution can improve flow reconstruction accuracy. Moreover, future utilization of multiple wavelengths in the scDCT would make it possible to measure CBF, cerebral oxygenation, and other derivatives (e.g., tissue oxidative metabolism) [117, 119, 120]. We note that new scDCT and DSCT systems with fast sampling rate can be used to map FC in the brain. The FC can be assessed by quantifying temporal correlations in LFOs across different regions of the brain, which enables depicting the functional network in the brain [40].

The head-simulating tissue phantoms provide significant flow contrasts between the solid and liquid phantoms. The relative flow contrast maps were generated by normalizing the measured flow indices to their mean values within the ROI, obtained from both solid and liquid phantoms. This normalization somewhat reduces the flow contrast between solid and liquid phantoms. Moreover, the partial volume effect from the top layer of solid phantom (no flow) also resulted in an underestimation of flow index in the deep liquid phantom, although DSCT enabled depth-sensitivity mapping with selected S-D distances. In the future, flow-simulating phantoms with different Intralipid particle flow rates will be used to further calibrate the new DSCT method.

Currently, our primary focus in scDCT/DSCT techniques is on continuously monitoring relative blood flow values. Absolute blood flow measurements are desirable because they provide crucial quantitative information with a flow unit (ml/min/100g) within tissues or organs. For example, when comparing data across different studies and different patient populations, absolute measurements ensure direct and longitudinal comparisons over time. Absolute measurements with scDCT/DSCT may be achieved by using methods of multiple exposure times and multiple S-D separations [151-153], which will be the subject of our future studies. Also, the head-simulating tissue phantoms will be used to calibrate and evaluate the system before *in-vivo* experiments.

5.2 Development of *FLoupe* for Intraoperative Identification of Human Brain Tumors

5.2.1 Study Summary and Innovation

I presented a low-cost wearable *FLoupe* device (US Patent Application #62/530,613, 2017), which are attached to wearable surgical eye loupes to help

neurosurgeons easily and accurately identify fluorescent MGs for safe and maximal tumor removal. We have tested two *FLoupe* prototypes for real-time imaging of Fluorescein and 5-ALA contrasts respectively in a small group of patients with MGs. Comparable results were observed against the standard neurosurgical operative microscope (PENTERO® 900) with fluorescence kits.

Our *FLoupe* technology provides unique advancements over other competitors' fluorescence imaging technologies, specifically for the guidance of brain cancer resection. Compared to expensive, large, stationary, neurosurgical operative microscopes (e.g., PENTERO® 900) [81, 85], *FLoupe* devices are affordable and wearable and allow for a greater range of movement, less obstruction, and faster/easier operation. This affordable and wearable device significantly increases the ability of more surgeons to conduct fast and thorough operations, and thus improving patient safety and outcomes. Moreover, this low-cost allows for procurement of multiple devices, thus alleviating costs for maintenance and downtime for device repair/replacement.

5.2.2 My Contribution to the Study

In the studies reported in **Chapter 4**, I invented a low-cost, wearable fluorescence eye loupe (*FLoupe*) device for intraoperative imaging of brain tissue perfusion. The *FLoupe* is specifically designed for intraoperative visualization of brain tumor margins in clinical settings, with the aim of enhancing surgical procedures through fluorescence-guided surgery. *FLoupe* was developed by integrating miniaturized light sources, flippable filters, and a recording camera to the surgical eye loupes. Two *FLoupe* prototypes were constructed for imaging of Fluorescein and 5-ALA, respectively. I collaborated with the technicians at SurgiTel, a world-leading manufacturer and supplier of eye loupes,

headlights, and video cameras regarding the development of *FLoupe-2*. Additionally, I collaborated with a neurosurgeon at a UK hospital, conducting intraoperative evaluations of the *FLoupe* in patients with primary malignant brain tumors. Comparable results were observed against the standard neurosurgical operative microscope (PENTERO® 900) with fluorescence kits. The results from this study have been submitted to the IEEE Journal of Translational Engineering in Health and Medicine for review. Preliminary data from the pilot study were incorporated into a STTR proposal to the NIH, leading to an STTR Phase-2 Award.

Over the span of this dissertation, I took on a leadership role in leading all three projects (**Chapters 2-4**). From the initial conceptions to ultimate completions of the instrumentations, experiments, and manuscripts, I was responsible for coordinating and executing all phases of studies including instrumentation, experimental design, data collection, data analysis, data interpretation, and manuscript writing.

5.2.3 Study Limitation and Future Perspective

One major limitation is the small number of subjects (11 patients with MGs). However, we believe this feasibility study is an important and necessary step towards larger clinical studies that would enroll more subjects to further validate the innovative *FLoupe* technique. Based on neurosurgeons' feedback in this pilot study, we are currently further optimizing the headlights (LEDs), video camera, emission filters, electrical control system, and mechanical design of *FLoupe* devices in terms of weight, size, imaging quality, and ease to wear/operate. The optimized *FLoupe* devices will be calibrated and validated against the PENTERO® 900 system for equivalence to image fluorescent MGs in a large group of patients. We expect that fluorescence images taken at the surgical site and from

biopsied samples by both devices will be equivalent and agree with the blinded histopathological analyses (the gold standard). The resulting data will be used for FDA clearance via the pre-market notification 510(k) submission with the PENTERO® 900 system as the primary predicate.

5.3 My Contribution to Other Studies

During my dissertation study period, I have also been involved in the design and development of a time-resolved laser speckle contrast imaging (TR-LSCI) of cerebral blood flow. The TR-LSCI illuminates picosecond-pulsed, coherent, widefield near-infrared light onto the head and synchronizes a newly developed, high-resolution, picosecond-gated SwissSPAD2 camera to capture CBF maps at different depths. My contributions also extended to the design and advancement of a multiple-wavelength speckle contrast diffuse correlation tomography (MW-scDCT) system. This innovative system enabled noncontact imaging of both blood flow and oxygenation distributions in deep tissues. I also participated in clinical studies with scDCT to assess blood flow distributions in mastectomy skin flaps in patients with breast cancers [56] and longitudinal imaging of CBF distributions in preterm infants.

APPENDIX. GLOSSARY

Terms	Descriptions
AHA	American Heart Association
ASL-MRI	Arterial-Spin-Labeled Magnetic Resonance Imaging
ANOVA	Analysis of Variance
AUC	Area Under-the-Curve
BFI	Blood Flow Indices
BOLD	Blood-oxygen-level-dependent
BPM	Heartbeat per Minute
CBF	Cerebral Blood Flow
CCA	Common Cerebral Artery
CCD	Charge-Coupled-Device
CMOS	Complementary Metal–Oxide–Semiconductor
DCS	Diffuse Correlation Spectroscopy
DLAR	Division of Laboratory Animal Resources
DSCT	Depth-Sensitive Diffuse Speckle Contrast Topography
EEG	Electroencephalography
EtCO ₂	End-Tidal Carbon Dioxide
FC	Functional Connectivity
FDA	Federal Drug Administration
FEM	Finite-Element-Method
FLoupe	Fluorescence Eye Loupe
FMRI	Functional Magnetic Resonance Imaging

fNIRS	Functional Near-Infrared Spectroscopy
FOV	Field-of-View
FWHM	Full Width at Half-Maximum
GBM	Glioblastoma Multiforme
GPU	Graphics Processing Units
GTR	Gross-Total-Resection
Hb	Deoxy-Hemoglobin Concentration
HbO ₂	Oxy-Hemoglobin Concentration
HD-DOT	High-Density Diffuse Optical Tomography
HPC	High-Performance Computing
HWHM	Half-Width-at-Half-Maximum
IACUC	Institutional Animal Care and Use Committee
IDH	Isocitrate Dehydrogenase
IRB	Institutional Review Board
IVH	Intraventricular Hemorrhage
LFOs	Low-Frequency Oscillations
LH	Left Hemisphere
LSCI	Laser Speckle Contrast Imaging
MEG	Magnetoencephalography
MGs	Malignant Gliomas
M-NIRFAST	Modified Near-Infrared Fluorescence and Spectral Tomography
MRI	Magnetic Resonance Imaging
NIR	Near-Infrared

NIRS	Near-Infrared Spectroscopy
OISI	Optical Intrinsic Signal Imaging
OR	Operating Room
PCT	Perfusion Computed Tomography
PET	Positron Emission Tomography
PpIX	Phototoxic Protoporphyrin IX
PSD	Power Spectral Density
rCBF	Relative Change in Cerebral Blood Flow
RH	Righ Hemisphere
ROI	Region of Interest
RPM	Respiration Per Minute
rs-FC	Resting-State Functional Connectivity
scDCT	Speckle Contrast Diffuse Correlation Tomography
sCMOS	Scientific Complementary Metal–Oxide–Semiconductor
S-D	Source-Detector
SNR	Signal-to-Noise Ratios
SpO ₂	Peripheral Artery Blood Oxygen Saturation
StO ₂	Blood Oxygen Saturation
TBI	Traumatic Brain Injury
TiO ₂	Titanium Dioxide
TR-LSCI	Time-Resolved Laser Speckle Contrast Imaging
UK	University of Kentucky
WHO	World Health Organization

XeCT	Xenon-Enhanced Computed Tomography
2-D	Two-Dimensional
3-D	Three-Dimensional
5-ALA	5-Aminolevulinic Acid

REFERENCES

1. Raichle, M.E. and D.A. Gusnard, *Appraising the brain's energy budget*. Proceedings of the National Academy of Sciences, 2002. 99(16): p. 10237-10239.
2. Attwell, D., et al., *Glial and neuronal control of brain blood flow*. Nature, 2010. 468(7321): p. 232-243.
3. Yu, G., *Diffuse correlation spectroscopy (DCS): a diagnostic tool for assessing tissue blood flow in vascular-related diseases and therapies*. Current Medical Imaging, 2012. 8(3): p. 194-210.
4. Bračić, M. and A. Stefanovska, *Wavelet-based analysis of human blood-flow dynamics*. Bulletin of mathematical biology, 1998. 60(5): p. 919-935.
5. Lang, E.W., et al., *Spontaneous oscillations of arterial blood pressure, cerebral and peripheral blood flow in healthy and comatose subjects*. Neurological research, 1999. 21(7): p. 665-669.
6. Pinti, P., D. Cardone, and A. Merla, *Simultaneous fNIRS and thermal infrared imaging during cognitive task reveal autonomic correlates of prefrontal cortex activity*. Scientific reports, 2015. 5(1): p. 1-14.
7. White, B.R., et al., *Bedside optical imaging of occipital resting-state functional connectivity in neonates*. Neuroimage, 2012. 59(3): p. 2529-2538.
8. Wang, J., et al., *Low-frequency fluctuations amplitude signals exhibit abnormalities of intrinsic brain activities and reflect cognitive impairment in leukoaraiosis patients*. Medical Science Monitor: International Medical Journal of Experimental and Clinical Research, 2019. 25: p. 5219.
9. White, B.R., et al., *Imaging of functional connectivity in the mouse brain*. PloS one, 2011. 6(1): p. e16322.
10. White, B.R., et al., *Low frequency power in cerebral blood flow is a biomarker of neurologic injury in the acute period after cardiac arrest*. Resuscitation, 2022. 178: p. 12-18.
11. Li, J.M., W.J. Bentley, and L.H. Snyder, *Functional connectivity arises from a slow rhythmic mechanism*. Proceedings of the National Academy of Sciences, 2015. 112(19): p. E2527-E2535.
12. Braun, R.D., R.A. Linsenmeier, and C.M. Yancey, *Spontaneous fluctuations in oxygen tension in the cat retina*. Microvascular research, 1992. 44(1): p. 73-84.
13. Padnick, L.B., R.A. Linsenmeier, and T.K. Goldstick, *Oxygenation of the cat primary visual cortex*. Journal of applied physiology, 1999. 86(5): p. 1490-1496.
14. Linsenmeier, R.A., et al., *Spontaneous Fluctuations of PO₂ in the Rabbit Somatosensory Cortex*, in *Oxygen Transport to Tissue XXXVII*. 2016, Springer. p. 311-317.
15. Zhang, Q., K.W. Gheres, and P.J. Drew, *Origins of 1/f-like tissue oxygenation fluctuations in the murine cortex*. PLoS biology, 2021. 19(7): p. e3001298.
16. Lu, H., et al., *Synchronized delta oscillations correlate with the resting-state functional MRI signal*. Proceedings of the National Academy of Sciences, 2007. 104(46): p. 18265-18269.
17. Wang, D., et al., *Fast blood flow monitoring in deep tissues with real-time software correlators*. Biomedical optics express, 2016. 7(3): p. 776-797.

18. Dragojević, T., et al., *High-density speckle contrast optical tomography of cerebral blood flow response to functional stimuli in the rodent brain*. Neurophotonics, 2019. 6(4): p. 045001.
19. Lystad, R.P. and H. Pollard, *Functional neuroimaging: a brief overview and feasibility for use in chiropractic research*. The Journal of the Canadian Chiropractic Association, 2009. 53(1): p. 59.
20. Yu, G., Y. Lin, and C. Huang, *Noncontact three-dimensional diffuse optical imaging of deep tissue blood flow distribution*. United States Patent #9861319 (2016-2036), 2016.
21. Anderson, A.L. and M.E. Thomason, *Functional plasticity before the cradle: a review of neural functional imaging in the human fetus*. Neuroscience & Biobehavioral Reviews, 2013. 37(9): p. 2220-2232.
22. Rudroff, T., et al., *Positron emission tomography detects greater blood flow and less blood flow heterogeneity in the exercising skeletal muscles of old compared with young men during fatiguing contractions*. The Journal of physiology, 2014. 592(2): p. 337-349.
23. Chugani, H.T., *A critical period of brain development: studies of cerebral glucose utilization with PET*. Preventive medicine, 1998. 27(2): p. 184-188.
24. Papadelis, C., et al., *Current and emerging potential for magnetoencephalography in pediatric epilepsy*. Journal of Pediatric Epilepsy, 2013. 2(01): p. 073-085.
25. Barnes, J.J., et al., *Electrophysiological measures of resting state functional connectivity and their relationship with working memory capacity in childhood*. Developmental science, 2016. 19(1): p. 19-31.
26. Boas, D.A., A.M. Dale, and M.A. Franceschini, *Diffuse optical imaging of brain activation: approaches to optimizing image sensitivity, resolution, and accuracy*. Neuroimage, 2004. 23: p. S275-S288.
27. Shang, Y., et al., *Diffuse optical monitoring of repeated cerebral ischemia in mice*. Optics express, 2011. 19(21): p. 20301-20315.
28. Liao, S.M., et al., *Neonatal hemodynamic response to visual cortex activity: high-density near-infrared spectroscopy study*. Journal of biomedical optics, 2010. 15(2): p. 026010.
29. Ferradal, S.L., et al., *Functional imaging of the developing brain at the bedside using diffuse optical tomography*. Cerebral cortex, 2016. 26(4): p. 1558-1568.
30. Gore, J.C., *Principles and practice of functional MRI of the human brain*. The Journal of clinical investigation, 2003. 112(1): p. 4-9.
31. Hoptman, M.J., et al., *Amplitude of low-frequency oscillations in schizophrenia: a resting state fMRI study*. Schizophrenia research, 2010. 117(1): p. 13-20.
32. Han, Y., et al., *Anatomical and functional deficits in patients with amnesic mild cognitive impairment*. PloS one, 2012. 7(2): p. e28664.
33. Wang, Z., et al., *Spatial patterns of intrinsic brain activity in mild cognitive impairment and Alzheimer's disease: A resting-state functional MRI study*. Human brain mapping, 2011. 32(10): p. 1720-1740.
34. Wang, L., et al., *Amplitude of low-frequency oscillations in first-episode, treatment-naive patients with major depressive disorder: a resting-state functional MRI study*. PloS one, 2012. 7(10): p. e48658.

35. Gao, L., et al., *Frequency-dependent changes of local resting oscillations in sleep-deprived brain*. PLoS One, 2015. 10(3): p. e0120323.
36. Zhou, Y., et al., *Characterization of thalamo-cortical association using amplitude and connectivity of functional MRI in mild traumatic brain injury*. Journal of Magnetic Resonance Imaging, 2014. 39(6): p. 1558-1568.
37. Quan, X., et al., *Frequency-Specific Changes of Amplitude of Low-Frequency Fluctuations in Patients with Acute Basal Ganglia Ischemic Stroke*. Neural plasticity, 2022. 2022.
38. Wintermark, M., et al., *Comparative overview of brain perfusion imaging techniques*. Stroke, 2005. 36(9): p. e83-e99.
39. Kimberley, T.J. and S.M. Lewis, *Understanding neuroimaging*. Physical therapy, 2007. 87(6): p. 670-683.
40. Mohammadi-Nejad, A.-R., et al., *Neonatal brain resting-state functional connectivity imaging modalities*. Photoacoustics, 2018. 10: p. 1-19.
41. Durduran, T., et al., *Diffuse optics for tissue monitoring and tomography*. Reports on progress in physics, 2010. 73(7): p. 076701.
42. He, L., et al., *Using optical fibers with different modes to improve the signal-to-noise ratio of diffuse correlation spectroscopy flow-oximeter measurements*. Journal of biomedical optics, 2013. 18(3): p. 037001-037001.
43. Bender, N., et al., *Coherent enhancement of optical remission in diffusive media*. Proceedings of the National Academy of Sciences, 2022. 119(41): p. e2207089119.
44. Shang, Y., et al., *Portable optical tissue flow oximeter based on diffuse correlation spectroscopy*. Optics letters, 2009. 34(22): p. 3556-3558.
45. Carp, S.A., M.B. Robinson, and M.A. Franceschini, *Diffuse correlation spectroscopy: current status and future outlook*. Neurophotonics, 2023. 10(1): p. 013509-013509.
46. Bahrani, A.A., et al., *Diffuse optical assessment of cerebral-autoregulation in older adults stratified by cerebrovascular risk*. Journal of biophotonics, 2020. 13(10): p. e202000073.
47. Cheng, R., et al., *Noninvasive optical evaluation of spontaneous low frequency oscillations in cerebral hemodynamics*. Neuroimage, 2012. 62(3): p. 1445-1454.
48. Tong, Y. and B.d. Frederick, *Time lag dependent multimodal processing of concurrent fMRI and near-infrared spectroscopy (NIRS) data suggests a global circulatory origin for low-frequency oscillation signals in human brain*. Neuroimage, 2010. 53(2): p. 553-564.
49. Pierro, M.L., et al., *Phase-amplitude investigation of spontaneous low-frequency oscillations of cerebral hemodynamics with near-infrared spectroscopy: a sleep study in human subjects*. Neuroimage, 2012. 63(3): p. 1571-1584.
50. Hebden, J.C., et al., *Three-dimensional optical tomography of the premature infant brain*. Physics in Medicine & Biology, 2002. 47(23): p. 4155.
51. Zhang, X., *Instrumentation in Diffuse Optical Imaging*. Photonics, 2014. 1(1): p. 9-32.
52. Boas, D.A. and A.K. Dunn, *Laser speckle contrast imaging in biomedical optics*. Journal of biomedical optics, 2010. 15(1): p. 011109.
53. Dunn, A.K., *Laser speckle contrast imaging of cerebral blood flow*. Annals of biomedical engineering, 2012. 40(2): p. 367-377.

54. Fathi, F., et al. *Laser speckle contrast imaging of cerebral blood flow using picosecond pulsed laser illumination*. in *Multiscale Imaging and Spectroscopy III*. 2022. SPIE.
55. Huang, C., et al., *Speckle contrast diffuse correlation tomography of cerebral blood flow in perinatal disease model of neonatal piglets*. *Journal of Biophotonics*, 2021. 14(4): p. e202000366.
56. Mazdeyasna, S., et al., *Intraoperative Optical and Fluorescence Imaging of Blood Flow Distributions in Mastectomy Skin Flaps for Identifying Ischemic Tissues*. *Plastic and Reconstructive Surgery*, 2022. 150(2): p. 282-287.
57. Irwin, D., et al., *Near-infrared Speckle Contrast Diffuse Correlation Tomography for Noncontact Imaging of Tissue Blood Flow Distribution*. 2022: CRC Press.
58. Mohtasebi, M., et al., *Detection of low-frequency oscillations in neonatal piglets with speckle contrast diffuse correlation tomography*. *Journal of Biomedical Optics*, 2023. 28(12): p. 121204-121204.
59. Huang, C., et al., *Noninvasive noncontact speckle contrast diffuse correlation tomography of cerebral blood flow in rats*. *Neuroimage*, 2019. 198: p. 160-169.
60. Jawdeh, E.G.A., et al., *Noncontact optical imaging of brain hemodynamics in preterm infants: a preliminary study*. *Physics in Medicine & Biology*, 2020.
61. Mohtasebi, M., et al. *Noncontact optical assessment of spontaneous low-frequency fluctuations of cerebral blood flow in neonatal intraventricular hemorrhage*. in *Optical Techniques in Neurosurgery, Neurophotonics, and Optogenetics*. 2021. International Society for Optics and Photonics.
62. Mazdeyasna, S., et al., *Noncontact speckle contrast diffuse correlation tomography of blood flow distributions in tissues with arbitrary geometries*. *J Biomed Opt*, 2018. 23(9): p. 1-9.
63. Mohtasebi, M., et al. *Noncontact optical assessment of disrupted cerebral functional connectivity in a piglet model of transient ischemic stroke*. in *Clinical and Translational Neurophotonics 2022*. 2022. SPIE.
64. Lin, Y., et al., *Three-dimensional flow contrast imaging of deep tissue using noncontact diffuse correlation tomography*. *Applied Physics Letters*, 2014. 104(12): p. 121103.
65. Hoshi, Y. and Y. Yamada, *Overview of diffuse optical tomography and its clinical applications*. *Journal of biomedical optics*, 2016. 21(9): p. 091312.
66. Pratama, A.S., et al. *A UWB antenna for microwave brain imaging*. in *2015 IEEE 4th Asia-Pacific Conference on Antennas and Propagation (APCAP)*. 2015. IEEE.
67. Li, J.T., et al., *Targeting different types of human meningioma and glioma cells using a novel adenoviral vector expressing GFP-TRAIL fusion protein from hTERT promoter*. *Cancer Cell International*, 2011. 11(1): p. 1-14.
68. Maher, E.A., et al., *Malignant glioma: genetics and biology of a grave matter*. *Genes & development*, 2001. 15(11): p. 1311-1333.
69. Mesti, T. and J. Ocvirk, *Malignant gliomas: old and new systemic treatment approaches*. *Radiology and Oncology*, 2016. 50(2): p. 129-138.
70. Kuhnt, D., et al., *Correlation of the extent of tumor volume resection and patient survival in surgery of glioblastoma multiforme with high-field intraoperative MRI guidance*. *Neuro-oncology*, 2011. 13(12): p. 1339-1348.

71. Lacroix, M., et al., *A multivariate analysis of 416 patients with glioblastoma multiforme: prognosis, extent of resection, and survival*. Journal of neurosurgery, 2001. 95(2): p. 190-198.
72. McGirt, M.J., et al., *Independent association of extent of resection with survival in patients with malignant brain astrocytoma*. Journal of neurosurgery, 2009. 110(1): p. 156-162.
73. Stummer, W., et al., *Prospective cohort study of radiotherapy with concomitant and adjuvant temozolomide chemotherapy for glioblastoma patients with no or minimal residual enhancing tumor load after surgery*. Journal of neuro-oncology, 2012. 108(1): p. 89-97.
74. Stummer, W., et al., *Fluorescence-guided surgery with 5-aminolevulinic acid for resection of malignant glioma: a randomised controlled multicentre phase III trial*. The lancet oncology, 2006. 7(5): p. 392-401.
75. Aldave, G., et al., *Prognostic value of residual fluorescent tissue in glioblastoma patients after gross total resection in 5-aminolevulinic acid-guided surgery*. Neurosurgery, 2013. 72(6): p. 915-921.
76. Picart, T., et al., *Is fluorescence-guided surgery with 5-ala in eloquent areas for malignant gliomas a reasonable and useful technique?* Neurochirurgie, 2017. 63(3): p. 189-196.
77. Acerbi, F., et al., *Fluorescein-guided surgery for malignant gliomas: a review*. Neurosurgical review, 2014. 37(4): p. 547-557.
78. Belykh, E., et al., *Intraoperative fluorescence imaging for personalized brain tumor resection: current state and future directions*. Frontiers in surgery, 2016. 3: p. 55.
79. Xue, Z., et al., *Fluorescein-guided surgery for pediatric brainstem gliomas: preliminary study and technical notes*. Journal of Neurological Surgery Part B: Skull Base, 2018. 79(S 04): p. S340-S346.
80. Acerbi, F., et al., *Fluorescein-Guided Surgery for Resection of High-Grade Gliomas: A Multicentric Prospective Phase II Study (FLUOGLIO) Fluorescein-Guided Removal of High-Grade Gliomas*. Clinical Cancer Research, 2018. 24(1): p. 52-61.
81. Zhang, N., et al., *Sodium fluorescein-guided resection under the YELLOW 560 nm surgical microscope filter in malignant gliomas: our first 38 cases experience*. BioMed Research International, 2017. 2017.
82. Cole, K.L., et al., *The Role of Advanced Imaging in Neurosurgical Diagnosis*. Journal of modern medical imaging, 2023. 1.
83. Castellano, A., et al., *Functional MRI for surgery of gliomas*. Current treatment options in neurology, 2017. 19: p. 1-23.
84. Senders, J.T., et al., *Agents for fluorescence-guided glioma surgery: a systematic review of preclinical and clinical results*. Acta neurochirurgica, 2017. 159(1): p. 151-167.
85. Acerbi, F., et al., *Fluorescein-guided surgery for grade IV gliomas with a dedicated filter on the surgical microscope: preliminary results in 12 cases*. Acta neurochirurgica, 2013. 155(7): p. 1277-1286.

86. Zong, H., R.G. Verhaak, and P. Canoll, *The cellular origin for malignant glioma and prospects for clinical advancements*. Expert review of molecular diagnostics, 2012. 12(4): p. 383-394.
87. Suero Molina, E., et al., *Validating a new generation filter system for visualizing 5-ALA-induced PpIX fluorescence in malignant glioma surgery: a proof of principle study*. Acta Neurochirurgica, 2020. 162: p. 785-793.
88. Smith, K.J. and P.N. Ainslie, *Regulation of cerebral blood flow and metabolism during exercise*. Experimental Physiology, 2017. 102(11): p. 1356-1371.
89. Lecrux, C. and E. Hamel, *The neurovascular unit in brain function and disease*. Acta physiologica, 2011. 203(1): p. 47-59.
90. Bauer, A.Q., et al., *Optical imaging of disrupted functional connectivity following ischemic stroke in mice*. Neuroimage, 2014. 99: p. 388-401.
91. Wegrzyk, J., et al., *Identifying motor functional neurological disorder using resting-state functional connectivity*. NeuroImage: Clinical, 2018. 17: p. 163-168.
92. Tadayonnejad, R., et al., *Clinical, cognitive, and functional connectivity correlations of resting-state intrinsic brain activity alterations in unmedicated depression*. Journal of affective disorders, 2015. 172: p. 241-250.
93. Kim, Y.E., et al., *Altered trigeminothalamic spontaneous low-frequency oscillations in migraine without aura: a resting-state fMRI study*. BMC neurology, 2021. 21(1): p. 1-9.
94. Tocchio, S., et al. *MRI evaluation and safety in the developing brain*. in *Seminars in perinatology*. 2015. Elsevier.
95. Kalchenko, V., et al., *Combined laser speckle imaging and fluorescent intravital microscopy for monitoring acute vascular permeability reaction*. Journal of Biomedical Optics, 2019. 24(6): p. 060501-060501.
96. Teichert, M. and J. Bolz, *Simultaneous intrinsic signal imaging of auditory and visual cortex reveals profound effects of acute hearing loss on visual processing*. Neuroimage, 2017. 159: p. 459-472.
97. Zhou, Q., et al., *Multisensory interplay within human auditory cortex: new evidence from intraoperative optical imaging of intrinsic signal*. World Neurosurgery, 2017. 98: p. 251-257.
98. Biccato, G., et al., *Increase in Low-Frequency Oscillations in fNIRS as Cerebral Response to Auditory Stimulation with Familiar Music*. Brain Sciences, 2021. 12(1): p. 42.
99. Urban, K.J., et al., *Functional near-infrared spectroscopy reveals reduced interhemispheric cortical communication after pediatric concussion*. Journal of neurotrauma, 2015. 32(11): p. 833-840.
100. Hocke, L.M., et al., *Reduced functional connectivity in adults with persistent post-concussion symptoms: a functional near-infrared spectroscopy study*. Journal of neurotrauma, 2018. 35(11): p. 1224-1232.
101. Andersen, A.V., et al., *Assessing low-frequency oscillations in cerebrovascular diseases and related conditions with near-infrared spectroscopy: a plausible method for evaluating cerebral autoregulation?* Neurophotonics, 2018. 5(3): p. 030901.
102. Huang, C., et al., *Speckle contrast diffuse correlation tomography of complex turbid medium flow*. Medical physics, 2015. 42(7): p. 4000-4006.

103. Huang, C., et al., *Noncontact 3-D speckle contrast diffuse correlation tomography of tissue blood flow distribution*. IEEE transactions on medical imaging, 2017. 36(10): p. 2068-2076.
104. Mohtasebi, M., et al. *Noncontact optical assessment of spontaneous low-frequency fluctuations of cerebral blood flow in neonatal intraventricular hemorrhage*. in *optical techniques in neurosurgery, Neurophotonics, and Optogenetics*. 2021. SPIE.
105. Huang, C., et al., *Alignment of sources and detectors on breast surface for noncontact diffuse correlation tomography of breast tumors*. Applied optics, 2015. 54(29): p. 8808-8816.
106. He, L., et al., *Noncontact diffuse correlation tomography of human breast tumor*. Journal of biomedical optics, 2015. 20(8): p. 86003-86003.
107. Huang, C., et al., *Noncontact speckle contrast diffuse correlation tomography of tissue blood flow distribution*. IEEE Transactions on Medical Imaging, 2017. 36(10): p. 2068-2076.
108. Zhao, M., et al., *Noncontact Speckle Contrast Diffuse Correlation Tomography of Blood Flow Distributions in Burn Wounds: A Preliminary Study*. Military Medicine, 2020. 185(Supplement_1): p. 82-87.
109. Otsu, N., *A threshold selection method from gray-level histograms*. IEEE transactions on systems, man, and cybernetics, 1979. 9(1): p. 62-66.
110. Obrig, H., et al., *Spontaneous low frequency oscillations of cerebral hemodynamics and metabolism in human adults*. Neuroimage, 2000. 12(6): p. 623-639.
111. Welch, P., *The use of fast Fourier transform for the estimation of power spectra: a method based on time averaging over short, modified periodograms*. IEEE Transactions on audio and electroacoustics, 1967. 15(2): p. 70-73.
112. Liao, L.-D., et al., *Neurovascular coupling: in vivo optical techniques for functional brain imaging*. Biomedical engineering online, 2013. 12: p. 1-20.
113. Zhang, L. and J. Zhao, *Amplitude of Low-Frequency Oscillations in First-Episode Drug-Naive Patients with Major Depressive Disorder: A Resting State Functional Magnetic Resonance Imaging Study*. Neuropsychiatric Disease and Treatment, 2022. 18: p. 555.
114. Yeo, C., et al., *Low frequency oscillations assessed by diffuse speckle contrast analysis for foot angiosome concept*. Scientific Reports, 2020. 10(1): p. 1-14.
115. Astashev, M., D. Serov, and A. Tankanag, *Anesthesia effects on the low frequency blood flow oscillations in mouse skin*. Skin Research and Technology, 2019. 25(1): p. 40-46.
116. Podtaev, S., M. Morozov, and P. Frick, *Wavelet-based correlations of skin temperature and blood flow oscillations*. Cardiovascular Engineering, 2008. 8: p. 185-189.
117. Roche-Labarbe, N., et al., *Somatosensory evoked changes in cerebral oxygen consumption measured non-invasively in premature neonates*. Neuroimage, 2014. 85: p. 279-286.
118. Zhao, M., et al., *Extraction of tissue optical property and blood flow from speckle contrast diffuse correlation tomography (scDCT) measurements*. Biomedical Optics Express, 2021. 12(9): p. 5894-5908.

119. Roche-Labarbe, N., et al., *Noninvasive optical measures of CBV, StO₂, CBF index, and rCMRO₂ in human premature neonates' brains in the first six weeks of life*. Human brain mapping, 2010. 31(3): p. 341-352.
120. Diop, M., et al., *Development of a combined broadband near-infrared and diffusion correlation system for monitoring cerebral blood flow and oxidative metabolism in preterm infants*. Biomedical optics express, 2015. 6(10): p. 3907-3918.
121. Zou, Q.-H., et al., *An improved approach to detection of amplitude of low-frequency fluctuation (ALFF) for resting-state fMRI: fractional ALFF*. Journal of neuroscience methods, 2008. 172(1): p. 137-141.
122. Yodh, A. and B. Chance, *Spectroscopy and imaging with diffusing light*. Physics today, 1995. 48(3): p. 34-41.
123. Zhou, C., et al., *Diffuse optical correlation tomography of cerebral blood flow during cortical spreading depression in rat brain*. Optics express, 2006. 14(3): p. 1125-1144.
124. Shang, Y., et al., *Diffuse optical monitoring of repeated cerebral ischemia in mice*. Opt Express, 2011. 19(21): p. 20301-15.
125. Chen, L., et al., *Novel experimental model for repeated forebrain ischemia-reperfusion*. Journal of experimental stroke and translational medicine, 2012. 5(1): p. 1-10.
126. Blanco, I., et al., *Longitudinal, transcranial measurement of functional activation in the rat brain by diffuse correlation spectroscopy*. Neurophotonics, 2017. 4(4): p. 045006.
127. Varma, H.M., et al., *Speckle contrast optical tomography: A new method for deep tissue three-dimensional tomography of blood flow*. Biomedical optics express, 2014. 5(4): p. 1275-1289.
128. Dragojević, T., et al., *High-density speckle contrast optical tomography (SCOT) for three dimensional tomographic imaging of the small animal brain*. NeuroImage, 2017. 153: p. 283-292.
129. Mohtasebi, M., et al., *Detection of low-frequency oscillations in neonatal piglets with speckle contrast diffuse correlation tomography*. Journal of Biomedical Optics, 2023. 28(12): p. 121204.
130. Mazdeyasna, S., et al., *Intraoperative optical and fluorescence imaging of blood flow distributions in mastectomy skin flaps for identifying ischemic tissues*. Plastic and reconstructive surgery, 2022. 150(2): p. 282.
131. Mozumder, M., et al., *A model-based iterative learning approach for diffuse optical tomography*. IEEE Transactions on Medical Imaging, 2021. 41(5): p. 1289-1299.
132. Irwin, D., et al., *Influences of tissue absorption and scattering on diffuse correlation spectroscopy blood flow measurements*. Biomedical optics express, 2011. 2(7): p. 1969-1985.
133. Liu, C., et al., *Choosing a model for laser speckle contrast imaging*. Biomedical Optics Express, 2021. 12(6): p. 3571-3583.
134. Basak, K., M. Manjunatha, and P.K. Dutta, *Review of laser speckle-based analysis in medical imaging*. Medical & biological engineering & computing, 2012. 50(6): p. 547-558.

135. Patel, D.D., et al., *Development of a preclinical laser speckle contrast imaging instrument for assessing systemic and retinal vascular function in small rodents*. *Translational Vision Science & Technology*, 2021. 10(9): p. 19-19.
136. Altman, Y.M., *Accelerating MATLAB Performance: 1001 tips to speed up MATLAB programs*. 2014: CRC Press.
137. Singh, D., et al., *A fast algorithm towards real-time laser speckle contrast imaging*. *Journal of biomedical optics*, 2022. 15(1): p. 011109.
138. Lamouche, G., et al., *Review of tissue simulating phantoms with controllable optical, mechanical and structural properties for use in optical coherence tomography*. *Biomedical optics express*, 2012. 3(6): p. 1381-1398.
139. Bentz, B.Z., et al., *Printed optics: phantoms for quantitative deep tissue fluorescence imaging*. *Optics letters*, 2016. 41(22): p. 5230-5233.
140. Boas, D.A., et al., *Establishing the diffuse correlation spectroscopy signal relationship with blood flow*. *Neurophotonics*, 2016. 3(3): p. 031412.
141. Tiernan, J., et al., *Intra-operative tumour detection and staging in colorectal cancer surgery*. *Colorectal Disease*, 2012. 14(9): p. e510-e520.
142. Belykh, E., et al., *Blood-brain barrier, blood-brain tumor barrier, and fluorescence-guided neurosurgical oncology: delivering optical labels to brain tumors*. *Frontiers in Oncology*, 2020. 10: p. 739.
143. Alston, L., et al., *Spectral complexity of 5-ALA induced PpIX fluorescence in guided surgery: a clinical study towards the discrimination of healthy tissue and margin boundaries in high and low grade gliomas*. *Biomedical optics express*, 2019. 10(5): p. 2478-2492.
144. Zhang, D.Y., S. Singhal, and J.Y. Lee, *Optical principles of fluorescence-guided brain tumor surgery: a practical primer for the neurosurgeon*. *Neurosurgery*, 2019. 85(3): p. 312-324.
145. Craig, S.E., et al., *Fluorescent-guided surgical resection of glioma with targeted molecular imaging agents: a literature review*. *World neurosurgery*, 2016. 90: p. 154-163.
146. Schucht, P., et al., *Gross total resection rates in contemporary glioblastoma surgery: results of an institutional protocol combining 5-aminolevulinic acid intraoperative fluorescence imaging and brain mapping*. *Neurosurgery*, 2012. 71(5): p. 927-936.
147. Ahmed, R., et al., *Malignant gliomas: current perspectives in diagnosis, treatment, and early response assessment using advanced quantitative imaging methods*. *Cancer management and research*, 2014: p. 149-170.
148. Georgescu, M.-M., *Multi-platform classification of IDH-wild-type glioblastoma based on ERK/MAPK pathway: diagnostic, prognostic and therapeutic implications*. *Cancers*, 2021. 13(18): p. 4532.
149. Zhang, X., et al., *A novel 5-aminolevulinic acid-enabled surgical loupe system—a consecutive brain tumor series of 11 cases*. *Operative Neurosurgery*, 2022. 22(5): p. 298-304.
150. Mohtasebi, M., et al., *Depth-sensitive diffuse speckle contrast topography (DSCT) for high-density mapping of cerebral blood flow in rodents*. *Neurophotonics*, under revision, 2023.

151. Liu, J., et al., *Simultaneously extracting multiple parameters via multi-distance and multi-exposure diffuse speckle contrast analysis*. Biomedical Optics Express, 2017. 8(10): p. 4537-4550.
152. Valdes, C.P., et al., *Speckle contrast optical spectroscopy, a non-invasive, diffuse optical method for measuring microvascular blood flow in tissue*. Biomedical optics express, 2014. 5(8): p. 2769-2784.
153. Liu, J., et al., *Quantitative model of diffuse speckle contrast analysis for flow measurement*. Journal of Biomedical Optics, 2017. 22(7): p. 076016-076016.

VITA

Mehrana Mohtasebi

Education

University of Kentucky, Lexington, KY

Doctor of Philosophy, Biomedical Engineering 2018–Present

Dissertation Title: Multiscale and Multimodality Optical Imaging of Brain

Hemodynamics and Function

Advisor: Professor Guoqiang Yu

GPA: 3.72

K. N. Toosi University of Technology, Tehran, Iran

Master of Science, Biomedical Engineering – Bioelectric 2013–2015

Dissertation Title: Modeling of Neonatal Skull Development Using Computed Tomography Images

Advisor: Professor Hamid Abrishami Moghaddam

GPA: 3.90

Sahand University of Technology, Tabriz, Iran

Bachelor of Science, Electrical Engineering – Control 2009–2013

GPA: 3.73

Farzanegan High School, Tehran, Iran

Diploma in Physics and Mathematics Discipline 2004–2008

Affiliated with the National Organization for the Development of Exceptional Talents (NODET)

Fellowships and Awards

- The Sarah Bennett Holmes Graduate Student Award Winner, 2022
- The Judges Choice Award in the University of Kentucky Von Allmen Center for Entrepreneurship Poster Pitch competition, 2022
- The American Heart Association (AHA) Predoctoral Fellowship, 2021
 - The AHA Predoctoral Fellowship with an outstanding ranking of top 15.51% for two years (2021-2023) to support my PhD dissertation work.
- F. Joseph Halcomb III, M.D. Department of Biomedical Engineering Outstanding Graduate Student (Doctoral) Award, 2021
- SPIE Photonics West Student Author Conference Support, 2021
- Successfully completed the Global Health Case Competition, 2021
- Finalist of The Halcomb Fellowship in Medicine and Engineering, University of Kentucky, 2020
 - Reviewed based on the written proposal.
- Biomedical Engineering Society (BMES) Career Development Award, 2020
 - Winners are selected among a pool of international applicants including graduate students, postdoctoral fellows and early career professionals involved in research and training focused on health disparities and minority health.

- Ranked 3rd based on GPA among all the students in the Biomedical Engineering program at K.N. Toosi University of Technology, 2015
- Honor student privilege award from Iran ministry of science and technology, 2013
- Ranked 2nd based on GPA among all the students in the Electrical Engineering - Control program at Sahand University of Technology, 2013
- Talented Student Awards - a member of Talented Students in all B.Sc. semesters because of high GPA and excellent performance (2010 - 2013)
- Selected for study in schools of National Organization for Development of Exceptional Talents (NODET) through an exam with less than 1 percent acceptance rate, 2004

Professional Experience

Sep 2018 – Oct 2023

Research Assistant at Biomedical Optics Lab

Department of Biomedical Engineering, University of Kentucky, Lexington, Kentucky
Mentor: Professor Guoqiang Yu

Jan 2014 – Dec 2016

Research Assistant at Machine Vision and Medical Image Processing Lab

Department of Biomedical Engineering, K.N. Toosi University of Technology, Tehran, Iran
Mentor: Professor Hamid Abrishami Moghaddam

Peer-Reviewed Journal/Conference Publications

1. **M. Mohtasebi**, D. Irwin, D. Singh, S. Mazdeyasna, X. Liu, S. Rabienia Haratbar, F. Fathi, C. Huang, K. E. Saatman, L. Chen, G. Yu. " Detection of Low-Frequency Oscillations in Neonatal Piglets with Speckle Contrast Diffuse Correlation Tomography", Journal of Biomedical Optics, DOI: 10.1117/1.JBO.28.12.121204 (2023)
2. **M. Mohtasebi**, M. Bayat, S. Ghadimi, H. Abrishami Moghaddam, and F. Wallois. "Modeling of Neonatal Skull Development Using Computed Tomography Images.", Innovation and Research in BioMedical engineering (IRBM), 42(1):19-27 (2021)
3. S. Mazdeyasna, C. Huang, A. Bonaroti, **M. Mohtasebi**, Q. Cheng, L. Wong, G. Yu, "Intraoperative Optical and Fluorescence Imaging of Blood Flow Distributions in Mastectomy Skin Flaps for Identifying Ischemic Tissues", Plastic and Reconstructive Surgery 150, no. 2: 282-287 (2022).
4. **M. Mohtasebi**, C. Huang, S. Mazdeyasna, B. Green, K. Saatman, Q. Cheng, L. Chen, G. Yu. "Noncontact Optical Assessment of Spontaneous Low-Frequency Fluctuations of Cerebral Blood Flow in Neonatal Intraventricular Hemorrhage." Optical Techniques in Neurosurgery, Neurophotonics, and Optogenetics. Vol. 11629. International Society for Optics and Photonics, (2021).
5. C. Huang, S. Mazdeyasna, **M. Mohtasebi**, K. Saatman, Q. Cheng, G. Yu, L. Chen, "Noncontact Speckle Contrast Diffuse Correlation Tomography of Cerebral Blood Flow in Neonatal Piglets with Perinatal Diseases", Journal of Biophotonics, JBIO2662. DOI: 10.1002/jbio.202000366 (2020)
6. S. Ghadimi, **M. Mohtasebi**, H. Abrishami Moghaddam, R. Grebe, M. Giti, and F. Wallois. "A Neonatal Bimodal MR-CT Head Template.", PloS one 12, no. 1 (2017).

Book:

1. D. Irwin, S. Mazdeyasna, C. Huang, M. Mohtasebi, **X. Liu**, L. Chen & G. Yu, Near-infrared Speckle Contrast Diffuse Correlation Tomography for Noncontact Imaging of Tissue Blood Flow Distribution. CRC Press (2022)

Conference Abstracts

1. **M. Mohtasebi**, L. Chen, S. Mazdeyasna, D. Singh, X. Liu, C. Huang, S. Rabienea Haratbar, F. Fathi, D. Powell, K. Saatman, Q. Cheng, G. Yu, “Noncontact Optical Assessment of Disrupted Cerebral Functional Connectivity in a Piglet Model of Transient Ischemic Stroke”, SPIE Photonics West Conference, San Francisco, CA, USA (2022) (Oral Presentation)
2. F. Fathi, S. Mazdeyasna, **M. Mohtasebi**, D. Singh, X. Liu, C. Huang, S. Rabienea Haratbar, L. Chen, G. Yu, “Laser Speckle Contrast Imaging of Cerebral Blood Flow Using Picosecond Pulsed Laser Illumination”, SPIE Photonics West Conference, San Francisco, CA, USA (2022) (Oral Presentation)
3. X. Liu, L. Chen, C. Huang, **M. Mohtasebi**, S. Mazdeyasna, Y. Gu, G. Yu, “A Wearable Optical Sensor for Continuous Monitoring of Cerebral Ischemia in Rodents and Piglets”, SPIE Photonics West Conference, San Francisco, CA, USA (2022) (Oral Presentation)
4. D. Singh, L. Chen, C. Huang, S. Mazdeyasna, F. Fathi, **M. Mohtasebi**, G. Yu, “A Fast Algorithm Towards Real-Time Laser Speckle Contrast Imaging”, SPIE Photonics West Conference, San Francisco, CA, USA (2022) (Poster Presentation)

Professional Service and Leadership

- President of the Biomedical Engineering Society (BMES) Student Chapter at University of Kentucky (2020-2021)
- Representative of Department of Biomedical Engineering at Graduate Student Congress, University of Kentucky (2020-2021)
- Member of Graduate Student Congress Professional Development & Networking Committee (2020-2021)
- Participate in UK College of Engineering E-Day to represent the Biomedical Optics Lab and BMES (2019-2021)
- Present UK Department of Biomedical Engineering at the District Science Fair, Lexington, KY (2019)
- Prepare and present UK BME at meet the BME professors, Lexington, KY (2019)